



# Università degli Studi di Ferrara

DOTTORATO DI RICERCA IN  
FISICA

CICLO XXII

COORDINATORE Prof. Frontera Filippo

CONVECTION DURING THE AFRICAN MONSOON:  
OBSERVATIONS AND MODELLING OF PRECIPITATION  
AND THE ROLE OF REGIONAL CIRCULATION  
ON ATMOSPHERIC COMPOSITION

Settore Scientifico Disciplinare FIS/06

**Dottorando**

Dott. Orlandi Emiliano

**Tutore interno**

Prof. Prodi Franco

**Tutore esterno**

Dr. Fierli Federico

Anni 2007/2009

# Contents

<b>1</b>	<b>Introduction</b>	<b>3</b>
1.1	General review and scientific issues . . . . .	3
1.2	Thesis structure . . . . .	17
<b>2</b>	<b>Mesoscale modelling of convection and Monsoon dynamics</b>	<b>21</b>
2.1	State of the art of regional modelling in West Africa . . . . .	21
2.2	Model intercomparison in the frame of AMMA . . . . .	25
<b>3</b>	<b>How to improve the model scores? A simple data assimilation approach</b>	<b>31</b>
3.1	Observations used . . . . .	32
3.2	The BOLAM model . . . . .	35
3.3	Description of the MCS event . . . . .	35
3.4	Nudging procedure and simulation set-up . . . . .	38
3.4.1	Sensitivity tests . . . . .	41
3.5	Comparison of simulated MCS lifecycle with observations . . . . .	43
3.5.1	Cloud top brightness temperature . . . . .	43
3.5.2	Rainfall . . . . .	50
3.6	Nudging impact on model dynamics . . . . .	55
<b>4</b>	<b>The AMMA field campaign</b>	<b>61</b>
4.1	Description of the AMMA field campaign . . . . .	61

---

4.2	Aircraft campaign background . . . . .	67
4.3	Convective outflow measurements . . . . .	78
4.3.1	Satellite observations . . . . .	78
4.3.2	M55 observations . . . . .	79
<b>5</b>	<b>Impact of deep convection in the tropical tropopause layer in West Africa</b>	<b>87</b>
5.1	Mesoscale simulation . . . . .	88
5.1.1	Validation . . . . .	88
5.1.2	Trajectories . . . . .	89
5.2	Convective outflow from BOLAM trajectories . . . . .	93
5.3	Comparison with observations . . . . .	99
<b>6</b>	<b>Transport of biomass burning emissions</b>	<b>105</b>
6.1	Observational evidence . . . . .	106
6.2	Model description and simulation set up. . . . .	110
6.3	Biomass burning transport . . . . .	113
<b>7</b>	<b>Seasonal scale re-analysis</b>	<b>121</b>
	<b>Conclusions</b>	<b>134</b>
<b>A</b>	<b>List of acronyms</b>	<b>141</b>
<b>B</b>	<b>List of simulations</b>	<b>143</b>



# Chapter 1

## Introduction

### 1.1 General review and scientific issues

To give an idea on what a tropical monsoon system is we cite from Holton (2004): “The term monsoon is commonly used in a rather general sense to designate any seasonally reversing circulation system. The basic drive for a monsoon circulation is provided by the contrast in the thermal properties of the land and sea surfaces.” The absorption of the solar radiation raises the surface temperature over land much more rapidly than over the ocean. Because of their different heat capacity, thin layer of the soil responds to the seasonal change in surface temperature more rapidly than the upper layer of the ocean that responds on a longer (seasonal) timescale. The warming of the land relative to the ocean leads to enhanced cumulus convection, and hence to latent heat release, which produces warm temperature throughout the troposphere.

Beyond the general features shared by all tropical monsoons, West African monsoon (WAM) has its own structure and variability. Monsoon dynamic involves a wide range of space (synoptic, regional and local) and time (decadal, interannual, seasonal and intra-seasonal) scales. Figure 1.1 shows streamlines from mean ECMWF (European Centre for Medium-Range Weather Forecast) wind fields in

July 2002, to sketch the main dynamical features, at 850 hPa, 650 hPa and 250hPa. Usually in July the WAM is in its mature stage and the atmospheric circulation related with the monsoon is well developed. Low level winds are shown in top left panel: the Harmattan, driven by the Saharan anticyclone (top right panel), the south-easterly trade winds and the monsoon flow, driven by the temperature gradient between the warm Guinean coast and the cold eastern equatorial Atlantic (Gu and Adler, 2004). Red line in the same panel represents the inter-tropical front ITF, where moist southwesterly monsoon winds and dry northeasterly Harmattan converge.

Upper right panel of figure 1.1 shows the atmospheric circulation at 650 hPa: the Saharan anticyclone, due to the descendent branch of the Hadley cell, and the African Easterly Jet (AEJ), are highlighted by the shaded area. AEJ is essentially geostrophic and owes its existence to the presence a strong surface wetness contrasts between the Sahara and equatorial Africa that leads to a positive surface temperature gradient , which, according to the thermal wind relation, induces easterly shear over the surface monsoon westerlies (Cook, 1999). Upper tropospheric dynamics (250 hPa) is shown in bottom panel of figure 1.1. The easterly wind blowing, around 10N and during the boreal summer, over Africa and the Atlantic ocean is the Tropical Easterly Jet (TEJ).

The inter-decadal and inter-annual variability of rainfall in the Sahelian region is shown by the Sahelian standardized rainfall index presented in figure 1.2. The rainfall index is evaluated as the difference, between the Sahelian (where sahel is identified by the lon-lat box: 10N-17.5N 22.5W-17.5E) rainfall for a given year and the mean over the reference period, divided by the standard deviation of the rainfall time series. Even if this index hides the spatial differences of precipitation trends in Sahel (Ali and Lebel, 2009; Lebel and Ali, 2009), it is used to understand the strong interdecadal variability of rainfall over the Sahelian region as a whole.

Figure 1.2 clearly shows a severe drought period between 1968 and today that

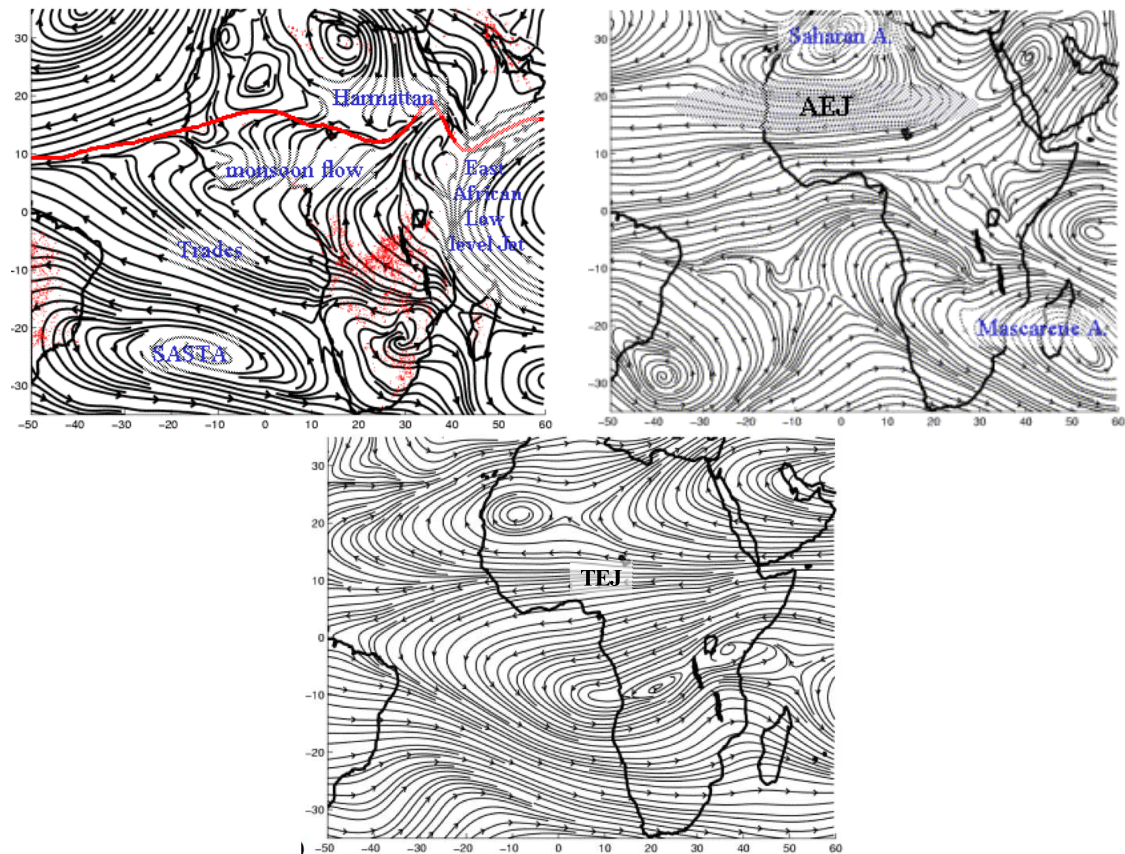


Figure 1.1: Monthly mean streamlines from July 2002 ECMWF analyses. 850 hPa [upper left]; 650 hPa [upper right] and 250 hPa. Main dynamical features are written in blue. Inter-tropical front is represented by a red dotted line. Red points symbolize the position of the fires in July. Shaded areas symbolize the AEJ location. (Adapted from Sauvage et al. (2005))

represent one of the strongest interdecadal signals on the planet in the 20<sup>th</sup> century. As reported by Giannini et al. (2003) Sahel is highly sensitive to sea surface temperature (SST) variability in all tropical basins, remote (Pacific) and local (Atlantic and Indian). A positive trend in equatorial Indian Ocean SSTs, between East Africa and Indonesia, is identified as the proximate cause for the negative rainfall trend observed in the Sahel from the late 1960s.

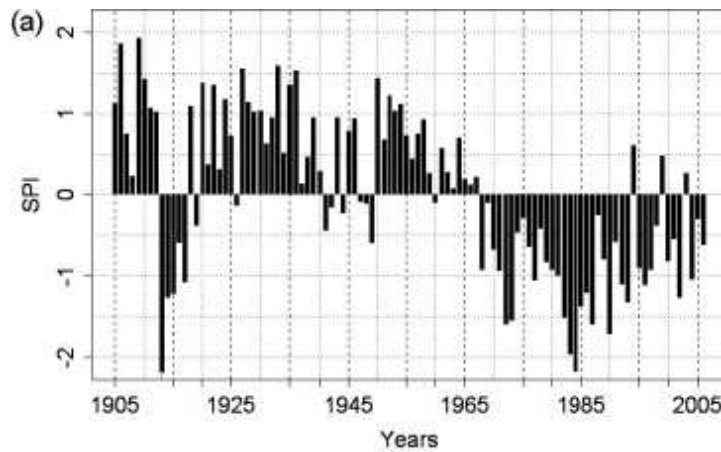


Figure 1.2: Sahelian precipitation index computed for period 1905-2006. (From Ali and Lebel (2009))

On a shorter time scale the seasonal cycle of the WAM is shown in figure 1.3. It represents mean precipitation between 10E and 10W over the 1998-2003 period. Major intense rainfall events appear near the Gulf of Guinea (5N) starting in April (day 90), move to northward latitudes around 10N during the July mid-September period and then retreat back to the south after mid-September October, corresponding to the seasonal migration of the inter tropical convergence zone (ITCZ) over the Sahelian region.



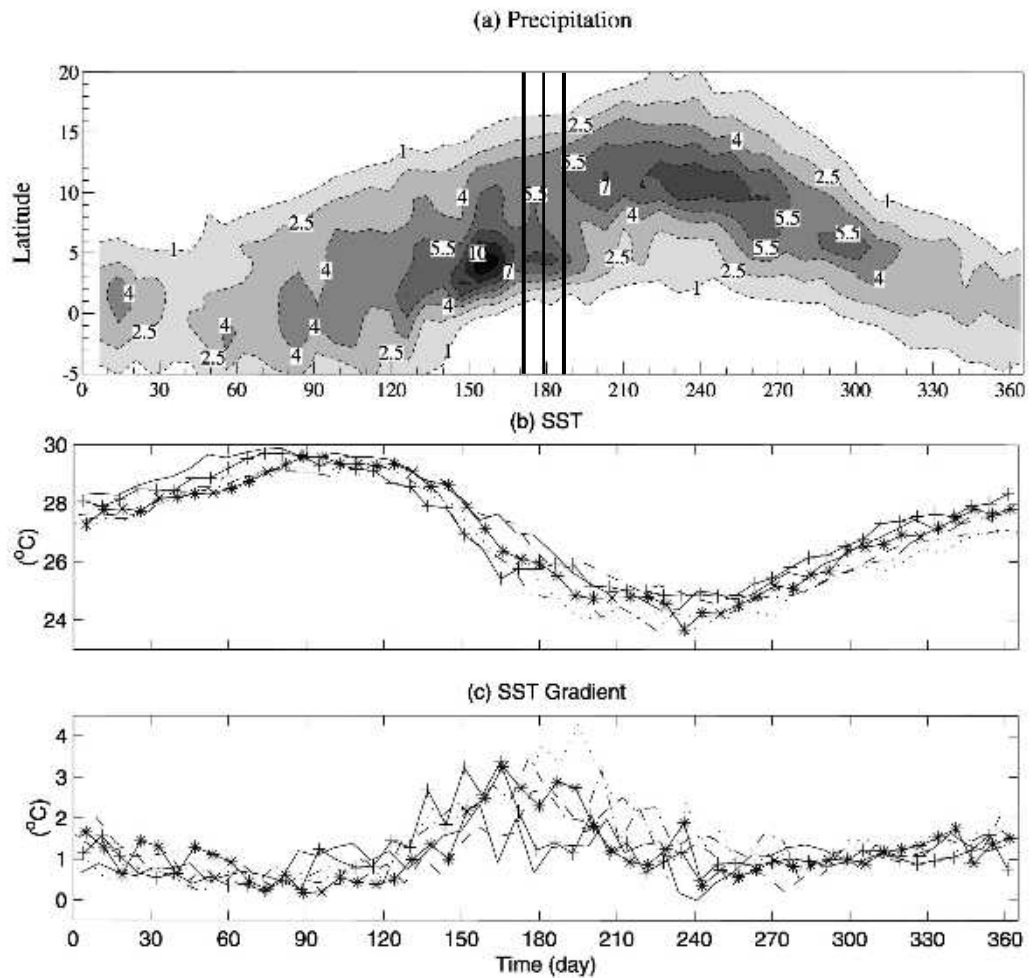


Figure 1.3: Seasonal cycles in (a) weekly rainfall ( $\text{mm day}^{-1}$ ) between 9.5W and 9.5E, (b) weekly SST ( $^{\circ}\text{C}$ ; 4S-4N, 10W-5E), and (c) weekly SST differences between 2N and 0, averaged along 10W-5E. In (b) and (c), solid lines are used for 1998, dashed lines for 1999, dashed-dotted lines for 2000, dotted lines for 2001, lines with asterisks (\*) for 2002, and lines with crosses (1) for 2003. (Adapted from Gu and Adler (2004)). Vertical lines in (a) indicates the mean monsoon on-set date with its standard deviation (Sultan and Janicot, 2003).

The monsoon onset is the seasonal migration of rain band between June and July, it is defined as the abrupt latitudinal shift of the ITCZ from a quasi-stationary location at 5N in May-June to a second quasi-stationary location at 10N in July-August. Sultan and Janicot (2003) found that the transition phase between the two stationary positions of the ITCZ is accompanied by low convective activity over West Africa and they indicated that the mean date for the WAM onset is 24 June with a standard deviation of 8 days.

As reported by Gu and Adler (2004) intense rainfall in the Gulf of Guinea begins in April (day 90 in figure 1.3) following the occurrence of warm sea surface temperature (SST) in the tropical eastern Atlantic. Low-level southerly wind accelerates and enhances upwelling of the eastern Atlantic ocean resulting in a decreased SST around the equator. This increases the SST gradient between the equator and 2N (fig. 1.3c) enhances southerly winds and produces favourable conditions for convection and rainfall around 5N during days 120-190. The cold SST zone begins to suppress the convection and rainfall when the mean SST is less than about 27°C (around day 180). Then the surface rainfall events near the Gulf of Guinea disappear and a second rain belt begins to develop around 10N in July and remains there during the later summer season.

Looking at smaller time-scale and focusing on the Sahelian region, we observe that there are few intense and short precipitation events that carry the whole rainfall over the region, as shown by figure 1.4, where drastic increase in time of precipitation are due to intense events related with mesoscale convective systems (MCS) in the Sahelian region.

MCS definition includes fast moving squall lines (10 to 15 m/s) that can be large systems up to 1000 km large, according to Redelsperger et al. (2002), and responsible for 80% of the annual rainfall in the sub-Saharan region (Mohr et al., 1999). The annual variability of MCSs in West Africa (WA) is driven by monsoon circulation, which provides favourable conditions for convection formation in the

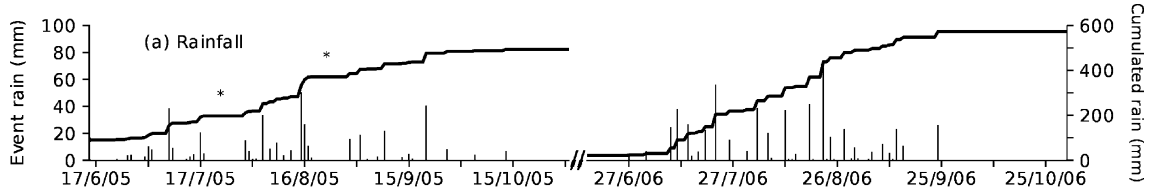


Figure 1.4: Daily (bars) and cumulated (line) rainfall for 2005 [left] and 2006 [right] at the Wankama catchment site, 13.65N 2.63E. (From Boulain et al. (2009))

Sahelian area.

The regional-scale environment of MCS development in WA has similar characteristics, which are common to organized convection (Laing and Fritsch, 2000), i.e. baroclinic zones characterized by large vertical wind shear in the lower troposphere and high Convective Available Potential Energy (CAPE). At a larger scale the low level AEJ constitutes the source of the African easterly waves (AEW), which are well recognised in playing an important role in the organization and modulation of convection (Mekonnen et al., 2006).

Concerning MCS internal dynamics, a conceptual model of a two-dimensional steady state squall line was proposed by Rotunno et al. (1988), which stresses the importance of a strong downwelling density current, a low-level wind shear and high CAPE value in maintaining a long-lived squall line. Such factors promote deep lifting at the leading edge of the system and enable it to maintain themselves and to propagate by mean of the continuous triggering of new convective cells. Mid-level dry air is important in promoting evaporation, allowing the formation of the density current. Figure 1.5 shows the sketch of the dynamic of a simplified 2 dimensional MCS. The thick black arrow indicates the density current allowing the formation of new convective cells, thick white arrow depicts the transport of boundary layer air up to the level of main convective outflow and thin arrows on the right shows the vertical wind shear. That picture must be taken just as an example used to show the main characteristics of a MCS, the real dynamic is more complicated and fully 3 dimensional.

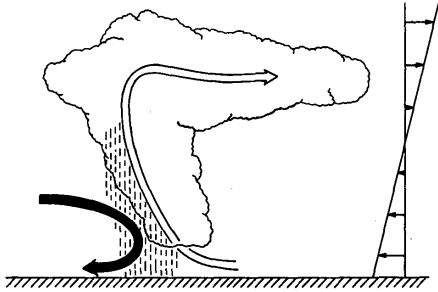


Figure 1.5: Schematic sketch of a 2 dimensional squall line. Black arrow indicates the density current, white arrow depicts the transport of boundary layer air up to the level of main convective outflow and thin arrows on the right shows the vertical wind shear. (From Rotunno et al. (1988))

This simplified 2D scheme can be roughly applied to characterise MCSs in west Africa. Middle level dry air can be also supplied by dry intrusion arriving from the Saharan area (Roca et al., 2005), while the vertical shear is due to the transition between the monsoon flow coming from the south-west in the low-level, and the AEJ in the middle-level (Sultan and Janicot, 2003). Large CAPE values are jointly provided by the strong heating of the surface and the wet air masses transported by the monsoon flow.

Concerning MCS lifetime, Laing et al. (2008) studied the propagation and diurnal cycle of organized convection in the period from May to August and in northern tropical Africa using five years (1999-2003) of infrared images in the  $10.5 \mu\text{m}$  channel of the Meteosat7 satellite. They reported that convective episodes tend to initiate in the lee of high terrain, consistent with thermal forcing from elevated heat sources. Single MCS spans an average distance of about 1000 km and last about 25 h with a phase speed between 10 and  $20 \text{ ms}^{-1}$ , but a substantial fraction of events exhibits systematic propagation over grater space scales (regional to continental) while undergoing decay and regeneration. An example of an MCS developing and propagating between 18 and 19 August 2006 in west Africa is given

in figure 1.6.

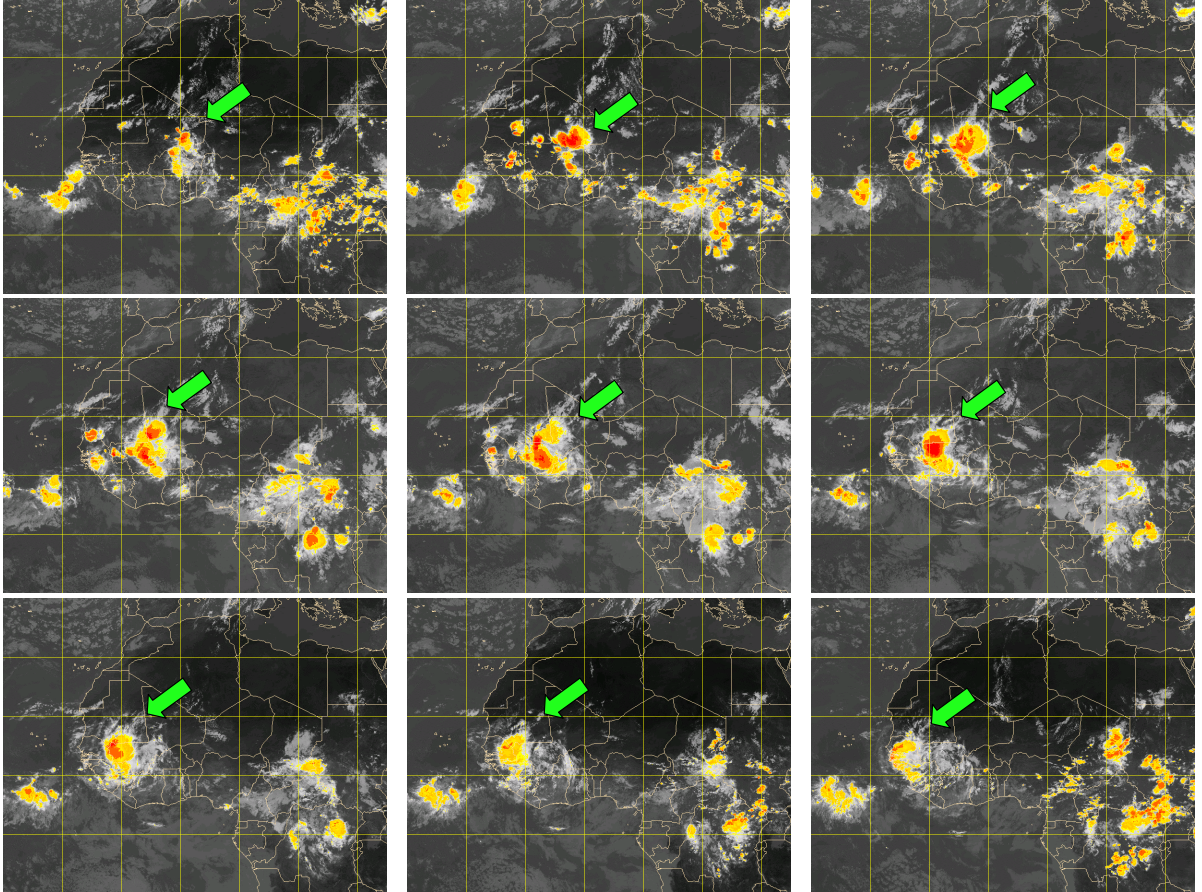


Figure 1.6: MSG cloud top brightness temperature from 15UTC of 18/08/2006 to 15UTC 19/08/2006 at 3 hours intervals. Yellow, orange and red colours correspond to cloud colder than 230K, 215K and 200K respectively.

Regarding the interaction between organised convection and AEW Laing et al. (2008) showed that organized mesoscale systems moved faster than the waves with an average phase speed of 12 and  $7.7 \text{ ms}^{-1}$ , respectively. Furthermore they found that during the peak monsoon period and in the zone between 10 E and 10 W, more than one third of cold cloud episodes occurred behind the trough of easterly waves, nearly one-quarter of cloud episodes occurred ahead of the trough and one-

tenth occurred within the wave trough. Regarding the diurnal cycle Laing et al. (2008) report that organised convection most probably occurs between 18 and 2 local time and west of 20 E.

So WAM dynamics is determined by the interaction of atmospheric features that have different spatial and temporal scale. Furthermore, the two-way interaction between atmosphere and ocean, soil and vegetation, contributes to increase the complexity of the picture. For those reasons meteorological and climatic models, both at global and regional scales, still shows important weaknesses when simulate rainfall. The other reason that makes modelling of west African monsoon a difficult task is the scarcity of measurements (Agusti-Panareda et al., 2009).

Numerical weather prediction precipitation forecast is generally poor during the wet West African monsoon season from June to September, because of the lack of data available. Particularly lacking are radiosondes data, which are the only observing system that provide a comprehensive 3-D thermodynamic and dynamic information of the atmosphere in the lower and mid-troposphere. Radiosonde observations are particularly important for the Sahel region located between 12N and 20N which is characterized by large gradients in temperature and moisture in the lower troposphere.

To overcome those difficulties, huge effort have been done to improve seasonal forecast of WAM. A correct prediction of the WAM onset is of great help for agriculture management in West Africa, where marked interannual variations in recent decades have resulted in extremely dry years with devastating environmental and socio-economic impacts. In a region where agriculture is mainly rain fed, drought years represent a serious danger for food and water security for West African societies.

Together with droughts another hazard for West African region is represented by floods as reported by United Nation-International Strategy for Disaster Reduction ([www.unisdr.org](http://www.unisdr.org)) 70% of natural disasters in West Africa between 1991 and 2005

are due to flooding. Thus short-range (0.5-2 days) forecasts of intense precipitation events are useful for early warning alert service in West Africa.

In west Africa lower tropospheric monsoon circulation, inter-hemispheric transport from central Africa driven by upper and middle tropospheric jet, long range transport from Asian monsoon region, deep convection, in-mixing across sub-tropical jet (STJ) from midlatitudes, export downwind and transport into the lower stratosphere (LS) superimpose their effect, leading to a complex atmospheric transport pattern (see the sketch in figure 1.7). Since west Africa is an important source for both biogenic and anthropogenic trace gases that controls the ozone concentration of the troposphere (e.g. Crutzen and Andreae (1990), Williams et al. (2009)), the distribution of chemicals and aerosols at local, regional and global scale is a key issue for atmospheric composition and global radiative budget.

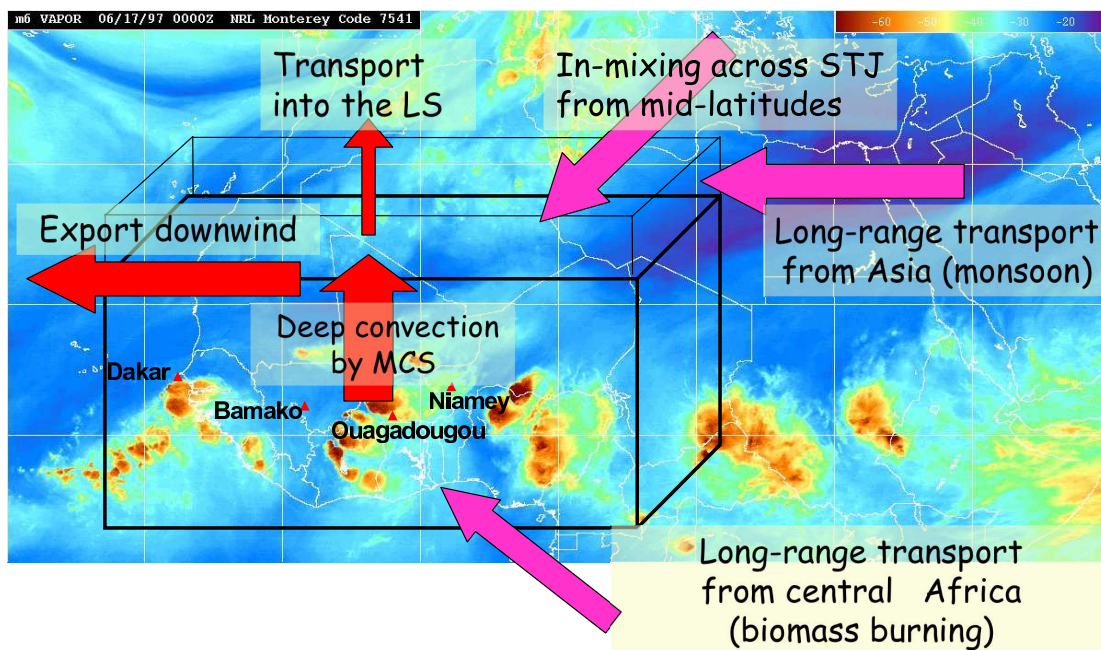


Figure 1.7: Main transport mechanisms influencing atmospheric composition over west Africa.

The tropospheric concentration of  $O_3$  and its precursors ( $CO$ ,  $NO$ ,  $NO_2$  and

volatile organic compound) plays a fundamental role in determining the oxidising capacity of the troposphere through the formation of the OH radical. Furthermore oxidised organic compound can lead to the formation of secondary aerosols which affect cloud formation processes and the radiative budget.

Tropical and deciduous forest in west Africa emits large amount of volatile organic compounds, which are rapidly oxidised and form secondary organic aerosols (Capes et al., 2009). Soil emissions of nitrous oxide, due to microbial processes, are quickly oxidised to  $\text{NO}_2$ , changing the rate of ozone production (Delon et al., 2008). Quickly growing African cities and megacities as Lagos, emit large amount of pollutants. Volatile organic compound, CO and  $\text{NO}_x$  emitted by vehicle combustion, power generation and petrochemical activity put Lagos amongst the cities with highest emission of the world (Hopkins et al., 2009).

Chemicals and aerosols sources in west Africa are still poorly known because of lack of direct measurements. Recently a large field campaign in the framework of AMMA (African Monsoon Multidisciplinary Analysis, Redelsperger et al. (2006)), devoted to the study of the dynamics and chemical composition of atmosphere in West Africa, gave some insight into emission processes over west Africa.

Together with local emissions also long range transport of biomass burning (BB) plumes influences the composition of troposphere and lower stratosphere in the region. Africa is the continent emitting the largest quantity of BB emissions with a strong inter-hemispheric transition between West Africa in boreal winter to central and southern Africa (figure 1.8) in boreal summer (Crutzen and Andreae, 1990) following the location of the dry season in each hemisphere. Production of O<sub>3</sub> downwind from wild fires influences the global oxidizing capacity and thus the lifetime of greenhouse gases such as CH<sub>4</sub>.

Layers influenced by BB plumes have been observed in the mid and upper troposphere over the Atlantic Ocean (Thompson et al., 1996; Jenkins et al., 2008) and over West Africa (Thouret et al., 2009) during the summer monsoon period.



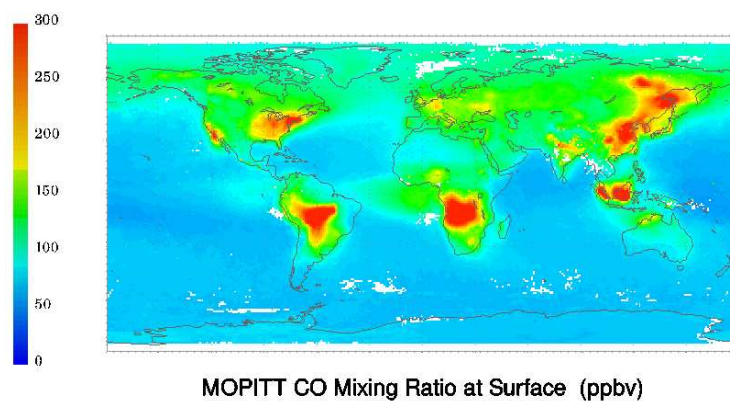


Figure 1.8: Surface mean CO concentration for August 2006 measured by MOPITT.

Mari et al. (2008) investigated the variability in the transport of BB emissions from central Africa to the gulf of Guinea (West Africa) and the Atlantic Ocean in the mid-troposphere during July and August 2006 and suggested that it is driven by variations in the southern branch of the African easterly jet. During periods when this jet is less active, BB emissions can be trapped over the continent and injected into the upper troposphere by deep convection, influencing the ozone concentration in the upper troposphere.

Vertical transport within the troposphere of chemicals and aerosols over tropical Africa is mainly due to convection. Other mechanism that are effective in middle latitude, like frontal uplift or slow isentropic transport, are less relevant with respect to convective uplift in northern tropical Africa during boreal summer. The transport within deep convective cloud also determine the exchange between troposphere and stratosphere. Air masses are transported by deep convection up to the level of neutral buoyancy, laying within the tropical tropopause layer (TTL), the interface layer between troposphere and stratosphere. Afterward TTL air masses

are slowly uplifted into the stratosphere due to dynamical forcing and radiative heating (Fueglistaler et al., 2005).

The determination of the height of convective clouds and their subsequent impact on TTL composition is important to estimate but it is difficult to achieve from satellite measurements due to the limited vertical resolution of satellite-borne profilers, on-board of METEOSAT for example, at the tropical tropopause. The information on the height where deep convection outflow occurs and modifies the water vapour and trace gas distributions can be derived from in-situ observations that offer an adequate vertical resolution. Several observational analyses based on in-situ aircraft data show that deep convection can impact up to the tropical tropopause (see for example Corti et al. (2008) and Khaykin et al. (2009)).

High vertical resolution observations of chemicals in the UTLS (Upper troposphere Lower Stratosphere) have been used to assess the role of convection in determining the atmospheric composition. Trace gases mixing ratios within recently uplifted air masses have been used to calculate the rate at which UTLS air is substituted by lower tropospheric air (Bertram et al., 2007), the fraction of boundary layer air present in the convective outflow (Bertram et al., 2007; Bechara et al., 2009), the vertical transport timescale within MCS (Bechara et al., 2009) and the photochemical activity of MCS' outflow.

It is difficult to distinguish between recent convective outflow and air masses transported from far away that underwent to chemical and photochemical processing. In west African atmosphere local convection superimposes its signature on other transport processes that take place in the troposphere and lower stratosphere: (1) the tropical easterly jet transport air masses uplifted by deep convection in the Asian monsoon area (Barret et al., 2008) (2) transport of extra tropical low stratospheric air masses within the tropical tropopause layer (3) transport of biomass burning plumes coming from south hemispheric wild fires and uplifted by deep convection in central Africa (Real et al., 2009).

For this, the use of trajectory simulations, passive tracer transport and chemistry-transport model simulations can be used to determine the area of provenience and distinguish between fresh convective outflow and aged air masses.

## 1.2 Thesis structure

The research presented here addresses a twofold issue: (1) analyse the dynamic of MCS, their role in precipitation and their predictability; (2) study how convection during the west African summer monsoon impacts on atmospheric composition. The approach chosen is based on a synergy between state of the art atmospheric mesoscale modelling and the analysis of a wide range and typology of observations. Availability of observations is a key problem for west Africa and the large international initiative AMMA (African Monsoon Multidisciplinary Analysis), in the frame of which the present study was conducted, aimed at improving our knowledge and understanding of chemical and physical processes within the WAM through balloon, aircraft, satellite, ground and sea based measurements.

One of the final objectives of AMMA is to improve the forecast the WAM on various time and spatial scales and assess its impact on climate. In this frame, the synergy between observations and modelling is a of fundamental importance since models are needed to interpret and homogenise measurements and, on the other hand, observations are needed to improve and validate models.

The scientific issues presented in the previous section are addresses in the present work with the aid of the mesoscale model BOLAM (BOlogna Limited Area Model) and measurements coming from satellite, ground based and aircraft measurements. Thus the first part of the thesis is devoted to test and improve BOLAM model while in the second part we use the BOLAM model to analyse measurements mainly collected in the frame of the AMMA field campaign during August 2006.

In chapter 2 we give a review of the problems that mesoscale models show when used in west Africa: low reliability of meteorological fields used to initialise regional models, the difficulty in reproduce the initiation and propagation of organised convective systems and the incorrect prediction of rainfall amount. Then we show a case study of intense precipitation due to an organised convective system and we evaluate the performances of numerous mesoscale models in reproducing precipitation rain rate and the propagation of the system. Precipitation generated by mesoscale models is compared with satellite precipitation estimates.

Precipitation related with deep convective events appear to be poorly forecasted by mesoscale model and often weakly correlates with rainfall measurements. So in chapter 3 we describe an approach to improve mesoscale model performances in reproducing the formation and propagation of organised convection and related precipitation. We present the implementation of a nudging procedure in the BOLAM model and we evaluate it using cloud top brightness temperature (CTBT) measured by Meteosat satellite together with precipitation estimates. The assimilation approach is based on the continuous assimilation of Meteosat infrared brightness temperatures within the model.

Chapter 4 is dedicated to the description of the field campaign that took place in west Africa in the frame of the AMMA project. During the campaign ground-based, ship, balloon, aircraft and satellite measurements were performed to sample the atmosphere, the ocean, the soil and the vegetation in west Africa. We particularly focus on atmospheric measurements taken during 2006 wet season. The measurement strategy is described and a review of the current literature based on aircraft and balloon measurements is presented together with the analyses of the average profiles of chemicals and aerosol in WA from aircraft observations. Moreover the observed role of convection on in situ observations from the M55 research aircraft is analysed.

The improvements achieved with the nudging scheme described in chapter 3

allowed to better simulate tracer transport in chapter 5. Beside the amelioration of precipitation, the improvement of organised convection position and evolution as well as the coherent modification of the divergent wind at convection outflow level, is exploited to evaluate the effect of deep convection over trace gases transport.

In chapter 5 we utilise the BOLAM model, together with the assimilation scheme, to analyse the impact of convection on the composition of the tropical tropopause layer in West-Africa. More specifically the model is validated against observations from M55 aircraft in convectively perturbed conditions and is then used to quantitatively estimate the impact of deep convection in west African upper troposphere.

Together with deep convective impact on the upper tropospheric composition, we also studied the influence of inter-hemispheric transport of biomass burning emissions from southern hemispheric wild fires. In chapter 6 we used BOLAM mesoscale model simulation to investigate whether the measurements collected during the AMMA field campaign were influenced or not by biomass burning emissions.

Pollutant plumes with enhanced concentrations of trace gases and aerosols were measured by research aircraft over the southern coast of West Africa during August 2006. We ran the BOLAM mesoscale model including a biomass burning tracer to confirm that the origin of the plumes are wild fires located in the southern hemisphere. Furthermore the injection of a tracer per day allowed to evaluate the time needed by air masses to travel between emission region and west Africa at different altitudes.

In the chapter 7 a follow-up of the work presented in the thesis is given. A seasonal mesoscale simulation covering the whole West African area is presented showing the impact of the nudging scheme on longer time-scales.

In the last section we delineate the general conclusions of this thesis giving an outline of future developments made possible by the finding of this study.



## Chapter 2

# Mesoscale modelling of convection and Monsoon dynamics

### 2.1 State of the art of regional modelling in West Africa

The complex coupling between different spatial and temporal scales involved in west African atmosphere dynamics, makes precipitation forecast on time scale ranging from inter-decadal to the single convective event a difficult task to be addressed. Synoptic atmospheric features like the low tropospheric African easterly jet (AEJ), the perturbations of this jet (African easterly wave AEW) and the tropical easterly jet promote and organise deep convection (Mekonnen et al., 2006). On the other hand, diabatically generated potential vorticity anomalies has a role in sustaining AEW (Berry and Thorncroft, 2005), soil moisture gradient, also due to MCS precipitation, determines the formation of the AEJ (Cook, 1999) and convection contributes to reinforce the monsoon flow at low levels (Diongue et al., 2002).

Another example of scale interaction is reported by Giannini et al. (2003) and regards the driving of two distinct pattern of rainfall variability by oceanic sea

surface temperature (SST) anomalies: on an inter-decadal time scale, Sahel is highly sensitive to SST variability in all tropical basins, remote (Pacific) and local (Atlantic and Indian). A positive trend in equatorial Indian Ocean SSTs, between East Africa and Indonesia, is identified as the proximate cause for the negative rainfall trend observed in the Sahel from the late 1960s. On a seasonal time scale anomalies in the equatorial Atlantic ocean drives precipitation anomalies of opposite sign in coastal west Africa and in the Sahelian region.

Modelling of west African monsoon is a difficult task also because of the lack of measurements (Agusti-Panareda et al., 2009) in fact numerical weather prediction of precipitation forecast is often low reliable during the wet west African monsoon season. Radiosonde data are particularly necessary because provide thermodynamic and dynamic profiles of both troposphere and stratosphere. Radiosonde observation are necessary in particular in the Sahelian region (12N-20N), that is characterised by strong latitudinal temperature and moisture gradients in the lower troposphere.

Before the African Monsoon Multidisciplinary Analysis (AMMA) field experiment in 2006, the radiosonde network was quite sparse and only few data were received via the Global Telecommunication System. Therefore, few radiosonde observations were assimilated in numerical weather prediction models' analyses. The AMMA project put a large effort on restoring and enhancing the radiosonde network (Parker et al., 2008). The AMMA radiosonde observations had a significant impact on the ECMWF analysis. ECMWF re-analyses show an overall improvement due to the assimilation of AMMA data, with an increase of deep cloud in the analysis and a precipitation increase in the 1-day forecast between 10W and 10E. On the other hand, the influence on the forecast is very short-lived due to large model biases. The soundings reveal large model biases in boundary layer temperature, which are too low, over northern and eastern Sahel. Assimilation of soundings east of 15E results in large temperature increments that



caused unrealistic increments of winds. Thus, although the mean analysis/forecast is improved over central Sahel, it is actually degraded over eastern Sahel.

The lack of measurements in the region lead to uncorrected or biased global meteorological models' analysis used to initialise regional models. Unrealistic initial and boundary conditions drive mesoscale models to incorrect representation of convection. Particularly important is the correct initialisation of humidity fields, and this initial-value problem is increased for the tropics and convective flows as large-scale forcings are weaker than for midlatitudes and condensation is an all-or-nothing process.

Diongue et al. (2002) studied the evolution of a squall line over Sahel in August 1992. They report moist bias in the ECMWF ERA-15 (ECMWF Re-Analyses from December 1978 to February 1994) reanalyses. The moist bias led to absolute instability and moist layers mainly in the deep Saharian boundary layer and at mid-level over Mali and Nigeria, respectively. Such features appeared to be responsible for the triggering of convective systems in the simulation at incorrect locations as compared with Meteosat images. They analysed the initial fields to find region of spurious instability by mean of the Brunt-Vaisala frequency. They modified the water vapour profile in order to suppress unrealistic instabilities. The corrections lead to a successful simulation of formation and propagation of the studied squall line.

Druyan et al. (2001) used regional model to simulate the Synoptic weather features over West Africa in the period 8-22 August 1988. They also needed to develop a methodology to improve ECMWF analyses, in particular moisture fields, used as initial and boundary conditions for the regional model. They found that more realistic time-space distribution of precipitation, when compared with rain gauge observations, were obtained by modifying the initial moisture and circulation fields to improve their compatibility with the regional model. Thus, a 24 hours simulation was ran prior then the initial date of the simulation (7 August), the

humidity fields produced by the regional model were used together with ECMWF temperatures to evaluate specific humidity profiles, that was then used instead of the ECMWF ones, to initialise the regional model.

Another way to improve the initial field used to initialise a limited area model in the tropics have been developed by Ma et al. (2007). They created a technique to improve initialization of a tropical cyclone prediction model using diabatic heating profiles estimated from a combination of both infrared satellite cloud imagery and satellite-derived rainfall. They created reference diabatic heating profiles, classifying them into three kinds: convective, stratiform or composite types. Then, during a 24h period prior to the start of the simulation, they used a nudging scheme to replace model-generated heating profiles by the reference heating profiles on the basis of the satellite-observed cloud top temperature and rainfall type.

Orlandi et al. (2010) used a similar approach to improve the representation of mesoscale convective systems in the region of West Africa. They developed and implemented a nudging procedure in the mesoscale meteorological model BOLAM (Malguzzi et al., 2006) to assimilate the METEOSAT infrared brightness temperatures within the model in order to trigger convection, where observations show the presence of large convective systems and to inhibits convection, when the model reproduces unrealistic convective precipitation. They showed that the nudging improves the geographical distribution and time evolution of mesoscale convective systems reproduced by the model and that the impact of assimilation is positive up to 13 hours after the end of the nudging period. They also showed that the nudging improves the simulated amount and spatial distribution of precipitation and coherently modifies the dynamical fields.

## 2.2 Model intercomparison in the frame of AMMA

In the present section we give an example of precipitation forecasts in the Sahelian region performed by mesoscale and global models. We participated to a model inter-comparison conducted in the framework of AMMA project aimed to assess the capability of meteorological models in reproducing a case of intense precipitation occurred in Sahel between 28 and 30 August 2005.

Figure 2.1 shows the Hovmoller (longitude versus time) plot of precipitation and the meridional component of the wind at 700 hPa averaged between 7N and 16N for the period 25-31 August 2005. 700 hPa is the altitude at which African easterly wave (AEW) forms as instability of the African easterly jet on its southern and northern side (Berry and Thorncroft, 2005). Interaction between MCS and AEW has been reported by many authors (e.g. Berry and Thorncroft (2005) and Mekonnen et al. (2006)), deep convective organisation seems to be favoured by the presence of AEW and diabatically generated potential vorticity anomalies has a role in sustaining AEW activity. As captured by time longitude diagrams of meridional wind at 700 hPa (figure 2.1), numerous African easterly wave developed and propagated in the period 25 August onward. The propagation of the rain band produced by the MCS studied here seems to be embedded within the trough of an African easterly wave.

Figure 2.2 shows the longitude-time diagram of surface rainfall from the satellite precipitation estimates EPSAT-SG (Chopin et al., 2004; Bergès et al., 2010) and TRMM-3B42RT (Huffman et al., 2007). Both satellite estimates show a westward moving MCS propagating at a speed of  $15^\circ/\text{day}$ . Structure and time evolution of the simulated MCS are similarly described by TRMM and EPSAT products while the amount of precipitation is higher for TRMM.

Five mesoscale and two global models were involved in this model

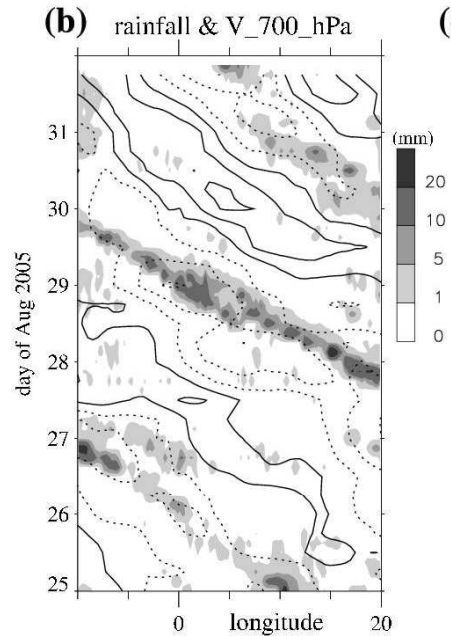


Figure 2.1: Rainfall (shaded) and meridional wind at 700 hPa (interval of  $2.5 \text{ ms}^{-1}$  between isolines). (Adapted from Guichard et al. (2010))

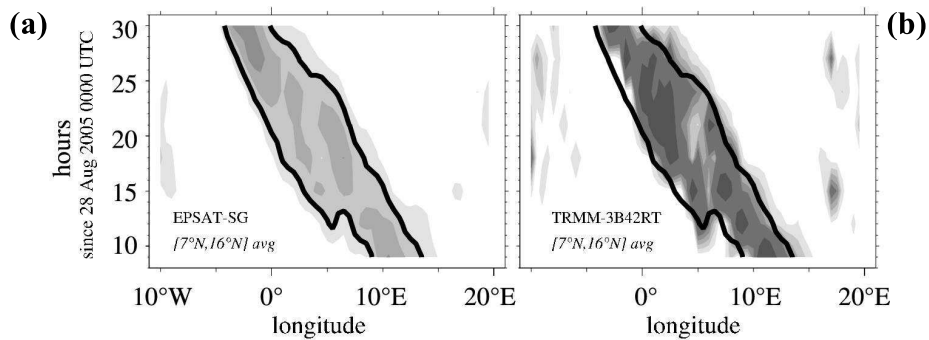


Figure 2.2: Longitude-time diagrams of surface rainfall, averaged over  $[7\text{N},16\text{N}]$ . Contour are 1,2,3,4,5,10,15 and 20. EPSAT-SG (left) and TRMM-3B42RT (right); the black thick lines delineate the area where the EPSAT-SG rainfall estimate is greater than 2 mm. (From Guichard et al. (2010))

intercomparison (see table 2.1), all the mesoscale models have been initialized with ECMWF analyses. All the mesoscale models include parameterizations, which vary in complexity, of surface, radiative, turbulent, convective and cloud processes. The size of the simulated domain differs among models, the horizontal resolution varies between ten to a few tens of kilometers, therefore, all of them made use of a parameterization scheme to describe subgrid convection.

Table 2.1: Model used, horizontal grid resolution

<i>Modelname</i>	<i>Horizontal resolution</i>	<i>Reference</i>
BOLAM	12 km	Malguzzi et al. (2006)
COSMO	28 km	Doms and Schattler (2002)
MesoNH	10 km	Lafore et al. (1997)
PROMES	15 km	Arribas et al. (2003)
WRF	12 km	Skamarock et al. (2005)
MOUM	60 km - global	Pope et al. (2000)
ECMWF IFS	35 km - global	Bechtold et al. (2008)

Figure 2.3 shows the longitude versus time plot for model precipitation, to be compared with figure 2.2. All the model simulate, as observed, a westward-moving pattern in this area, with relatively close speeds among models. However, it is not always the dominant pattern. Indeed, rainfall is predicted at night to the east of the rainfall line in most models. The rainfall line itself is less well defined in MesoNH, COSMO and ECMWF IFS. MesoNH and MOUM are also characterized by widespread daytime convection east of 5E. The BOLAM model overestimates precipitation with respect to satellite estimates but well reproduce the longitudinal extension of the MCS. Furthermore it underestimated the speed of propagation and generates an eastward shifted precipitation pattern.

This example shows that precipitation forecast in the Sahelian area is a difficult

task for mesoscale models. Despite the fact that all the mesoscale models have been initialised with the same ECMWF fields and have similar horizontal resolution, relevant differences are found with respect to satellite estimates and among model's representation of precipitation.

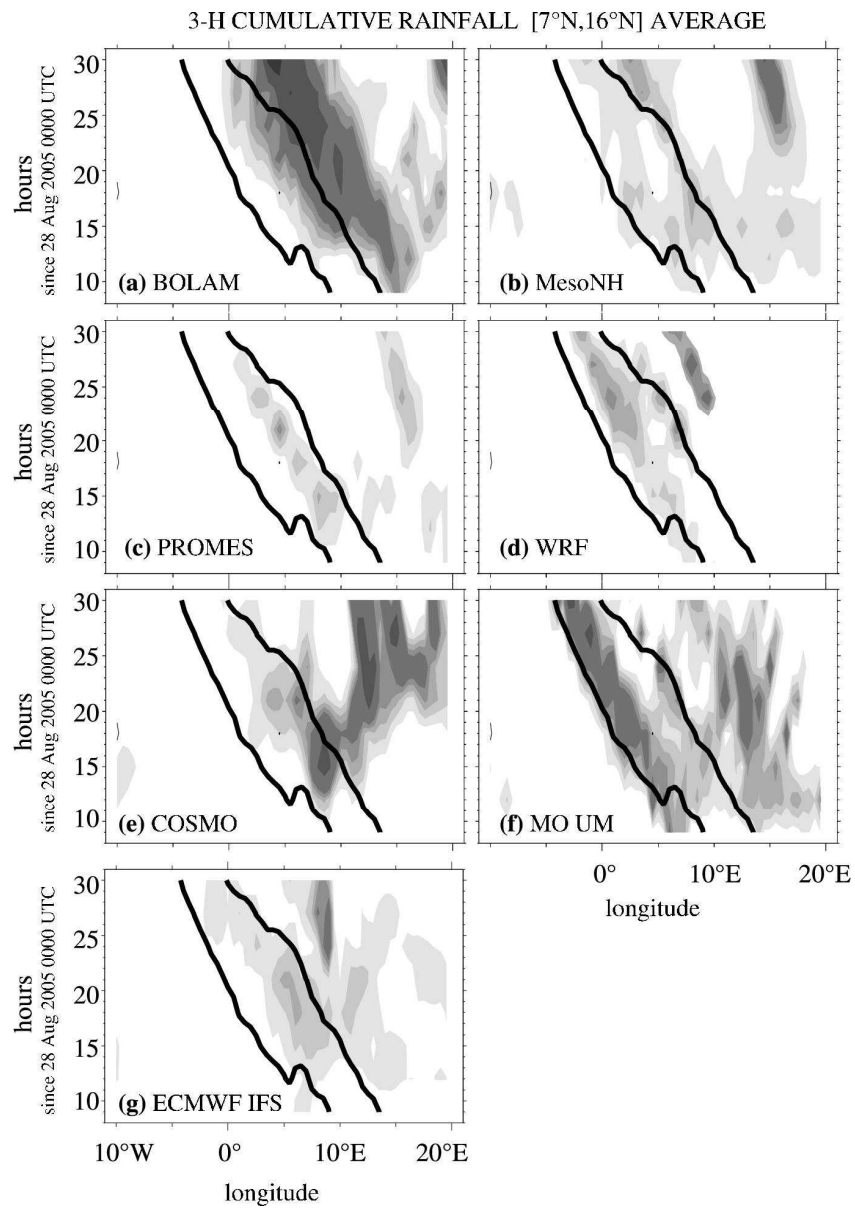


Figure 2.3: As figure 2.2 but for models. (From Guichard et al. (2010))





## Chapter 3

# How to improve the model scores? A simple data assimilation approach

In the previous chapter we showed that meteorological simulations of deep convective events and of the precipitation associated with them in West Africa is a difficult task to be addressed by mesoscale meteorological models. This because of the complex interaction between processes at different spatial and temporal scales and because of the scarcity and sparsity of atmospheric measurements in the region that lead to low reliable global analyses/forecasts used as boundary and initial conditions for mesoscale models.

In this chapter we describe the implementation of an assimilation scheme aimed at improving convective representation and precipitation. The scheme is based on the use of satellite observations of cloud top brightness temperature (CTBT) to correct the model humidity profiles. In fact the simulation of convection and precipitation is strongly dependent on an accurate description of water vapour profiles.

Firstly, observations used for the assimilation and for the evaluation of

results are presented. Then the nudging procedure is tested against an intense precipitation event occurred between 9 and 12 August 2006 in West Africa. Precipitation and cloud top brightness temperature are used to evaluate the model capability in reproducing the deep convective event.

### 3.1 Observations used

During the monsoon season in West Africa the 80% of precipitation is expected to come from mesoscale convective systems that have a time-scale ranging from 1 day to few days. Thus for assimilation purposes observations used to improve convection needs to be at sufficiently high temporal resolution.

Global datasets of precipitation from rain gauges like GPCC (Rudolf and Schneider, 2004) are sparse and have low temporal resolution (1 month). Combined satellite and ground precipitation estimates of the Global Precipitation Climatology Project (GPCP 1DD) (Huffman et al., 2001) have the advantage of being continuous in space, but have a horizontal resolution of  $1^\circ$  and a temporal resolution of 1 day. Near-real-time satellite precipitation estimates from infrared and merged infrared and passive microwave instruments have a higher temporal (6 hours to 15 minutes) and spatial ( $0.7^\circ$  to  $0.1^\circ$ ) resolution, but exhibit a low detection rate for heavy precipitation in the tropics (Ebert et al., 2007). Moreover multi-satellite measurements need to be converted into precipitation estimates by means of parameterization and calibration that could introduce errors.

In the nudging scheme developed herein CTBT from  $10.8 \mu\text{m}$  channel of SEVIRI radiometer on-board the Meteosat Second Generation Satellite (MSG) is used. It has been preferred to rainfall because its derivation from MSG radiance is a straightforward calculation and because it has higher temporal (15 minutes) and spatial (3 km at the sub-satellite point) resolutions with respect to rainfall estimates that also uses satellite radiance and has a time resolution of 3 hours and a spatial

resolution of  $0.25^\circ$  (TRMM products).

A CTBT lower than 230 K is considered as a proxy for the occurrence of deep convection following Fu et al. (1990) where is shown that very little bright-cold clouds (organised convective systems) occurs at temperature warmer than 230K and very little dull-cold cloud (thin cirrus) occurs at temperature colder than 230K. A detailed description of the method used to derive CTBT from radiance is described in EUMETSAT (2008)

To evaluate the model, CTBT, TRMM 3B42 and GPCP 1DD precipitation estimates are used. The GPCP algorithm combines precipitation estimates from several sources, including infra red (IR) and passive microwave (PM) rain estimates, and rain gauge observations (Huffman et al. (2001) and references therein). The IR data came mainly from the different geostationary meteorological satellites but data from polar-orbiting satellites were also used to fill in the gaps at higher latitudes. The IR-based estimates used the Geostationary Operational Environmental Satellite (GOES) precipitation index (GPI). The microwave data come mainly from the Special Sensor Microwave Imager (SSM/I) onboard the defense meteorological satellite program. The PM estimates were used to adjust the GPI estimate. Then the multisatellite estimate was adjusted towards the large-scale gauge average for each grid box. The gauge-adjusted multisatellite estimates were then combined with gauge analysis using a weighted average, where the weights are the inverse error variances of the respective estimates. The current products include a monthly analysis at  $2.5^\circ \times 2.5^\circ$  grids, a 5-day (pentad) analysis at the same spatial resolution, and a daily product at a special resolution of one degree.

The GPCP one-degree daily (1DD) product does not use PM rain estimates and gauge measurements directly (Huffman et al., 2001). SSM/I data were used within the framework of the threshold-matched precipitation index to delineate rain areas in the IR data. Gauge data were involved indirectly when the 1DD product was scaled so that monthly accumulations of 1DD matched the monthly

GPCP product. The monthly and pentad analyses extend from 1979 to current, while the daily product is available starting from October 1996. The daily products are made available 2 to 3 months after the end of each month.

Products from the TRMM multisatellite precipitation analysis algorithm include the 'TRMM and Other Satellites' (3B42) described in Huffman et al. (2007). The 3B42 estimates are produced 3-hourly at a spatial resolution of  $0.25^\circ$ . The major inputs into the 3B42 algorithm are IR data from geostationary satellites, PM data from the TRMM microwave imager (TMI), SSM/I, Advanced Microwave Sounding Unit (AMSU) and Advanced Microwave Sounding Radiometer-Earth Observing System (AMSRE). The 3B42 estimates are produced in four steps: (1) the PM estimates are calibrated and combined, (2) IR precipitation estimates are created using the PM estimates for calibration, (3) PM and IR estimates are combined, and (4) the data are rescaled to monthly totals whereby gauge observations are also used indirectly. This product is available for a few days after the end of each month.

## 3.2 The BOLAM model

BOLAM is a meteorological model based on primitive equations in the hydrostatic approximation. It solves the prognostic equations for wind components  $u$  and  $v$ , potential temperature, specific humidity and surface pressure. Variables are defined on hybrid coordinates and are distributed on a non-uniformly spaced Lorenz grid. The horizontal discretization employs geographical coordinates, with latitudinal rotation on an Arakawa C-grid. The model implements a weighted average flux scheme for three-dimensional advection. The lateral boundary conditions are imposed by means of a relaxation scheme that minimizes wave energy reflection. The microphysical scheme has five prognostic variables (cloud water, cloud ice, rain, snow and graupel), as derived from the one proposed by Schultz (1995). Deep convection is parameterized with the scheme of Kain-Fritsch (Kain and Fritsch, 1990; Kain, 2004). The boundary layer scheme is based on the mixing length assumption and the explicit prediction of turbulent kinetic energy (Zampieri et al., 2005), while the surface turbulent fluxes are computed according to the Monin-Obukhov similarity theory. The parameterization of the effects of vegetation and soil processes (Pressman, 1994) is based on the water and energy balance in a four-layer soil model, and includes the diagnostic computation of skin temperature and humidity, seasonally dependent vegetation effects, evapotranspiration and interception of precipitation. The radiation is computed with a combined application of the scheme from Ritter and Geleyn (1992) and the operational one from the ECMWF (Morcrette et al., 1998). Further details of the model are provided in Malguzzi et al. (2000).

## 3.3 Description of the MCS event

The event used to perform the test of data assimilation is characterised by the development of two large mesoscale convective systems observed in the Sahelian

region from 9 to 12 August 2006. It has been chosen because is one of the strongest convective event of the 2006 monsoon season and because a validation of the nudging scheme for this case of intense precipitation was useful for the analysis of aircraft measurements presented in chapter 5.

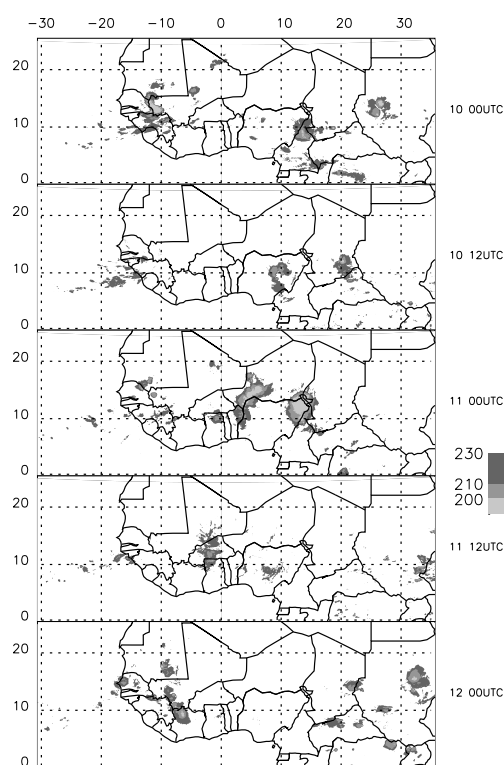


Figure 3.1: Meteosat cloud top temperature from 00 UTC 10 Aug. to 00 UTC 12 Aug. 2006, every 12 hours. Colour scale in K.

Figure 3.1 shows the CTBT derived from channel 10.8 of the SEVIRI instrument on-board the Meteosat Second Generation Satellite (MSG). The top panel refers to 00 UTC 10 August 2006 and the interval between two images is 12 hours. Two systems are clearly visible in the top panel: a westward system (WS) around 13E 10N and an eastward system (ES) around 26E 13N. The WS has a lifecycle longer than two days, with a decreasing phase at 12 UTC 11 August, followed by regeneration. Its approximate speed of propagation is 11 m/s and the minimum

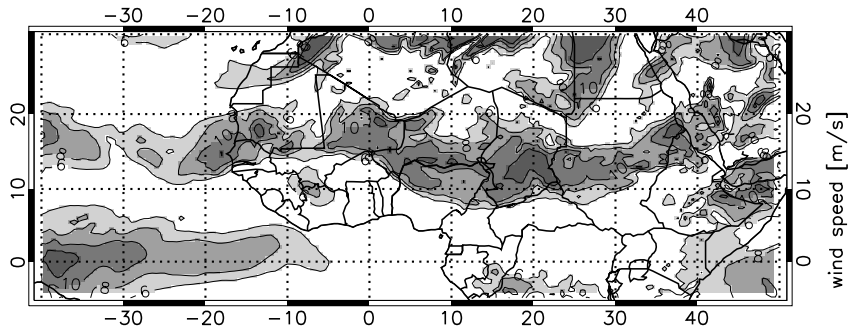


Figure 3.2: ECMWF analysis of wind speed at 700hPa on 00 UTC 10 Aug. 2006.

CTBT is 190K. The ES has a shorter lifecycle of 36 hours and dissolves over northern Nigeria around 12 UTC 11 August. Its propagation speed is similar to that of the WS system and its minimum brightness temperature is 185K.

The generation of these large systems is related to the intense monsoon flow, which is well established, providing favourable conditions for the generation of convection. The relationship of the observed MCS with the AEW activity is less clear. The wavelet decomposition presented in Janicot et al. (2008) shows that the AEW activity during the 2006 monsoon season was divided into three peak periods: mid-June, mid-July and from mid-August to mid-September. According to Janicot et al. (2008), the analysed event occurs in a period of low AEW activity. However, it is possible to identify the wave structure in the western part of the Sahelian region. Figure 3.2 shows the ECMWF (European Centre for Medium-range Weather Forecast) analysis of wind speed on 10 August at 00 UTC at 700hPa, considered as the altitude of maximum AEW intensity. A trough of an AEW is visible over South Mali. The ECMWF analysis 24 hours later (not shown) indicates that the wave moves westward toward Senegal. Nevertheless, it is difficult to relate the generation of the observed systems directly to this wave event.

### 3.4 Nudging procedure and simulation set-up

The nudging scheme is based on the approach proposed by Davolio and Buzzi (2004) (which is an evolution of the Falkovich et al., 2000 approach), focusing on the nudging of precipitation in extratropical regions. The scheme is modified here to deal with intense convective precipitation in the West African monsoon season: (1) the separation between convective and stratiform precipitations is not included and (2) the scheme assimilates the CTBT derived from the SEVIRI infrared channel centred at 10.8 micrometers, instead of precipitation. This has the advantage of a high spatial and temporal resolution and overcomes the uncertainty associated with precipitation estimates (Ebert et al., 2007).

The nudging procedure compares brightness temperature observed from satellite and evaluated by BOLAM and makes the appropriate modifications on the model specific humidity profile. Modifications are made when the temperature difference exceeds 2 K and when model or observed brightness temperatures are below 230 K, the latter condition to select only the grid points where precipitating deep convection occurs or is forecast by the model (Fu et al., 1990). The model-derived CTBT is estimated with the RTTOV-8 (Saunders et al., 2005) radiative transfer model from BOLAM water vapour, temperature and hydrometeors profiles.

The mixing ratio  $q(k)$ , evaluated by BOLAM at each model level  $k$  and each grid point, is modified for the grid-point column selected for nudging according to the following equations:

$$q(k) = q(k)^{model} + \Delta q(k)^{nudg} \quad (3.1)$$

$$\Delta q(k)^{nudg} = -\nu(k)\tau^{-1}[q(k)^{model} - \varepsilon q^{sat}(k)] \times \Delta t \quad (3.2)$$

where  $q^{sat}$  is the saturation mixing ratio with respect to liquid water above 0° C. Below 0° C a mixed phase cloud is considered and  $q^{sat}$  is evaluated using



a combination of saturation mixing ratio over liquid water and ice from Tetens' formulas.

$\nu(k)$  is a weighting function that identifies the portion of the vertical profile modified by the nudging procedure. Parameter  $\nu$  is set to 1 between the ground and 700 hPa, and then decreases to 0 at 500 hPa following a cubic law, remaining equal to 0 up to the top of the domain.

Parameter  $\tau$  is the relaxation time that determines the intensity of nudging, it has been varied to test the sensitivity of BOLAM to the nudging scheme. The values used for the test are 2, 4 and 10 hours.

The sign and intensity of the modification applied to the moisture profile depend on the term in the square brackets in Equation (3.2). If BOLAM CTBT is greater than the satellite one (less intense convection), parameter  $\varepsilon$  in equation 3.2 is set to 1 and the humidity profile is increased toward its saturation value. In the opposite case,  $\varepsilon$  is set to 0.5 and the profile is decreased toward a sub-saturated condition. The subset of grid points where the nudging is applied and the value of parameter  $\varepsilon$  are determined by the comparison between model and satellite CTBT, performed every 20 minutes, while the satellite data are updated once per hour. The modification to the moisture profile is applied after the evaluation of the term in the square brackets of Equation (3.2), which is done for every integration timestep. This allows a smooth forcing of the model and the reduction of the forcing term, if the model profile approaches the target profile  $\varepsilon q^{\text{sat}}$ .

A set of simulations was defined, using nudging with different assimilation periods and relaxation times, while a simulation without nudging was used as reference for the assessment of nudging impact. All simulations cover a period of three days from 00 UTC 09 August 2006 to 00 UTC 12 August 2006: better performances are obtained with a three day simulation starting when the two MCSs began to develop, in order to include their complete life cycle. Initial and lateral boundary conditions are interpolated from the ECMWF 6-hourly analyses

at  $0.5^\circ \times 0.5^\circ$  horizontal resolution and at 91 vertical levels.

The BOLAM model (described in section 3.2) is run with 38 vertical hybrid levels, from the ground to the top of the atmosphere (0.1 hPa), with denser levels near the ground. The horizontal domain chosen for the simulation has  $300 \times 220$  grid points with a horizontal resolution of 12 km ( $0.108^\circ$  in rotated coordinates). The domain covers the region of the analyzed convective systems life cycle and ranges from 8W, 25E in longitude and from 2S to 23N in latitude. The large distance covered by Sahelian MCSs, due to their speed of propagation, requires the use of a large domain to describe their whole lifecycle, and, as a practical consequence, a reduced horizontal resolution. Thus convection cannot be explicitly resolved in the model and the use of a convective parameterization is needed.

The values of the nudging window and the relaxation times are given in Table 3.1. Assimilation of CTBT through the nudging scheme starts after one day of free model integration (00 UTC of 10 August). According to sensitivity studies, a longer assimilation period does not improve the model performance nor the duration of improvements due to assimilation in the last day of simulation. The Nudg-24h-2 and Nudg-48h-2 simulations will be used to evaluate the impact of nudging duration on the rainfall and convective life cycle. The Nudg-24h-2, Nudg-24h-4 and Nudg-24h-10 experiments will be used to evaluate the sensitivity to the relaxation time  $\tau$  defined in Equation 3.2

Table 3.1: Characteristics and names of the simulations

	Relaxation time $\tau$		
Nudging endurance	2 hours	4 hours	10 hours
24 hours	<i>Nudg-24h-2</i>	<i>Nudg-24h-4</i>	<i>Nudg-24h-10</i>
48 hours	<i>Nudg-48h-2</i>		
No nudging	<i>Free-run</i>		

### 3.4.1 Sensitivity tests

In the present section we investigate the response of the BOLAM model to the modification of the weight assigned to the forcing term modulating the moisture profile. We focus on the sensitivity to the relaxation time  $\tau$ , since it has a strong impact on the scores considering CTBT. The tests were run only on the 24 hour nudging simulations. The values tested for the  $\tau$  parameter are 2, 4 and 10 hours. A further aim of the work was to assess the feasibility of producing accurate analyses based on radiance temperature nudging. Since  $\tau$  determines the intensity of nudging, it is crucial to choose a smooth relaxation of the model towards the observations, for a long period of nudging. Fractional Skill Score (FSS, Robert and Lean 2008) was used to evaluate the performance of the model, in terms of CTBT (and rainfall in the following section). FSS scores belong to the verification methods based on fuzzy logic (Ebert, 2008), which relax the requirement for exact matches between forecasts and observations, using instead a spatial window or neighbourhood surrounding the forecast and observed points.

The percentage of grid points over the domain with CTBT under 220K is shown in the left panel of Figure 3.3 for the three analyzed simulations. This temperature threshold was chosen to evaluate the performance of the model in reproducing deep convective events, because 220K roughly corresponds to a cloud top above 12.5 Km height (Schmetz, 1997). In both panels the vertical lines indicate the start and the end of the assimilation period. In left panel it can be seen that the best matching between the MSG data is obtained with the simulation Nudg-24-2 for the first 62 hours of the run, after which an underestimation of the area covered by convection is visible. The right panel in Figure 3.3 shows the time evolution of the FSS score during the nudging period. It shows higher values for the maximum and a more rapid increase of the score for lower relaxation times. On the third simulation day, when the nudging scheme was inactive, the best performance of the model is still obtained with the experiment that has the lowest relaxation time, since the

simulation with  $\tau=2$  h shows the longest endurance of the improvement due to nudging. Such behaviour can be explained by the fact that a lower relaxation time implies a stronger forcing of the model toward the target given by the observations. Nevertheless, it must be stressed that the nudging directly modifies the water vapour content only in the lower troposphere, and a substantial agreement with a derived variable like infrared CTBT should be considered as a validation of the nudging approach. Thus, in the analysis below, we use the value of  $\tau=2$  h for both the 24 hour and the 48 hour nudging experiments.

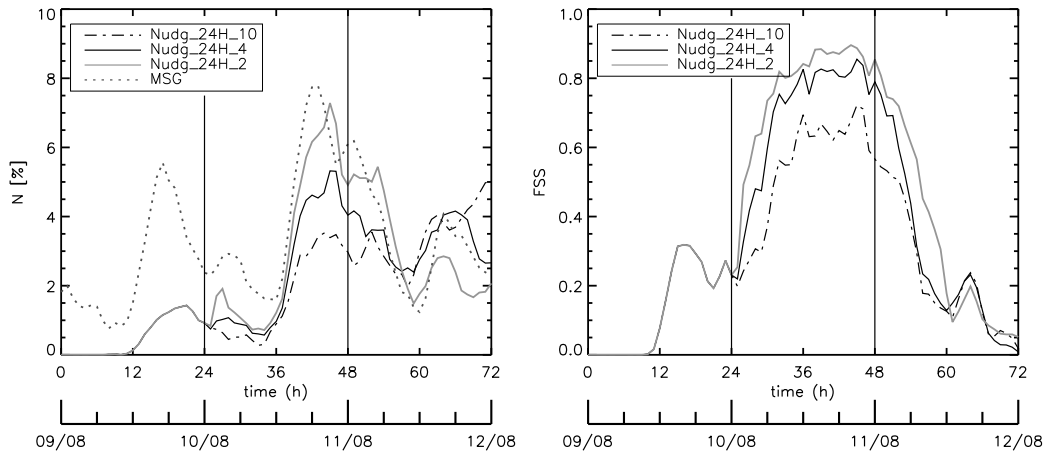


Figure 3.3: Evolution in time of the percentage of grid points characterized by a CTBT exceeding 220 K [left panel]. FSS score versus time for CTBT, temperature threshold is 220 K and spatial window is 60 Km [right panel].

## 3.5 Comparison of simulated MCS lifecycle with observations

### 3.5.1 Cloud top brightness temperature

The first objective was to evaluate the spatial and temporal distribution of the convective systems reproduced by the Free-run and the nudged simulations. The purpose was to assess the impact of the nudging procedure on the convective system representation and to evaluate the duration of the improvements derived from nudging. The evaluation here was carried out using observed and model-derived CTBT, because it is a good proxy for the intensity of convection. The simulations analyzed were Nudg-24h-2, Nudg-48h-2 and the Free-run; it has been chosen to use  $\tau=2$  h because it gives the best scores for CTBT, compared to the other relaxation times tested, as discussed in Section 3.4.1.

The CTBT at 18 UTC 10 August 2006 for the three simulations and MSG observations are shown in Figure 3.4. The Westward mesoscale convective system (WS) and Eastward one (ES) are visible in the observations (top left panel) over northern Nigeria (WS) and southern Chad (ES), respectively. The ES appears to be more intense in terms of brightness temperature and area coverage. Sparse intense convective activity is also observed in northwestern Niger, Eastern Mali and Burkina Faso. The brightness temperature from the Free-run (Fig. 3.4, top right panel) is severely underestimated: convective systems in the latitude belt ranging from 5N and 15N appear to be smaller, less intense and less organised than observed. The Free-run simulation reproduces two distinct areas of intense convection: a western one over Nigeria, which is southerly displaced and less intense compared to satellite observations; an eastern one over southern Chad, now reproduced as sparse and intense convective activity and displaced eastward.

Nudg-24h-2 and Nudg-48h-2 (Fig. 3.4, bottom panel) are identical, since the nudging process is still active at the analyzed time for both simulations.

The nudging provides a substantial improvement on the MCS distribution and propagation. Both the position and the overall structure of ES and WS agree well with observations, even if the simulated MCSs are more scattered. The BOLAM brightness temperatures now lies within the same range as the MSG ones, even if the area covered by the MCS seems to be underestimated. The nudging reduces the cloud coverage and the intensity of the unrealistic convective activity at the boundaries between Nigeria and Cameroon, and allows the generation of small MCSs in the northern part of the domain.

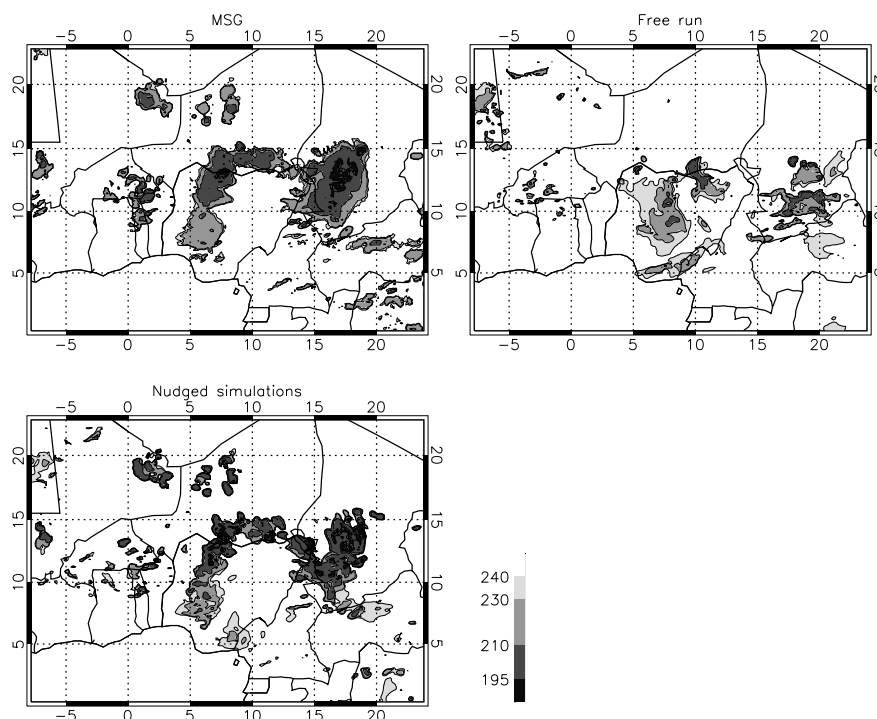


Figure 3.4: Cloud top temperature at 18 UTC 10 Aug. 2006. MSG (top left), Free-run (top right), nudged simulations (bottom left). Colour scale is in K.

Figure 3.5 shows the observed and simulated brightness temperature at 18 UTC 11 August. It should be stressed that the simulation Nudg-24h-2 had 18 hours of run without assimilation after the 24 hour nudging, while Nudg-48h-2 was still

forced with MSG data. The observations show that the WS system is located in the 9N-18N belt around 5W longitude. The WS is weakening (as displayed by the lower BT values), while the ES is nearly dissolved, except three smaller cloud systems located above Benin and western Nigeria. Apart from the WS system and a small one in middle of Chad, convective activity north of 10N is absent. The Free-run simulation (Fig. 3.5, top right panel) shows a much more intense convective activity than the satellite. It reproduces organized convective activity in three areas, plus some small and intense convective systems.

The bottom left panel of Figure 3.5 (Nudg-24h-2) shows the evolution of the WS and the ES described above. The former is located between 10N and 17N and between 5W and 0, while the latter is the convective complex with its highest convective activity centred at 13N 5E. Both systems have moved slower than the observed ones and are slightly displaced northward. As regards the system evolving from the ES, it is still in an active (and intensifying) phase, rather than in a decreasing phase, as observed in the satellite data. The Nudg-48h-2 simulation (Fig. 3.5, bottom right panel) is in better agreement with the observations, as expected, since the nudging process is active throughout the entire run. Nevertheless, the 48 hour nudged simulation does not completely dissipate the WS, as in the case of Nudg-24h-2 simulation.

Figure 3.6 shows the 12.5 percentile of grid points where the CTBT exceeds the thresholds of 210K, 220K, 230K and 240K, for each fixed longitude in the domain, as a function of time. The cloud fraction colder than the threshold from MSG observations (Fig. 3.6, upper left panel) shows the time and longitude evolution of the two large MCSs described in section 2. Both systems are characterized by a marked diurnal cycle with development of convection after 12 UTC, a maximum around 18 UTC and a rapid decrease from 6 UTC to 12 UTC. This is in agreement with the convection cycle evaluated from the MSG climatology over Africa presented in Laing et al. (2008).

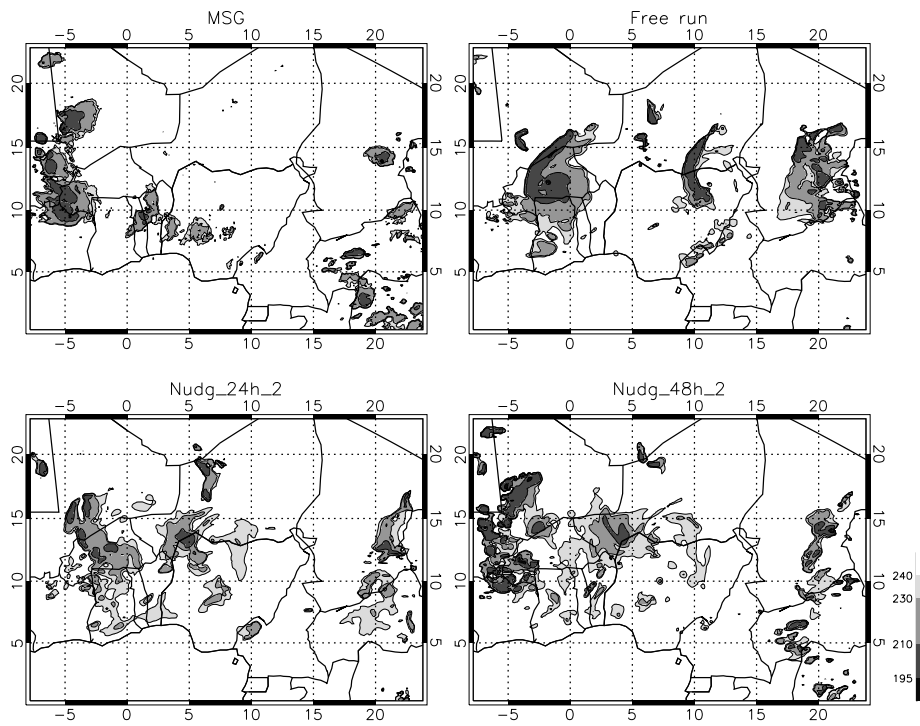


Figure 3.5: As in Fig. 3.4 but at 18 UTC 11 Aug. 2006.



The Free-run simulation (Fig. 3.6, top right panel) forms three convective systems, which propagate westward with a reduced speed compared with observations. A realistic diurnal cycle is reproduced with generation of convection at 12 UTC on each simulation day and a maximum around 18 UTC. From CTBT maps at 14 UTC (not shown), it is possible to observe that convection initiates on the lee side of the Darfur mountains, in agreement with the analyses of Laing et al. (2008) and Mekonnen et al. (2006).

The Nudg-24h-2 simulation (Fig. 3.6, bottom left panel) has a correct position and propagation speed of the MCSs during the assimilation period (00 UTC 10 August - 00 UTC 11 August). After the end of the nudging period the speed of the two systems decreases and their lifecycle is not correctly reproduced. In fact, the ES does not totally dissipate at 6 UTC 11 August, but grows again at 12 UTC 11 August, while the WS decreases after 12 UTC 11 August. In general, the convective systems reproduced during the portion of simulation without nudging are characterized, as in the Free-run, by a lower westward propagation speed, but display a diurnal lifecycle of the systems in agreement with observations. It is also possible to argue that nudging has a relevant impact throughout the run since the convection on the last day of simulation, despite the mentioned differences, seems to be more realistic than in the Free-run. Figure 3.6 confirms that the Nudg-48h-2 simulation is in good agreement with the observed lifecycle and propagation speed of the MCS, even if it can be observed that convection is still active after 6 UTC 10 August between 0E and 10E, as in the case of the Nudg-24h-2 simulation.

The left panel in Figure 3.7 shows the percentage of grid points with CTBT under 220K. For both panels the vertical lines indicate the start of the assimilation period for both the nudged simulations and the end for the Nudg-24h-2 simulation. MSG observations again show the diurnal cycle of the convective activity, which is also, at least on a qualitative basis, reproduced by all simulations. Compared to the Free-run, the amount of convection is much better reproduced when the

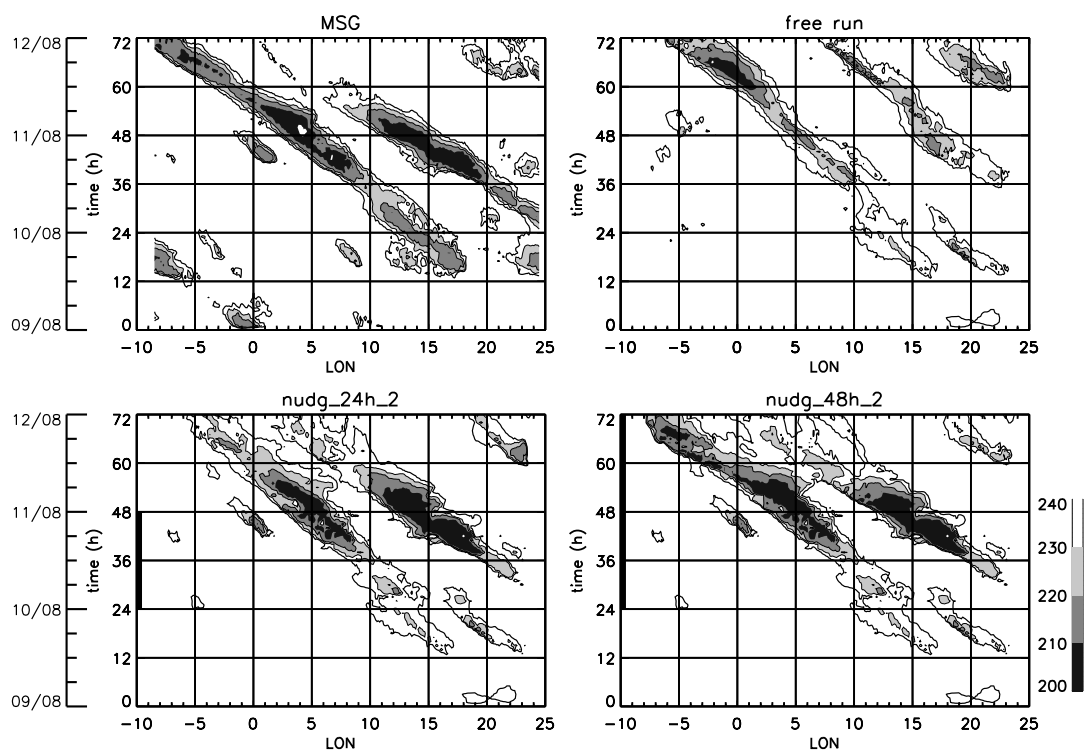


Figure 3.6: Hovmoller plots for the 12.5 percentile of grid points whose CTBT exceeds the temperature thresholds of 210K, 220K, 230K and 240K, for each fixed longitude in the domain. Solid lines in the left borders indicate the nudging period.

assimilation is applied. The Free-run underestimates the average convective activity during the first two days of the simulation and overestimates it during the last one, while the nudged simulations underestimate the convective activity for just the first 30 hours, and capture a secondary maximum at 4 UTC 10 August as well as the rapid increase after 12 UTC 10 August. It is also worth noticing that, during the third day of the run, the Nudg-24h-2 simulation still shows a better agreement with MSG observations than the Free-run does. The right panel in Figure 3.7 shows the time evolution of the FSS. A maximum threshold of 230 K to calculate the FSS is chosen to apply the score only to the model grid points where the nudging procedure was active. The FSS analysis also shows a quantitative improvement as a result of the nudging procedure. From the start of the nudging period FSS rapidly increases up to values close to 0.85, after which the FSS for Nudg-48h-2 remains higher than in the Free-run until the end of the simulation, while the FSS for Nudg-24h-2 drops to values close to those of the Free-run after 13 hours from the end of nudging. This also provides an estimate of the endurance of the improvement due to assimilation.

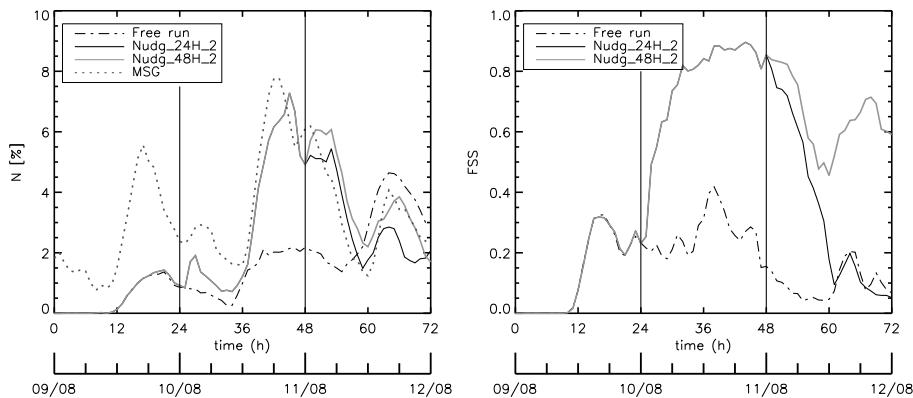


Figure 3.7: Evolution in time of the percentage of grid points characterized by a CTBT exceeding 220 K [left panel]. FSS score versus time for CTBT, temperature threshold is 220 K and spatial window is 60 Km [right panel].

### 3.5.2 Rainfall

The next step was to assess to what extent the nudging improved the spatial distribution and intensity of the precipitation field. The comparison was performed for the last 24 hours of simulations, i.e. 11 August 2006. The rainfall observations came from the daily accumulated precipitation at 1 degree of the GPCP project (Huffman et al., 2001) and from the Tropical Rainfall Measuring Mission (TRMM) (Kummerov et al., 2000) 3 hourly product at 0.25 degree of resolution. Nicholson et al. (2003 I and II) used a rain gauge database, different from the one used by GPCP and TRMM estimates, to validate both TRMM and GPCP rainfall products over West Africa on 1998. They used an horizontal resolution of 2.5 degrees and showed that GPCP relative error lies between -2% and 14% in August. They showed also that TRMM relative error is around 8% in August, considering 1 degree boxes.

Figure 3.8 shows the accumulated precipitation for GPCP, TRMM and the simulations. Both rainfall datasets show two main precipitation areas associated to the ES and WS convective systems: West of 5E and between 10E and 15E. The precipitation of the Free-run simulation is associated to the three systems described in Figure 3.5, which produce rainfall throughout the 10N-15N latitude band. The comparison between the Free-run and rainfall observations shows that the simulated precipitation is more spread, and that the geographical position of the intense precipitation ( $> 20$  mm) does not agree with the observed one.

A clear improvement is obtained with nudging for both the Nudg-24h-2 and Nudg-48h-2 simulations. The first shows a remarkable coincidence with GPCP and TRMM for the areas of intense precipitation and a general reduction of the rainfall area. The agreement is further improved with the 48 hour nudging. This result is also confirmed by the FSS score, calculated for two precipitation thresholds, 10 and 20 mm, and a longitude-latitude window of  $3^\circ \times 3^\circ$  for GPCP product and  $0.75^\circ \times 0.75^\circ$  for TRMM. FSS scores have been evaluated by remapping the BOLAM daily accumulated precipitation over TRMM and GPCP grids. The FSS

scores are reported in Table 3.2. As expected, the FSS score is in general higher for the Nudg-48h-2 simulation. The improvement is particularly relevant for the highest threshold (20 mm), where both Nudg-48h-2 and Nudg-24h-2 simulations give markedly higher scores compared to the Free-run. For the lower threshold (10 mm) the nudging still provides an improvement in terms of FSS score. Nevertheless, the difference compared to the Free-run simulation score is less pronounced, a finding that can be explained by observing that low precipitation is distributed over a larger area, located in the same latitudinal band for observations and all the simulations.

Table 3.2: FSS score for precipitation evaluated for three thresholds: 10 and 20 mm. The reference values are GPCP [top] and TRMM [bottom]. The neighbourhood window considered is  $3^\circ \times 3^\circ$  for GPCP and  $0.75^\circ \times 0.75^\circ$  for TRMM.

	<i>Nudg-48h-2</i>	<i>Nudg-24h-2</i>	<i>Free-run</i>
GPCP			
10 mm	0.88	0.74	0.65
20 mm	0.64	0.64	0.43
TRMM			
10 mm	0.77	0.58	0.43
20 mm	0.65	0.53	0.24

Table 3.3 reports the total rainfall amounts from GPCP, TRMM and the simulations. Total rainfall is the accumulated precipitation over the whole model domain for the 11 August. Three range ( $< 0.5$ ;  $0.5 \div 5$ ;  $> 20$  mm) are chosen to estimate the performance of the simulations for total, low and intense precipitation, respectively. *area* values are the percentage of grid points where precipitation lies within the above mentioned ranges. It is worth noticing that the GPCP and TRMM product does not only use MSG radiances, which are assimilated into the model, but also passive microwave satellite and gauge measurements, to evaluate

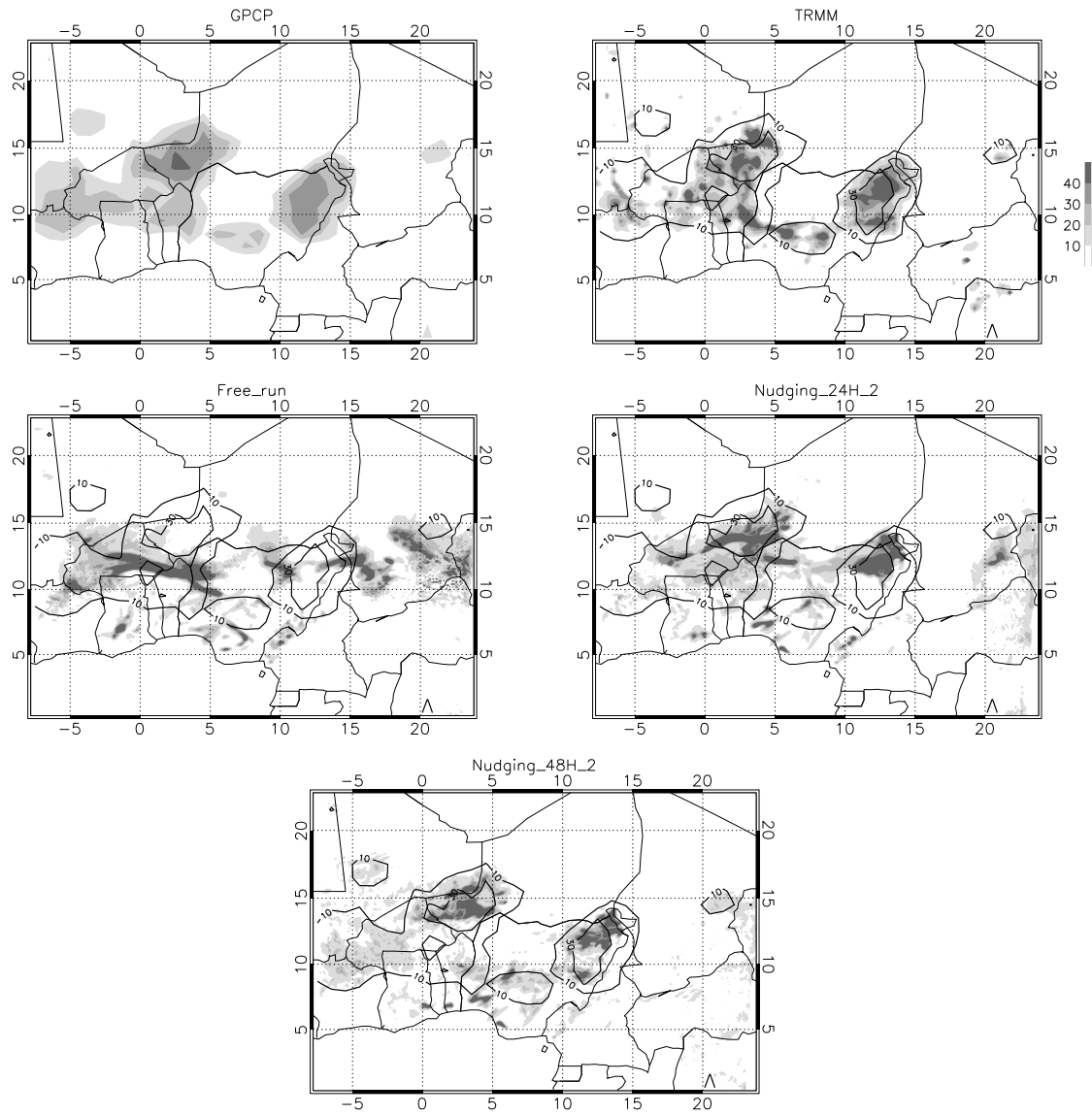


Figure 3.8: 24 hour cumulated rainfall on 11 Aug. 2006. GPCP (top left), TRMM (top right), Free-run simulation (centre left), Nudg-24h-2 (center right) and Nudg-48h-2 (bottom). Black solid contours on the three simulation panels reproduce the GPCP rainfall for the threshold of 10 and 30 mm.

the daily rainfall. Therefore the agreement between measured and model rainfall can be considered as a validation for the nudging scheme used.

Table 3.3: Total rainfall ( $10^9\text{kg/day}$ ) and percentage of domain corresponding to values of rainfall exceeding three thresholds: low ( $0.5\text{ mm} < \text{rainfall} < 5\text{ mm}$ ) intense ( $\text{rainfall} > 20\text{ mm}$ ) and total ( $\text{rainfall} > 0.5\text{ mm}$ )

		Total rain $>0.5$	Low $0.5 < \text{rain} < 5$	Intense rain $>20$
<i>Nudg-48h-2</i>	Tot	41277	5359	13603
	Area	50%	22%	3%
<i>Nudg-24h-2</i>	Tot	43241	4500	21116
	Area	43%	20%	5%
<i>Free-run</i>	Tot	48834	4570	27261
	Area	46%	21%	6%
<i>GPCP</i>	Tot	42723	3124	24384
	Area	38%	14%	9%
<i>TRMM</i>	Tot	36156	2857	22511
	Area	31%	13%	6%

We observe that total precipitation from TRMM and GPCP are different. As expected, GPCP rainfall values are higher with respect to TRMM in West Africa as showed by Nicholson et al. (2003 I). Comparison with observations shows that the Free-run and the Nudg-24h-2 simulations slightly overestimate the total rainfall, while Nudg-48h-2 precipitation lies between GPCP and TRMM values. By contrast, all simulations overestimate the area where precipitation occurs. The simulations overestimate by a factor around 1.3 the total amount of rainfall and the area interested by low precipitation ( $0.5 \div 5$ ). For intense precipitation the Nudg-24h-2 and Free-run simulations give a reasonable agreement with the observations for the total rainfall and the area while Nudg-48h-2 underestimates by a factor

around 2 both the total precipitation and the area. However, it should be stressed that in the Nudg-48h-2 simulation the nudging procedure greatly improves the precipitation distribution, as well as the position, as is clearly shown in Figure 3.8 and as can be deduced by the FSS score in Table 3.2.



### 3.6 Nudging impact on model dynamics

It is likely that the nudging of water vapour has an impact on the dynamical and thermodynamical variables of the model. So it is important to verify that such changes are coherent with the modification in MCS position and dynamics due to the assimilation procedure. Firstly, the divergence of horizontal wind field at 150 hPa has been chosen because it reveals upward vertical motion of air masses related to convective activity. 150 hPa is approximately the height where air masses decrease their vertical speed due to convective uplift and diverge from uprise column. Figure 3.9 shows divergence of horizontal wind fields together with 230 K cloud top brightness temperature isotherms for the three simulations at 18 UTC 11 August. The free-run simulation (top left panel (Fig. 3.9)) has, as expected, a coincidence of areas with low CTBT and high positive value of divergence for all the three MCS discussed in section 3.5.1. Regarding the westernmost MCS, it is worth noticing that within the 230 K isotherm two different areas can be distinguished: a front part exhibiting high value of divergence and thus strong convective uplift and the anvil part with low values of divergence at the rear. Top right and bottom panels of figure 3.9 regards Nudg-24h-2 and Nudg-48h-2 simulations, respectively. The same correlation with low CTBT and high divergence is found for both experiments. Upper tropospheric wind fields are modified by the nudging procedure with respect to the free-run even 18 hours after the end of assimilation. Both top right and bottom panels show an area with low CTBT and low divergence corresponding to the ES described in section 5.1. The divergence at 250 hPa (not shown) is higher than at 150 hPa for the ES in both the nudged simulations, revealing that these MCSs are in a decreasing phase. The analysis of the divergence at lower levels and of the related explicit vertical velocity (not shown) indicates that the model reacts to the increments on the thermodynamic variables (temperature and humidity) applied by the convective parameterization scheme with changes in the 3-D velocity field that are consistent with the cumulative effects of organized

convection in the area of interest. Therefore, the nudging scheme appears to be effective in modifying the explicit model dynamics in a coherent way.

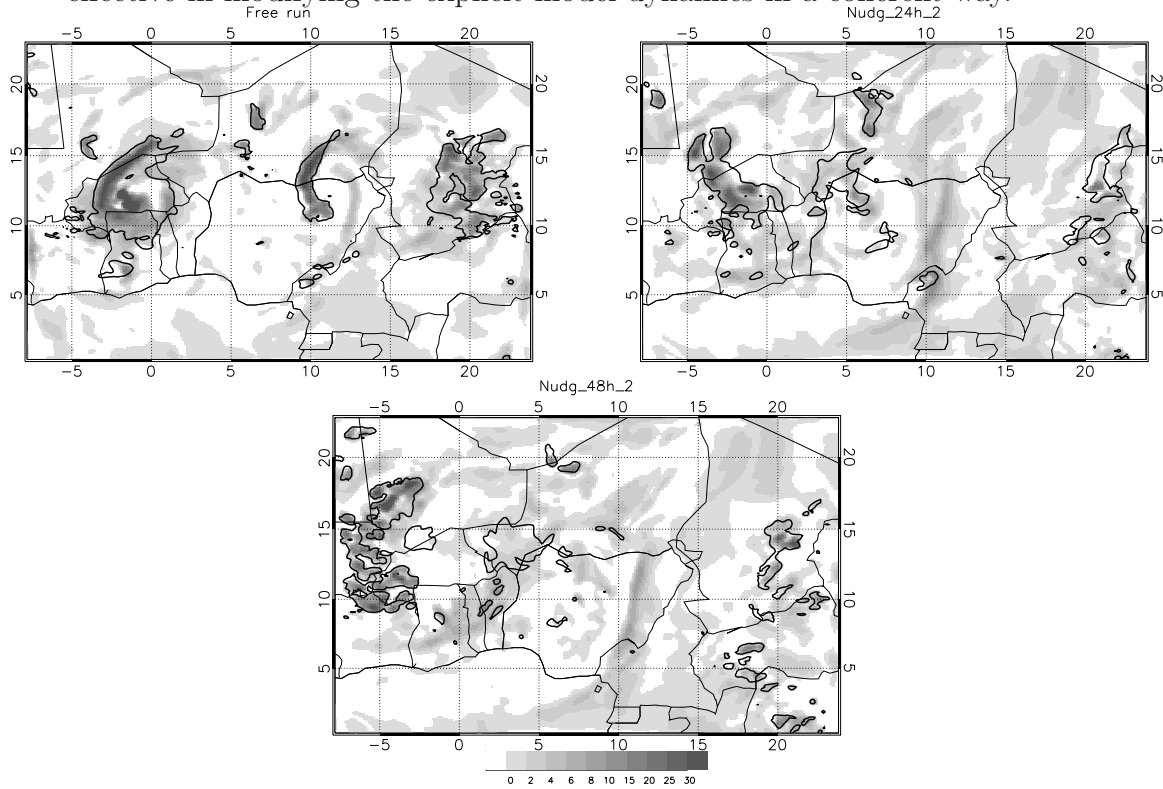


Figure 3.9: Horizontal wind divergence ( $10^{-5} \text{ s}^{-1}$ ) at 150 hPa on 11 August 18UTC. Free-run [top left], Nudg-24h-2 [top right] and Nudg-48h-2 [bottom]. Solid contours are 230 K CTBT isotherms.

In summary, in chapter 3 we proposed a method to overcome low reliability of global models' analysis and improve the performances of the mesoscale models in reproducing organised convective events. We presented the implementation into the BOLAM model of a nudging scheme which forces water vapour in the lower troposphere using CTBT observations from the 10.8  $\mu\text{m}$  channel of the MSG satellite. We tested the assimilation scheme in a case of intense precipitation due to the development of two intense MCSs occurring over West Africa during the 2006 monsoon season.

A comparison is performed among three model simulations and observations of cloud top brightness temperature (CTBT; derived from MSG-SEVIRI data) and of precipitation fields (from the GPCP daily and TRMM 3-hourly product), in order to assess the model score without assimilation and the improvement due to nudging. Two different set-up for the nudging scheme has been used: (1-forecast) the nudging is activated for one day and then switched-off for the last 24 hours of simulation. (2-analysis) the nudging is left active until the end of the simulation. Set-up (1) is used to evaluate the capability of the nudging scheme in improving the forecasting ability of the model. Set-up (2) is used to produce a reanalysis that uses CTBT to improve representation of convection.

The comparison of observed and simulated CTBT shows that the simulation without nudging underestimates intensity and area interested by convection, furthermore it shows that the position and speed of the MCSs are far from observations. Conversely, the diurnal cycle is in reasonable agreement with observations and the recent climatology given by Laing et al. (2008). Using CTBT, we estimated that the nudging procedure (in forecast set-up) has a positive impact in terms of the FSS score for 13 hours after the end of the assimilation period. The best agreement with observations is found with the analysis nudging set-up, with which the fractional skill score for CTBT remains high ( $> 0.6$  over 1.) throughout the integration period. Furthermore the position and speed of propagation of the

MCSs is close to observations.

The comparison of accumulated model and measured precipitation shows a positive impact in reducing the overestimation of total precipitation and in improving the spatial patterns for both nudging set-up. As encountered in the comparison with CTBT, the FSS scores for precipitation is highest for the analysis nudging set-up. Nevertheless, a clear improvement for the last 24 hours of simulation is also obtained for the forecast nudging set-up. Finally a comparison of horizontal wind field divergence at 150 hPa between nudged and non-nudged simulations has been performed revealing that the nudging procedure is able to modify the dynamical fields of the simulation according to the observed convection. For the forecast nudging set-up these modifications persist after the assimilation period leading to an assimilation impact quantified above.

The analysis of the simulation with forecast set-up for the nudging scheme has shown that it is possible to improve the forecasting capabilities on a time window of about 12 hours after the end of the assimilation. Thus it can be used in an operational weather forecast frame to improve at least short-range forecast of precipitation events. It has been also shown that continuous nudging can simulate a correct distribution and propagation of MCSs, also improving precipitation. This could be particularly useful for the detailed analysis of the water cycle and transport related to convection in the Sahelian region, which requires a correct positioning of MCSs and an accurate quantification of precipitation.

Future improvements of the nudging procedure could be obtained with the combined use of CTBT and satellite rainfall products, even if it would reduce the temporal and spatial resolutions of the data assimilated. A further improvement can be obtained with the use of a climatological profile in the cases of dehydration. At present a constant relative humidity profile, equal to half of the saturated value, is used to dehydratate the layer between 1000 and 500 hPa when the model produces unrealistic convective activity. A climatological profile of non-convective cases over

West Africa could be obtained and used in the whole troposphere to drive the model water vapour profile to more realistic undersaturated conditions.



# Chapter 4

## The AMMA field campaign

In this chapter we describe measurements of chemicals and aerosols performed during the AMMA field campaign and analysed in chapters 5 and 6 have been . In section 4.1 we provide an overview of the AMMA field campaign and of the mean atmospheric concentration of trace gases and aerosols during wet season 2006. For sake of comprehension of the analyses carried out in the following chapters, a review of the current literature based on aircraft and balloon measurements is presented in section 4.2. A more detailed analysis of the impact of convection on measurements collected by the high altitude research aircraft M55 Geophysica is carried out in section 4.3 and then compared with BOLAM simulation results in chapter 5.

### 4.1 Description of the AMMA field campaign

The African Monsoon Multidisciplinary Analysis (AMMA) international project aimed at improving our knowledge and understanding of the West African monsoon and the socio-economic impacts of its variability (Redelsperger et al., 2006). The achievement of the AMMA project relies on a field measurements programme which is the largest and most extensive ever attempted in Africa. Ground-based, sea-based and aircraft measurements have been performed in the frame of AMMA

field campaign which is organised in nested time-scales.

Figure 4.1 shows the time scales involved: the long-term monitoring programme (LOP, 2001-2009) based on existing infrastructure; Enhanced Observing Period (EOP, 2005-2007), which saw the implementation of specific land-based and sea-based instruments; Special Observing Periods (SOPs) in 2006, when intensive land-based, sea-based, aircraft and balloons measurements took place.

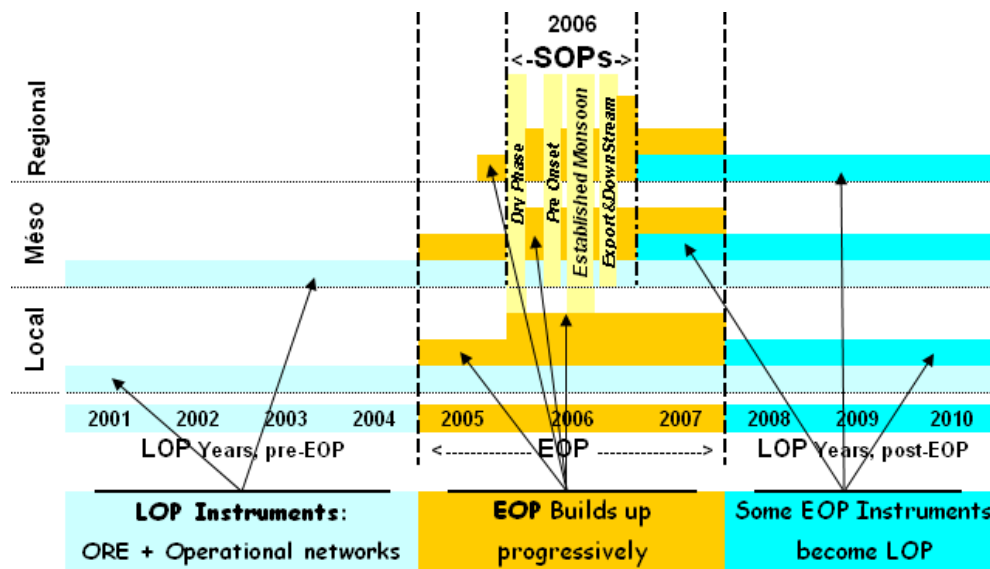


Figure 4.1: Space-time schematic of the AMMA observation programme. (From Lebel et al. (2009b))

The objective of LOP is to document and analyse the interannual variability of some components of the WAM which have characteristic long time-scales (sea-surface temperature and salinity, ground water balance, vegetation dynamics, anthropogenic forcing). Radiosoundings network active during the LOP is shown in figure 4.2(a).

EOP is designed to provide a detailed documentation of the annual cycle of the surface and atmospheric parameters from convective scales of a few kilometres up to regional scales. The regional coverage is obtained through various actions including a restoration and upgrade of the operational networks, the installation of



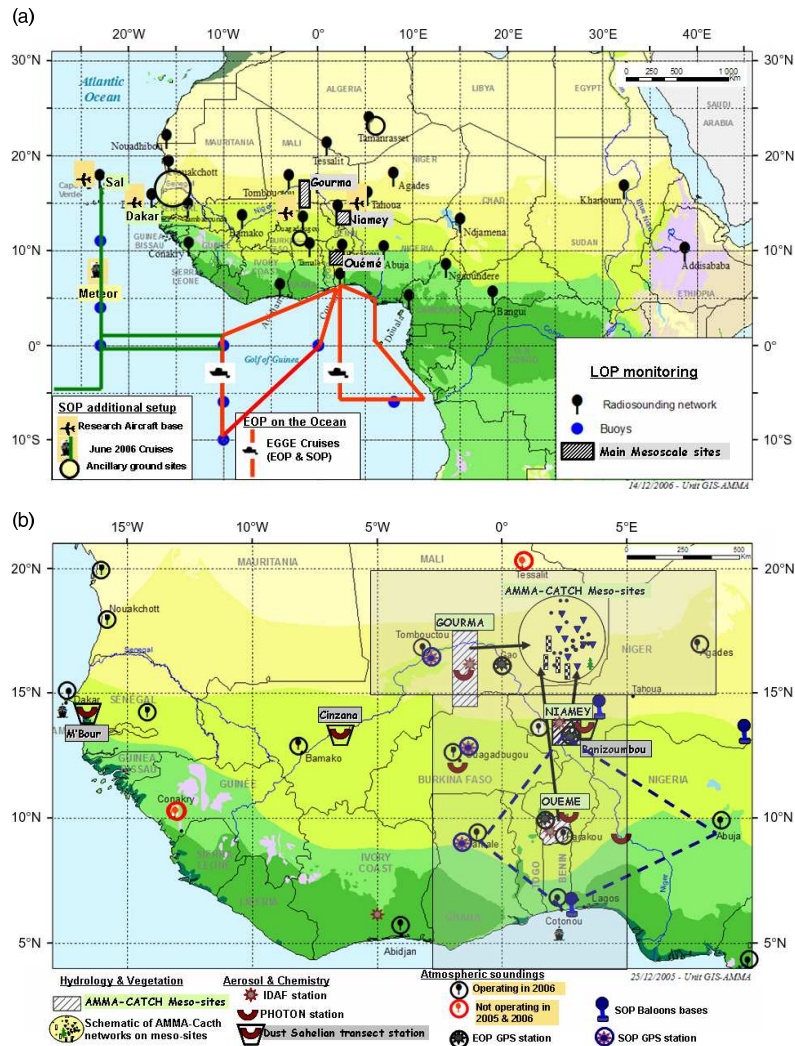


Figure 4.2: The AMMA measurement network. Panel (a) shows cruises performed with research ship during both the EOP and SOP periods, research aircraft bases activated during the SOP together with radiosounding network active during the LOP. In panel (b) balloon sounding bases operating during EOP in Niamey and Cotonou are shown. Grey shaded areas represent the AMMA-CATCH (AMMA-Coupling the Tropical Atmosphere and the Hydrological Cycle) sites of Gourma, Niamey and Oueme. (From Lebel et al. (2009b))

new instruments and two annual cruises with research vessels (see figure 4.2(a)).

SOP focused on specific processes and weather systems at various key stages of the annual cycle of the WAM, with intensified observations occurring over the following periods: (1) the dry season (SOP0; 10 January-20 February), (2) Monsoon onset (SOP1; 15 May-30 June), (3) Peak monsoon (SOP2; 1 July-30 August) and (4) Late monsoon (SOP3; 15 August - 30 September).

SOP1 and SOP2 represent the core of the AMMA observational programme and were aimed at the most intensive study of the physical processes, and associated biochemical processes, which control the monsoon during the wet season. The main scientific objectives of SOP1 and SOP2 were to obtain a comprehensive description of: (1) atmospheric dynamics on time-scales ranging from hours to a few days; (2) land-atmosphere coupling, including rainfall feedback with soil moisture and with vegetation and the control of biogenic chemical emissions by vegetation and soils; (3) water cycle processes, coupled between the land, ocean and atmosphere systems; (4) chemical and aerosol processes, including emission from the land and ocean, transport and transformation in the atmosphere and lower stratosphere.

To accomplish the latter objective a multi-aircraft and a balloons campaigns took place over West Africa. Measurements on board 5 research aircraft and almost daily balloon launches from three bases provided the first detailed, in-situ, characterisation of the chemical composition of the troposphere and lower stratosphere in this region. Figure 4.2(a) shows the research aircraft bases in Ouagadougou and Niamey while balloons measurements bases active during SOP are shown in figure 4.2(b). The research aircraft, widely used in this study, were equipped with instruments to make measurements of ozone (O<sub>3</sub>), many of its precursor species (e.g. carbon monoxide (CO), nitrogen oxides (NO<sub>x</sub>) and volatile organic compounds (VOCs), as well as photochemical products (e.g. radicals species and oxygenated VOCs (OVOCs) and aerosols (for a comprehensive overview of balloon and aircraft payloads see Cairo et al. (2009)).

Previous in-situ observations in this region, during the wet season, have been confined to the MOZAIC programme (Measurements of OZone, water vapour, carbon monoxide and nitrogen oxides by in-service AIRbus airCRAFT Marenco et al. (1998)), which involved measurements on commercial aircraft flying in the upper troposphere, with vertical profiles at airports of Abidjan, Ivory Coast and Lagos, Nigeria (Sauvage et al., 2005). The MOZAIC measurements have been limited to O<sub>3</sub>, CO, water vapor and total odd nitrogen (NO<sub>y</sub>). Other field campaign have been devoted to measure biomass burning emissions in West Africa during the dry season (DECAFE -Dynamic and Atmospheric Chemistry in Equatorial Forest-(Delmas et al., 1995), (Fontan et al., 1992); TROPOZ -Tropospheric Ozone Campaign- (Jonquieres et al., 1998)); furthermore measurements in Central and Southern Africa have also focussed on the dry season when there is widespread biomass burning (SAFARI -Southern African Fire Atmosphere Research Initiative-(Swap et al., 2002); DECAFE (Fontan et al., 1992), (Andreae et al., 1992)).

In this chapter we focus on the Special Observational Period 2 (SOP2), which targeted the monsoon maximum in July and August 2006 with the aircraft instrumented for chemical measurements. During July and August 2006 five research aircraft made comprehensive chemical measurements from the boundary layer to the lower stratosphere (around 50 hPa), from 2N to 21N, and between 10W and 7E (Figure 4.3).

Three research aircraft used were based in Niamey, Niger: NERC BAe-146 (Natural Environment Research Council, [www.nerc.ac.uk/](http://www.nerc.ac.uk/)); CNRS Falcon and ATR (Centre National de la Recherche Scientifique, [www.cnrs.fr](http://www.cnrs.fr)). Two in Ouagadougou, Burkina Faso: DLR Falcon (Deutsches Zentrum für Luft und Raumfahrt, [www.dlr.de](http://www.dlr.de)) and Geophysica M55.

The horizontal and vertical ranges covered by each aircraft are illustrated in figure 4.3. The ATR focussed on the lower troposphere, the BAe-146 on the lower and mid-troposphere, the two Falcons on the upper troposphere and the

M55 on the upper troposphere/lower stratosphere (UTLS). In combination aircraft measurements provide coverage throughout the full depth of the troposphere and the lower stratosphere.

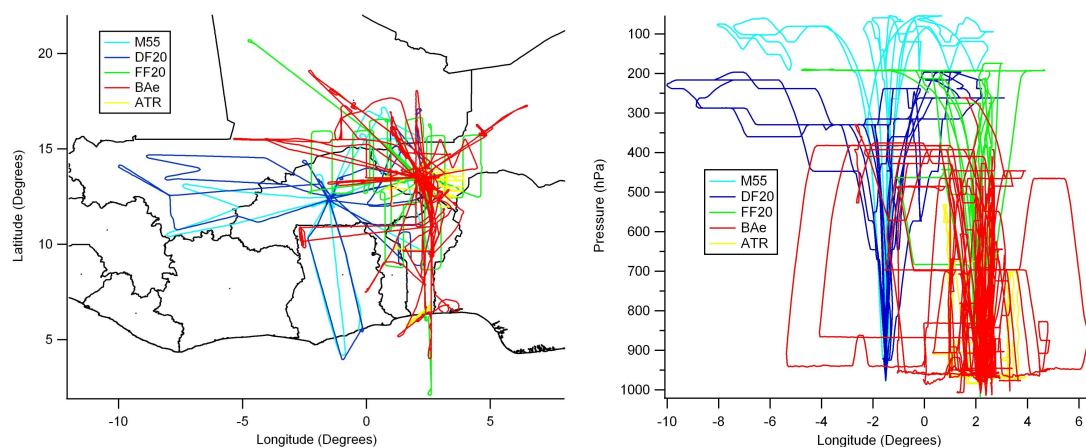


Figure 4.3: Longitude-latitude [upper panel] and longitude-pressure [lower panel] plots of the 5 research aircraft flights tracks during SOP. Reeves 2010, personal communication.

## 4.2 Aircraft campaign background

Here we focus on the results from the M55 campaign data that are most extensively analysed in this study. Further details on the payloads and instrumental features are given in Cairo et al. (2009). The strategy adopted for the aircraft measurement was to perform various types of flights to sample different air masses: (1) affected by recent deep convective outflow (2) influenced by polluted plumes transported from both southern hemispheric wild fires and from the Asian monsoon region (3) loaded with local biogenic and anthropogenic emissions and (4) representative of background concentrations.

Five local flights and one transfer flight have been performed by M55 Geophysica aircraft and flight tracks are reported in figure 4.4. Flight paths on 1 and 16 August are the transfer flights between Marrakesh and Ouagadougou. Flights going more southward (4 and 13 August) were aimed to provide background concentrations and sample air masses impacted by long range transport of biomass burning plumes and Asian monsoon air masses respectively. Two flights (8 and 13 August) have been performed to sample the atmosphere over the same trajectory and at the same time of the CALIPSO (Cloud-Aerosol Lidar and Infrared Pathfinder Satellite Observation) satellite overpass to compare measurements taken from the aircraft and the satellite and validate the satellite products. Two flights were specifically dedicated to the sampling of air masses influenced by recent MCS outflow (7 and 11 August), moreover almost all the flights included a dive at 200 hPa to make measurements in the main convective outflow (4.3 right panel). Figure 4.5 shows profiles of  $\text{H}_2\text{O}$ ,  $\text{CO}$ ,  $\text{CO}_2$ ,  $\text{O}_3$ ,  $\text{NO}$  and particles with diameter greater than  $14 \mu\text{m}$  ( $\text{N}_{14}$ ) measured on board of M55 during the 5 local flights of the AMMA field campaign in 2006.

Deep convection is very effective in transporting air-masses from the lower troposphere to the lower part of the tropical tropopause layer (TTL). It can impact the upper part of the TTL via 2 main mechanisms: convective uplift of air masses

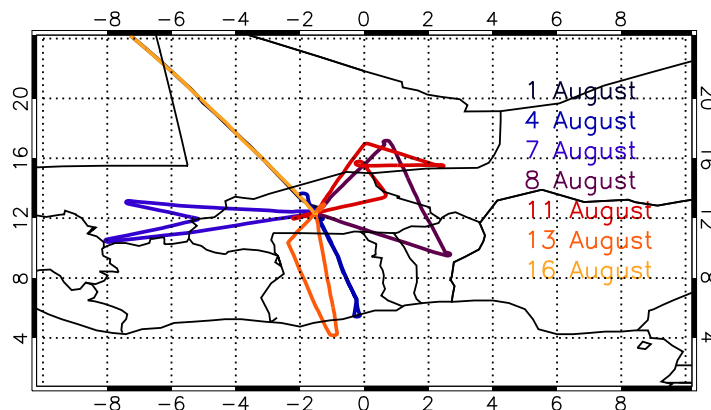


Figure 4.4: Flights tracks of M-55 Geophysica research aircraft.

up to the level of neutral buoyancy, followed by slow uplift due to dynamical forcing and radiative heating, and direct injection within lower stratosphere. Which is the more efficient mechanism among the two is still question of debate (Fueglistaler et al., 2009).

Signatures of convection can be identified as deviations of tracer concentrations from mean profile due to rapid vertical transport from the planetary boundary layer. The typical effect of deep convection is to pull boundary layer air-masses at the level of convective outflow, leaving almost unperturbed the air-masses at intermediate tropospheric levels. Because each of the chemicals used to asses the role and importance of convective transport is expected to have different mean vertical profile, signatures of convection are different for each chemicals. For a chemical with a mixing ratio that is constant with height, vertical mixing would not lead to any changes in mixing ratios and thus it would not be possible to infer any information about deep convective transport.

Ozone profile measured far from ozone precursors sources is expected to slowly increase with height in the troposphere and then to quickly increase in stratosphere because of to the fotodissociation of molecular oxygen. The minimum in the boundary layer and the slow increase in the troposphere is due to the fact that the principal sink of ozone is surface deposition. The effect of deep convection on

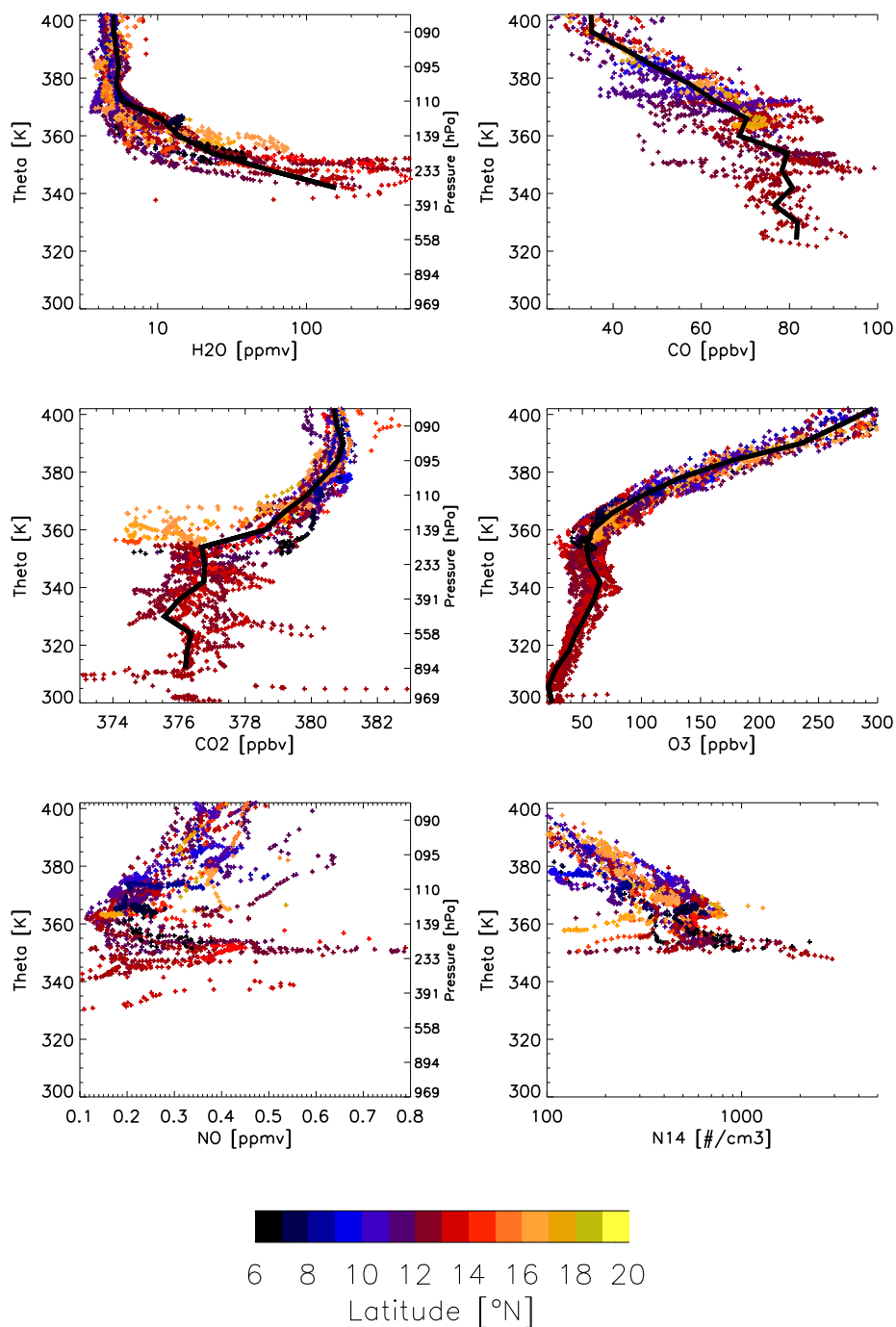


Figure 4.5: Profile of H<sub>2</sub>O, CO, CO<sub>2</sub>, O<sub>3</sub>, NO and particles with diameter greater than 14  $\mu\text{m}$  measured on board of M-55 during the 5 local flights of the AMMA field campaign in 2006. Colours indicate latitude. Black thick line is the mean profile.

such a kind of vertical profile lead to a decrease in ozone mixing ratios at the level of mean convective outflow. In the tropical areas deep convection frequently occurs leading to the typical S-shape profile for ozone. This is more clearly visible over areas where boundary layer concentrations are weakly influenced by anthropogenic and biogenic sources of ozone precursors (for instance Pacific Ocean) (Fueglistaler et al., 2009).

In West Africa anthropogenic and biogenic emissions, together with long-range transport of ozone enriched air-masses from middle-east, India and southern Africa, lead to a less pronounced S-shape mean vertical profile. In fact, M55 sampled several typologies of air masses with both enhanced or reduced values of CO, CO<sub>2</sub> and O<sub>3</sub> concentrations depending on the emissions in the region where convection occurred and subsequent chemical processing in the upper troposphere. O<sub>3</sub> profiles measured during AMMA over West Africa by Fast Ozone Analyzer (FOZAN) are reported in figure 4.5 middle-right panel. As expected the S-shape of the mean profile (black line in figure) is clearly visible even if is less pronounced than over an area with an unpolluted boundary layer as observed in Australia (see green line in Homan et al. (2009), figure 3) than over west Africa.

Carbon monoxide (CO) is produced by incomplete combustion in urban areas and biomass burning injected into the troposphere from the ground. CO is also produced by oxidation of hydrocarbons emitted from the surface. The principal sink of CO is oxidation by OH radical that is formed throughout the troposphere. Because its sources are mainly at the surface and it is destroyed through the troposphere, it is expected to have high value in the boundary layer and to have a decreasing profile in the troposphere. Thus an enhancement of CO at the main convective outflow is considered as a convective signature. Observations from COLD (Cryogenically Operated Laser Diode) instrument (figure 4.5 upper right panel) shows clearly slowly decreasing concentrations up to 350K (200 hPa) and a rapid decrease above. Around 350K enhanced concentrations (measured on the



7 August) is a clear signature of convective transport of CO enriched air from the boundary layer.

This easy picture is complicated by the long lifetime of CO (1-2 months): long range transport of CO enriched air-masses could lead to layers of enhanced mixing ratios that superimpose on convective transport signatures. Barret et al. (2008) studied the long range transport of air masses with high CO concentrations in west African upper troposphere (above 150 hPa) uplifted by convection within the Indian monsoon and then transported over Africa by easterly winds. Sauvage et al. (2007) and Mari et al. (2008) report long range transport of wild fires plumes with elevated CO concentration from central and south Africa in the middle troposphere and Real et al. (2009) demonstrated the biomass burning origin of a polluted layer measured in the west African upper troposphere (200 hPa).

CO<sub>2</sub> is well mixed in troposphere with a minimum during daytime in the boundary layer due to vegetation uptake. Thus the effect of deep convection results in a minimum of CO<sub>2</sub> mixing ratio at the level of main convective outflow. CO<sub>2</sub> profiles measured by the High Altitude Gas Analyzer (HAGAR) are presented in figure 4.5 middle-left panel. Those profiles show distinct minima in the TTL, reflecting the outflow of boundary layer air depleted in CO<sub>2</sub>. These reductions suggest that i) convective influence in the TTL is quite significant in the sampled air masses and that ii) the main convective outflow was usually located at potential temperature levels around 350-360 K (220-140 hPa), and for the flight of 11 August (orange crosses) even reached up to 370 K (115 hPa). In the same figure a bunch of black crosses with mixing ratios well above the mean profile can be seen around 350-370 K (220 - 115 hPa). As well as a CO<sub>2</sub> increase, a large concentration of N<sub>14</sub> (particles larger than 14 $\mu$ m) were measured on the same flight around 200 hPa, as shown in figure 4.5 lower-right panel. These measurements have been performed on the 13 August and, as we will see in chapter 6, they could be explained as a signatures of biomass burning plume transport.

Figure 4.5 upper left panel shows water vapour measurements. It is highly variable up to 370K because of great difference between hydrated air masses out-flowed by deep convective events and background values. Above the highest level reached by deep convection measured during the M55 campaign (370K on 11 August), water vapour concentration are almost constant with height. NO data (lower left panel of figure 4.5) shows clear enhancements below 355K probably due to production by lightening and hence signatures of recent convective processing.

The analyses conducted here is complemented by several works focussing on AMMA observations. Bechara et al. (2009) analysed Volatile Organic Compounds (VOC) measured by the new instrument AMOVOC onboard the two French aircraft (ATR-42 and F-20) aiming to estimate the fraction of boundary layer air contained in deep convective outflow and the vertical transport timescale during convective events

Firstly they distinguish between convective and non-convective air masses using CO, O<sub>3</sub> and relative humidity observations. As previously discussed, CO, O<sub>3</sub> present some characteristics that make them suitable for infer air masses' convective history. For what concern relative humidity, Bechara et al. (2009) report that average condition shows RH values of 70% in lower troposphere (particularly above the tropical forest influenced by the wet monsoon flow). With altitude, air mass layers get dryer up to RH value of 20%. The use of a single tracer is not sufficient for convective case distinction, for example high CO concentrations could be due to transport of biomass burning pollutants. Thus only concomitant variations of tracer vertical shapes are considered by Bechara et al. (2009) as a situation perturbed by convection. Apart from their properties, they choose CO and O<sub>3</sub> because of their high sampling time resolution (1-30 s) and because their atmospheric lifetime is longer than MCS duration (2 months for CO and several days for O<sub>3</sub>) versus MCS life time of 0.5-2 days.

Once filtered out non-convective flight, Bechara et al. (2009) used non methane

hydrocarbons (NMHC) measurements to estimate the fraction of low tropospheric air in fresh convective outflow. Averaging between all the NMCH compound and all the convective flight selected, they found a mean value for this fraction of  $40 \pm 15\%$  (see figure 4.6 Bechara et al. (2009)). Furthermore they estimate a vertical transport timescale during convective events of  $25 \pm 10$  minutes.

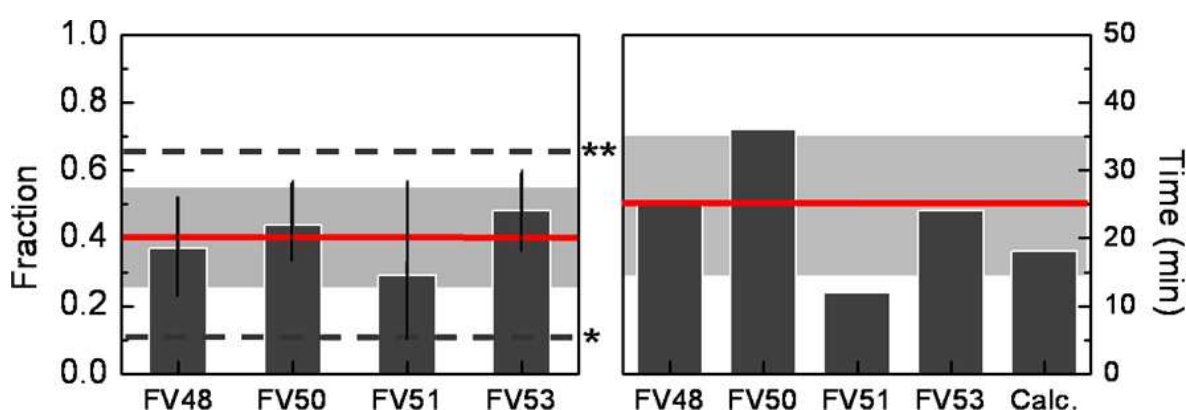


Figure 4.6: Deep convection characteristics in West Africa. Left plot: Fraction of low tropospheric air in fresh convective outflow for each MCS. Vertical lines are error bars, mean fraction is in red, transparent grey area is standard deviation and dashed lines are minimum and maximum literature data comparison. Right plot: Vertical transport timescale for each MCS and theoretical time Calc. calculated considering a vertical speed of  $15\text{ms}^{-1}$  to reach 12 km altitude. Red line indicates mean time, transparent grey area is the standard deviation. (From Bechara et al. (2009))

Superimposed on deep convective transport, long range transport of biomass burning plumes from southern hemisphere has a fundamental role in determining the vertical profile of tracer gases and aerosols in the troposphere and lower stratosphere above west Africa. During northern hemispheric wet season the rainfall band migrate northward and local populations of central and south Africa use fires for agricultural purposes. Many authors studied the direct transport of air masses from wild fires region to west African middle troposphere through the Gulf

of Guinea (see Sauvage et al. (2007); Mari et al. (2008) and references therein). Also upper tropospheric composition can be influenced by inter hemispheric transport of biomass burning plumes as showed by Real et al. (2009).

Thouret et al. (2009) analysed a total of 98 ozone vertical profiles measured over Cotonou, Benin, during a 26 month period (December 2004-January 2007). The 24 vertical profiles recorded in June-July-August (JJA) 2006, during the AMMA-SOP period, are presented in Thouret et al. (2009) and reported here in figure 4.7. Layers with enhanced ozone concentrations are visible (and highlighted by circles) between 3 and 5 km attributed to southern biomass burning products. These southern intrusions were rare in June (only the 30th) and July (2 on 8) whilst they were nearly a daily occurrence during August 2006. Regarding the inter-annual variability Thouret et al. (2009) found that years 2005 and 2006 seem to have had more favourable conditions for intrusions of southern hemispheric biomass burning plumes. Within the MOZAIC (Marenco et al., 1998) data set , 28% of the profiles in JJA 2003 presented such layers while the soundings time series (2005 and 2006) exhibited this phenomenon for 41% of the samples.

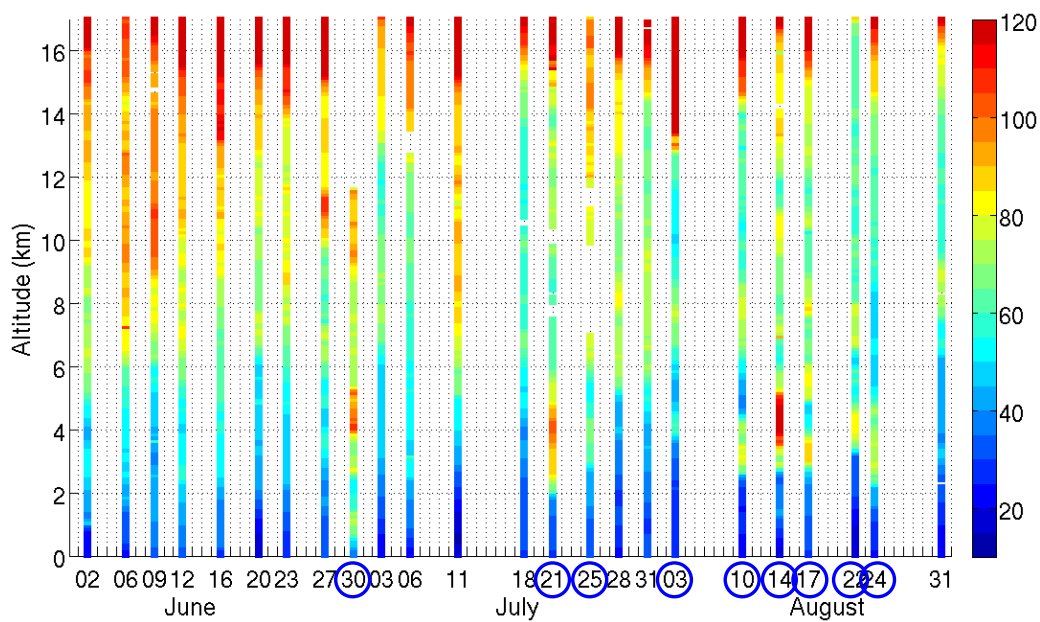


Figure 4.7: Time series of the ozone profiles from the surface up to 17 km during June-July-August 2006. Dates with O<sub>3</sub> enhancement are circled. (From Thouret et al. (2009))

Andrés-Hernández et al. (2009) analysed Peroxy radical measurements made on board the DLR-Falcon research aircraft during AMMA field campaign. They focused on photochemical activity in the outflow of mesoscale convective systems. Hydroperoxyl and alkyl peroxy radicals, are involved in most of the oxidation mechanisms taking place in the troposphere. Knowledge of their amounts and distributions provides essential information about the aging and history of an air mass. Using these measurements they individuate 2 flights (4 and 15 August 2006) with measurements performed within the fresh outflow of MCSs.

Andrés-Hernández et al. (2009) performed simulation with a simplified chemical box model and found  $O_3$  production rates of  $1.0 \text{ ppb h}^{-1}$  for the 15 August flight and between  $0.4$  and  $1.2 \text{ ppb h}^{-1}$  for the 4 August flight. Furthermore they report observation of biomass burning plumes on 4 and 13 August over West Africa in the layer from 500 to 650 hPa. Back-trajectory calculations using the FLEXTRA model (Stohl et al., 1995) indicate the origin of biomass burning plume measured on 4 August in continental Africa while 13 August one originates from Cameroon-Congo, close to the Gulf of Guinea.

Ancellet et al. (2009) used  $CO$ ,  $O_3$ ,  $NO_x$ ,  $H_2O$  and hydroperoxide concentrations measured on board of the French research aircraft F-20 to distinguish between different types of air masses. They identified 5 types of air masses undergone to different transport processes and loaded with different sources of trace gases. To confirm the sources responsible for the chemical characteristics of each group, they determine the transport processes associated to the different air masses using the Lagrangian transport model FLEXTRA.

Regarding the ozone production in air masses away from the direct outflow of MCS, Ancellet et al. (2009) found that it is related to (i) the transport of biomass burning emission from the SH, (ii) local anthropogenic sources like the city plume near Cotonou. Regarding the chemical composition of the outflow of the different MCSs, Ancellet et al. (2009) showed that the increase of  $CO$  and  $H_2O_2$  and the

associated chemical reactivity necessary for subsequent O<sub>3</sub> formation, are directly related to the position and the lifetime of the MCS during its evolution. Increased lifetime (>1.5 days) allows more H<sub>2</sub>O<sub>2</sub> formation, while a trajectory of the MCS crossing the 10N latitude increases the CO transport to the upper troposphere.

## 4.3 Convective outflow measurements

Here the analysis is restricted to M55 flights potentially influenced by local convection (7, 8 and 11 August 2006). Data collected on these specific flights is used to examine signatures of local deep convection on the measured trace gases and aerosols. Satellite observations will be used to analyse the convective activity during the 24 hour before the flights took place and to hypothesise which are, among various candidates, the MCS outflow that influenced the aircraft measurements.

### 4.3.1 Satellite observations

CTBT at  $10.8 \mu\text{m}$  measured by the Meteosat second generation satellite provides information about MCSs lifetimes and positions. Figure 4.8 shows the evolution of MCSs before each M55 flight. A temperature threshold ( $\text{CTBT} < 210 \text{ K}$ ) was applied to select deep convective clouds (Schmetz et al., 1997). CTBT evolution during 24 hours before the observations are reported with time resolution of 6 hours and horizontal resolution of 4 km together with the M55 flight path.

**August 7 2006** The top panel in Figure 4.8 shows the MSG CTBT evolution from August 6 at 15 UTC to August 7 at the same time. Four MCSs, identified as organized convection, are visible during this period: (1) a first one propagating north of the measurement area; (2,3) two systems crossing and merging above south-west Chad; and a last one (4) in Sudan. Furthermore, sparse convection (5) develops at the boundary between Niger and Nigeria from 24 to 12 hours before the observations. Assuming an average wind speed of 19 m/s derived from ECMWF analyses, it is possible to argue that the region where the M55 flew could have been influenced both by the simultaneous local convection (1) and by sparse convection (5) that occurred between 12 and 24 hours before the flight above Niger.



**August 8 2006** The CTBTs prior to 8th August flight are shown in middle panel of Figure 4.8. Two MCSs formed between August 7 and August 8, one dissolving between Sudan and Chad 12 hours before measurements (1) and the second (2) dissolving over South Niger 10 hours before the measurement. In that case, the mean zonal wind speed from ECMWF is 16 m/s, and it is possible to argue that the outflow of system (2) could have reached the M55 area at the time of the measurement. Furthermore, less organized convection forms at the same time of M55 observations on both the east and west sides of the flight path.

**August 11 2006** The CTBTs before the 11th August flight are shown in bottom panel of Figure 4.8. Two vast MCSs are observed: a westward moving one (1) crossing the measurements area 6 hours before the flight, and an eastward one (2) dissolving over eastern Nigeria, 9 hours before measurements. Using a mean zonal wind speed of 13 m/s, it is possible to argue that M55 likely sampled the outflow of system (1).

### 4.3.2 M55 observations

In this section observations of aerosol backscatter ratio (BSR), aerosol depolarization (D), ozone ( $O_3$ ), water vapour ( $H_2O$ ), carbon dioxide ( $CO_2$ ) and particles fine fraction ( $N_{6-14}$ ) are used. Relative humidity with respect to ice freezing (RHI) is estimated from observed  $H_2O$ , temperature and pressure using the formula prescribed by the World Meteorological Organization and the Marti and Mauersberger (1993) formula for saturation pressure over ice. The description of the campaign and the overview of each flight is provided in Cairo et al. (2009) where a list of available observations are presented.

Enhanced values of BSR indicate the presence of aerosols and values of D above 10 % indicate the presence of ice crystals (Cairo et al., 1999). The mechanism of cirrus formation in the uppermost troposphere is still matter of debate, in

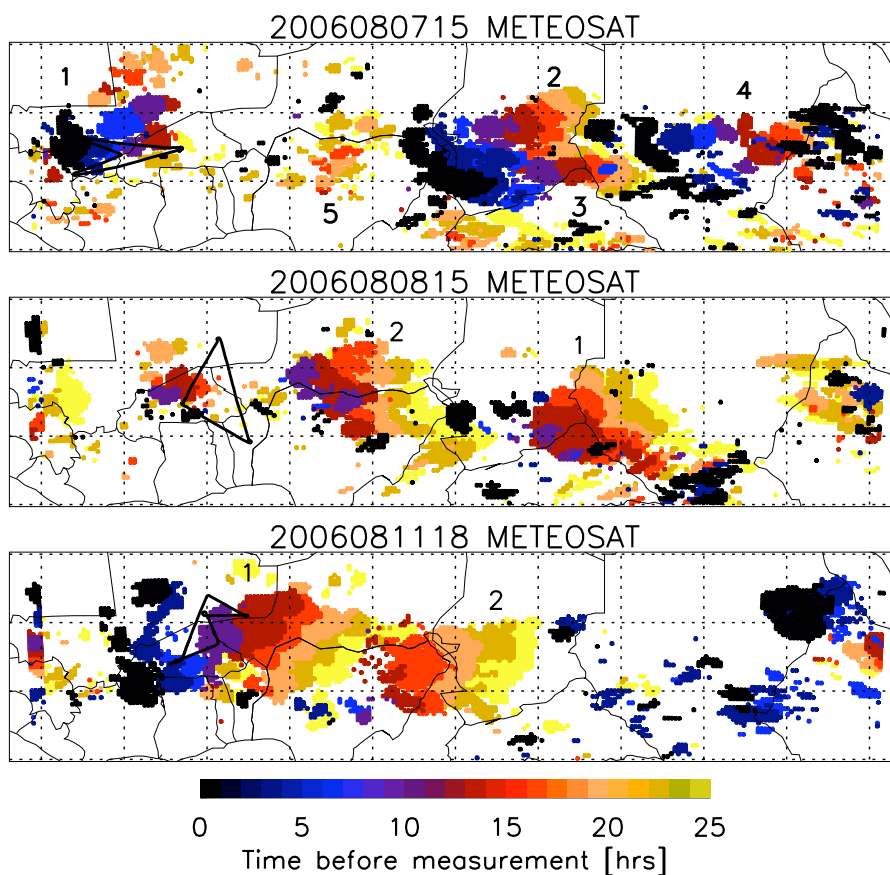


Figure 4.8: Meteosat Cloud top brightness temperature time evolution during 24 hours prior to the M55 flight on August 7 2006 (top panel), August 8 2006 (middle level), and August 11 2006 (lower panel). Clouds are shown as colored regions where  $CTBT < 210$  K. Colors indicates the time (in hours) prior to observations. Flight path is shown by the black line; numbers identify different MSCs described in the text.

particular whether ice particles formation can be directly linked to deep convective systems (see for instance Pfister et al. (2001)). The use of ice particles as tracer for convection may be ambiguous.

Ultrafine particles ( $N_{6-14}$ ) are estimated as the difference between the concentration of particles larger than 6 nm and larger than 14 nm; enhanced values of  $N_{6-14}$  (up to  $1000 \text{ cm}^{-3}$ ) indicate that formation must be recent because nucleation mode particles exist only for few hours to one day. Such values can be observed in recent outflow of deep convective clouds (Curtius, 2006). Non convective average profile, used to identify observed outliers, was calculated from data collected on the 4 and 13 August flights. These flights were large-scale north-south transects and provide information on the background conditions in the uppermost troposphere.

Figure 4.9 shows the M55 observations on August 7, there and in the following figures 4.10 and 4.11 dashed lines represent non-convective average profile. The flight was carried out between 11N and 13N and sampled a region east of the MCSs indicated by (1) in the upper panel of figure 4.8. Two layers of enhanced aerosol depolarization were observed at 350 and 370 K. Observations with enhanced aerosol concentrations ( $\text{BSR} > 1.2$ ) are labeled with open triangles. It can be seen that particles are in solid phase since  $D$  is larger than 20 % when BSR is enhanced.

Total water is enhanced with respect to the average profile in both aerosol layers where RHI exceeds 100 %.  $\text{O}_3$  concentrations range between 45 and 60 ppbv at 350 K (where BSR is enhanced) and increases steadily above 360 K.  $N_{6-14}$  shows enhanced values (above  $100 \text{ cm}^{-3}$ ) in the lower aerosol layer. In the higher layer, enhanced BSR were observed together with  $\text{O}_3$  concentrations of 80 ppbv which is above the values measured below 360 K.  $\text{CO}_2$  data were not available for this event.

Figure 4.10 shows the observations for August 8; the M55 performed a north-south cross section between 8N and 18N (see Figure 4.8, middle panel), and

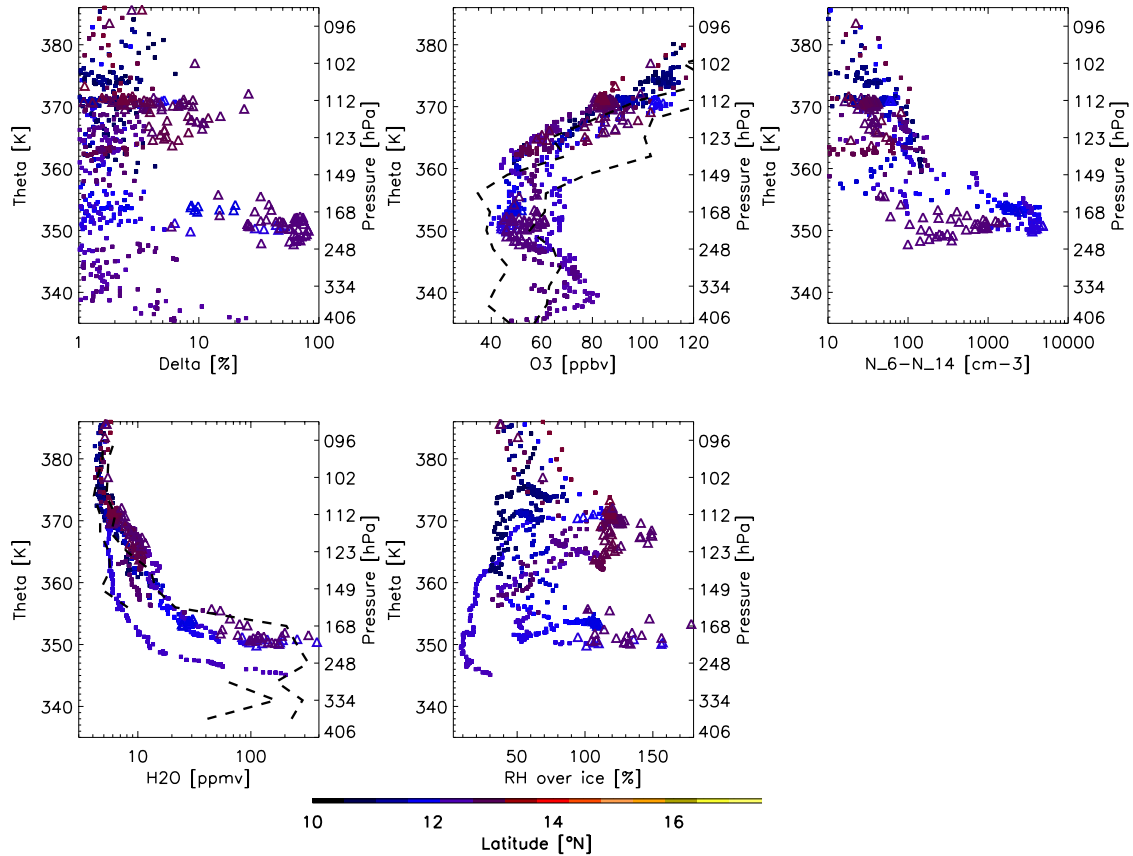


Figure 4.9: Vertical profiles of observed depolarization  $D$ , ozone  $O_3$ , carbon dioxide  $CO_2$ , particle fine fraction  $N_6-N_{14}$ , water vapour  $H_2O$  and relative humidity with respect to ice  $RH$  on August 7, 2006. Colors indicate the measurement latitude; triangles indicate the observations within air parcels containing aerosol ( $BSR > 1.2$ ). Dashed lines indicates average value  $\pm$  one standard deviation of  $O_3$ ,  $CO_2$  and  $H_2O$ .

measurements are likely to have been influenced by MCS outflow 10 to 20 hours prior to observation. Enhanced BSR and D were observed between 11N and 14N below 355 K, at 17N at 365 K and at lower latitudes (11N) between 370 and 375 K. In the lower layer, H<sub>2</sub>O concentrations are much larger (15 to 200 ppmv) at 14N with respect to 11N. Values of RHI are above 100 % inside the three aerosol layers.

O<sub>3</sub> shows again a constant profile below 360 K with concentrations ranging between 40 and 70 ppbv in correspondance to the enhanced BSR (triangles). Higher concentrations of ozone are seen above. CO<sub>2</sub> concentrations are quite variable below 350 K (larger values at 11N than at 14N) and steadily increase above. Slightly reduced CO<sub>2</sub> concentrations were observed between 365 and 375 K. This could be interpreted as a signature of convective outflow that transport depleted CO<sub>2</sub> from below since convection uplifts air poor in CO<sub>2</sub> originating from the surface (Park et al. (2007)).

The aerosol layer at 365 K is also associated with enhanced H<sub>2</sub>O (15 ppmv) and saturated RHI. No clear signature on CO<sub>2</sub>, CO and O<sub>3</sub> is visible. The highest layer at 372 K is associated with enhanced H<sub>2</sub>O and RHI > 100 % while CO<sub>2</sub> do not show any deviation with respect to the average profile. N<sub>6-14</sub> cannot be estimated since observations have a partial coverage. However the analysis of total number of particles available above 360 K height do not show any increase in concentration due to nucleation event.

Figure 4.11 shows the observations for 11 August, taken between 12N and 16N (see figure 4.8, bottom panel). Several layers with enhanced BSR and D are observed up to 376 K. H<sub>2</sub>O is enhanced in the 355-365 K layer at 18N of latitude where no particles were observed while RHI were unsaturated. Increased H<sub>2</sub>O was also observed between 365 and 380 K at 14N of latitude at the same time as enhanced ice particles.

N<sub>6-14</sub> is higher (with values between 100 and 3000 cm<sup>-3</sup>) up to 370 K and

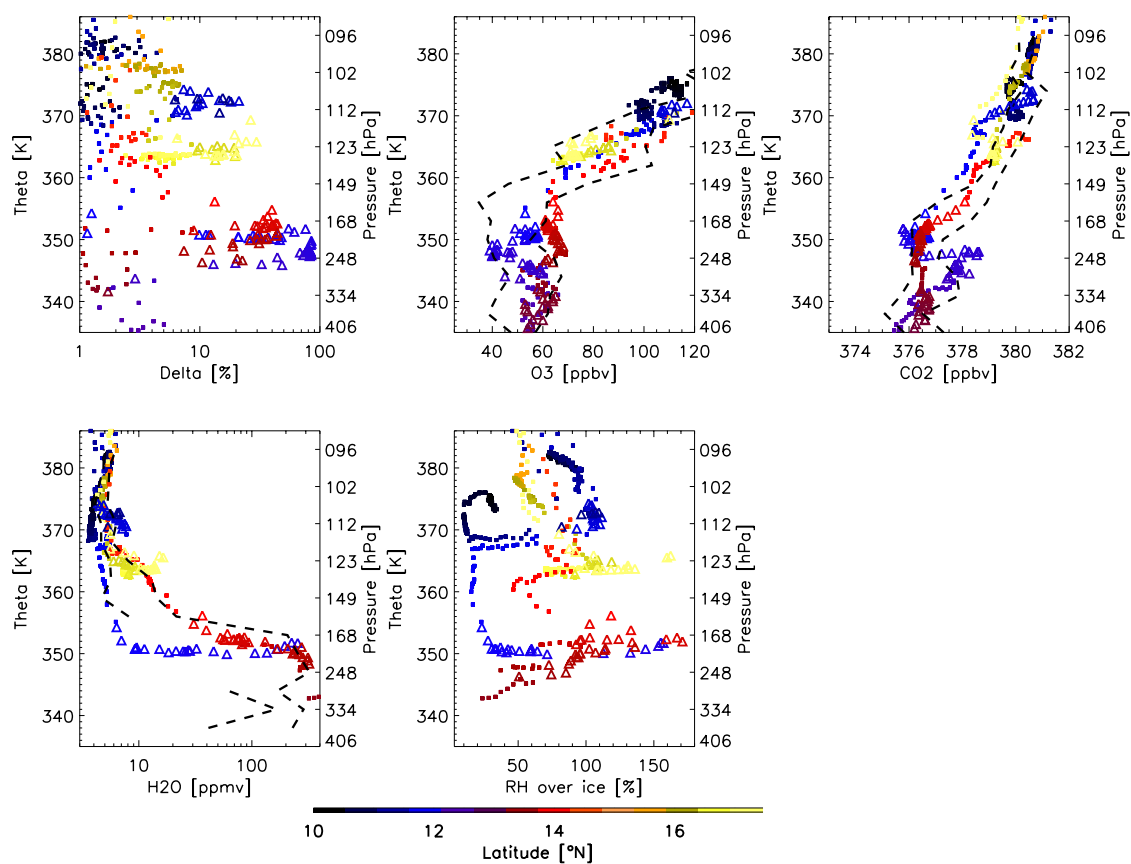


Figure 4.10: As Figure 4.9 but for August 8, 2006

larger values are observed with background BSR. Moreover, large  $N_{6-14}$  is in general correlated to depleted  $CO_2$ .  $O_3$  concentrations range between 45 and 60 ppbv below 355 K. Between 355 and 370 K  $O_3$  is highly variable (45 to 90 ppbv) depending on the sampled latitude and increases steadily above that level.  $CO_2$  shows constant concentrations below 355 K (377 ppbv) and reduced concentrations (374 ppbv) from 355 to 368 K.

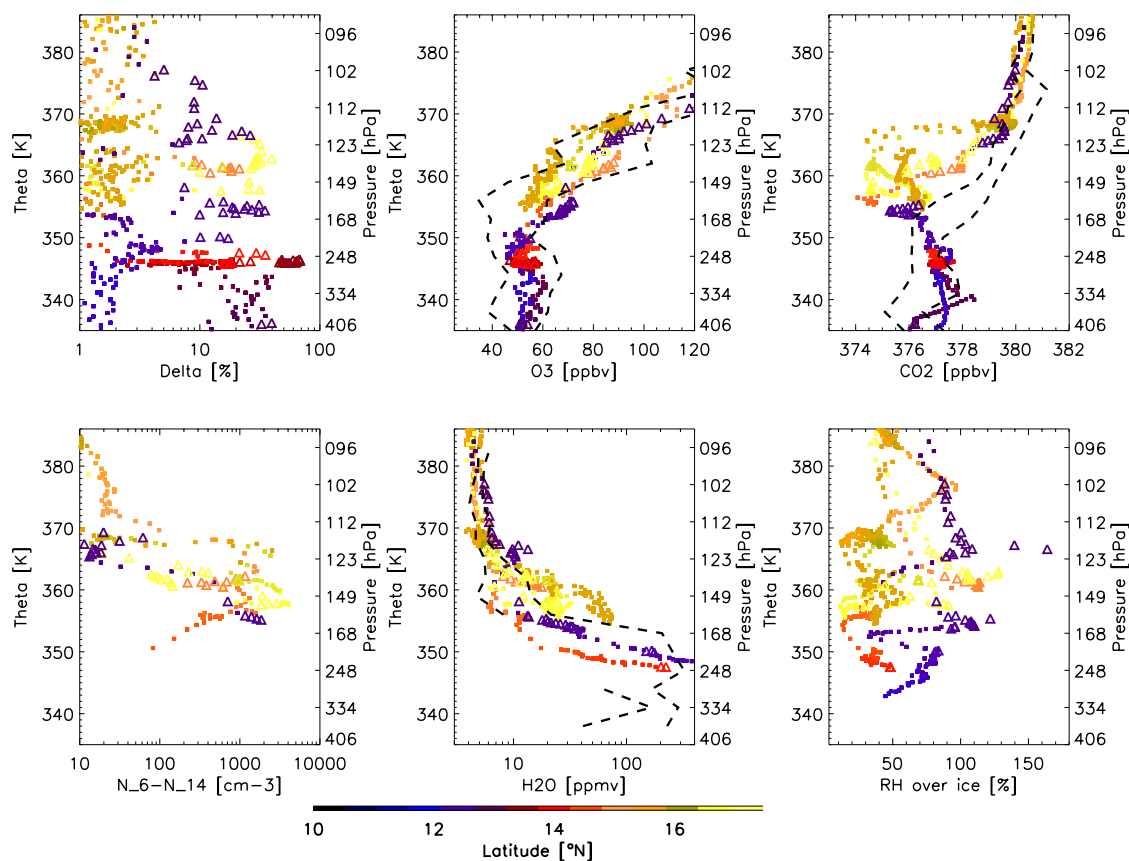


Figure 4.11: As figure 4.9 but for August 11, 2006

From the data collected during the flight considered influenced by recent (less than 4 days) convection (namely 7,8 and 11 August), it is evident that convective impact is visible below 355 K with simultaneous enhancements in water vapour,

BSR and aerosol fine fraction, together with reduced concentrations of  $\text{CO}_2$  and nearly-constant  $\text{O}_3$ . Enhanced concentration of ice particles were also observed up to these altitudes indicating that in the main outflow they were formed as a result of deep convection.

Above 355 K several layers of particles under saturated conditions were observed. During August 7 and 8 these layers were less ubiquitous with respect to the main outflow below 355 K and were, on average, not correlated to a clear signature on chemical tracers. Nevertheless, small and sporadic signatures in  $\text{CO}_2$  (and  $\text{NO}$  - not reported here) were observed above the main convective outflow level.

Observations on 11 August show a different picture with ice aerosol observed throughout the vertical profile up to 375 K. In this case, convective impact reached up to 365 and 370 K based on the presence of reduced  $\text{CO}_2$  concentrations and the presence of ultrafine particles.

The identification of convective signatures in  $\text{O}_3$  is less straightforward due to high ozone variability in West Africa troposphere. Local sources of  $\text{O}_3$  over West Africa which can be convectively uplifted are mixed with air masses advected from upwind regions and air from the lower stratosphere in the upper TTL. Observations of ice particles and outliers in chemical species (and ultrafine particles) are often uncorrelated in the layer between the average convective outflow at 355 K and the tropopause, leading to the qualitative conclusion that this region is composed of airmasses with different processing and lifetime in the TTL.



## Chapter 5

# Impact of deep convection in the tropical tropopause layer in West Africa

In section 3.6 we showed that the assimilation of CTBT into the BOLAM model improves the positioning of deep convection and coherently modifies model dynamics, generating divergent wind fields above the top of MCSs and convergent winds in the boundary layer. This makes simulation performed with BOLAM nudged with CTBT a suitable instrument to study the vertical transport due to deep convection. Thus, we investigate the role of convective uplift on trace gas and aerosol concentrations over West Africa during August 2006, with the aid of trajectories calculated from the mesoscale model BOLAM. The analysis is carried out using M55 Geophysica measurements collected during the flights influenced by recent convection on 7,8 and 11 August 2006 that have been presented in section 4.3.

Moreover, the mesoscale simulations are used to estimate the variability in convective outflow through the use of the in-situ observations coupled to the trajectory analysis. In order: (1) to evaluate the capability of the model

to reproduce the vertical structure of convective outflow and the presence of convectively processed layers above the level of average convective outflow and, (2) to identify the extent of such layers and compare with the observed impact of convection in the upper troposphere.

## 5.1 Mesoscale simulation

The BOLAM model (described in section 3.2) is been used to simulate the impact of convection upper tropospheric air masses. The horizontal domain chosed has 235 x 235 grid points and 24 km horizontal resolution. Here, the simulation started at 00 UTC on 4 August to 00 UTC on 14 August 2006, to cover all the local flights performed by the M55 Geophysica. The model was continuously nudged with brightness temperatures at  $10.8 \mu\text{m}$  from Meteosat Second Generation (MSG) satellite in order to accurately reproduce the evolution of mesoscale convective systems as already described in chapter 3.

### 5.1.1 Validation

The nudged BOLAM simulation was evaluated by comparing model derived CTBT and the satellite observations shown in Figure 4.8. Figure 5.1 shows CTBT calculated using BOLAM water vapour, temperature and hydrometeors profiles. Similarly to figure 4.8, only regions with CTBT  $< 210$  K are plotted.

BOLAM CTBTs for August 7 (shown in top panel of figure 5.1) correctly reproduce the observed evolution of MCSs labeled as 1 to 4 in figure 4.8, top panel, and also the sparse deep convection upwind of measurement area which developed 12 and 24 hours before the flight took place. On the 8 August, BOLAM CTBTs (middle panel of figure 5.1) show the MCS (labeled as 1 in Figure 4.8) dissolving over Niger, while MCS (2) is more scattered, particularly at the end of its life cycle, 15 to 9 hours before the measurements. Furthermore, sparse and

intense convection developing upwind of the flight area 20 hours before the flight is also captured by BOLAM. Bottom panel of figure 5.1 shows CTBT on August 11. Both the position and life cycle of two MCSs are well reproduced by the model even if they appear more scattered.

The nudging procedure improves the representation of convection compared with the simulation without nudging (not shown). In general, BOLAM generates less organized convective systems with respect to satellite observations but the position and the temporal evolution of MCSs are well reproduced. Simulations also show a coherent transport behavior in presence of MCSs generated by nudging, with increased divergence in the upper troposphere (see section 3.6). Therefore, the transport by convective uplift and outflow can be estimated from the BOLAM simulation with an accuracy considered adequate enough to be used in the interpretation of the M55 data.

### 5.1.2 Trajectories

In order to account for convective uplift, trajectories were calculated from BOLAM using the on-line approach proposed by Gheusi and Stein (2002). The method is based on the advection of air parcels positions treated as a passive tracer and the subsequent off-line reconstruction of backward trajectories from position fields. In addition to the three-dimensional transport calculated using explicitly resolved winds, the position fields are also modified by the parametrized vertical diffusion and the convective transport that uses a mass-flux method to re-adjust the vertical displacements inside convective clouds.

Despite the uncertainties related to this approach, Gheusi and Stein (2002) have demonstrated that the Lagrangian evolution can be studied on a qualitative basis for relatively large trajectory clusters. In the present study, this method was used off-line with a time interval of 3 hours to calculate the trajectories. Fierli et al. (2008) have previously shown that BOLAM trajectories provide a realistic

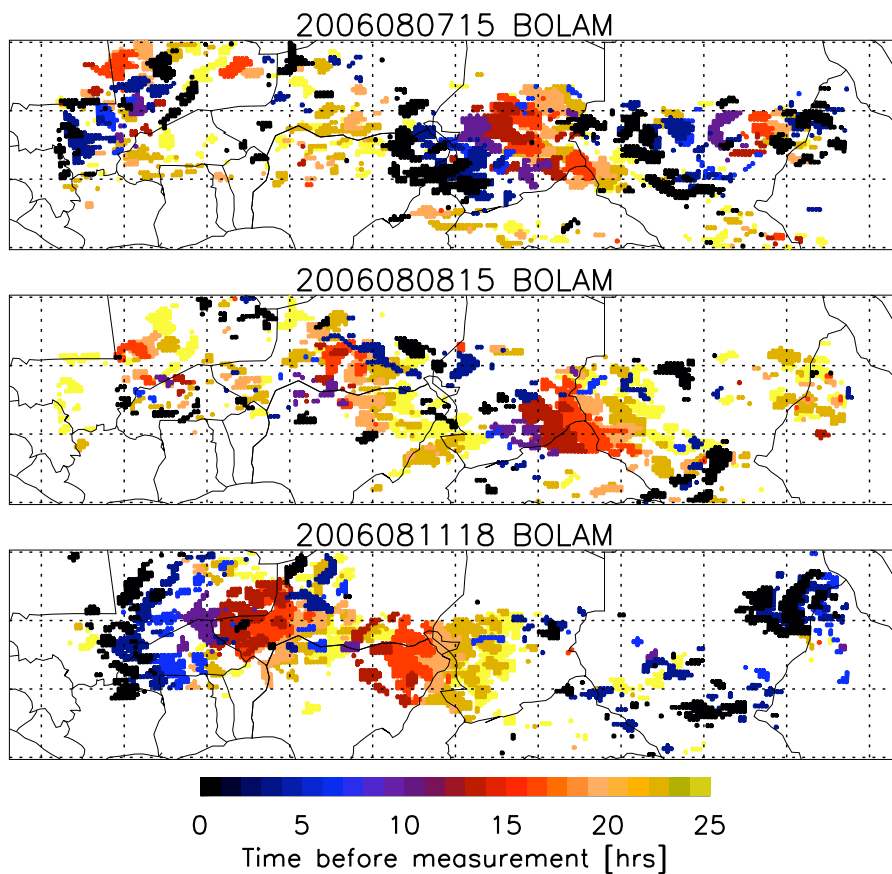


Figure 5.1: BOLAM cloud top brightness temperature time evolution during 24 hours prior to the M55 flight on August 7 2006 (top panel), August 8 2006 (middle level), and August 11 2006 (lower panel). Clouds are shown as colored regions where CTBT < 210 K. Colors indicates the time (in hours) prior to observations.

description of the outflow originating from a vast convective region during the HIBISCUS (Impact of tropical convection on the upper troposphere and lower stratosphere at global scale) campaign over Brazil. Although the model vertical resolution is still fairly coarse, mesoscale model simulations are likely to resolve convective transport at altitudes ranging from the top of the mean convection outflow and the tropopause.

Two trajectory clusters were calculated for each flight. (1) Backtrajectories originating from model grid points within a region encompassing the flight path with pressure levels ranging from 300 to 100 hPa in order to include the whole upper troposphere. The overall number of trajectories varied from 6900 for 7 August 12 UTC to 10800 for 8 and 11 August. (2) Backtrajectories originating from the flight path calculated from each observation point every 5 minutes, leading to an average cluster of 1000 elements per each M55 flight. The results are used to identify which convective systems have generated the outflow observed by M55, and the extent to which convection might have influenced the region where observations were carried out.

Based on this Lagrangian analysis, 2 different diagnostics were computed:

- The convective fraction,  $f_c$ , (calculated from cluster (2) in 12  $\theta$  layers) defined as the ratio between the number of parcels having been processed by convective uplift and the total number of trajectories. This is analogous to the model estimate of the probability that an air mass sampled by the aircraft was processed and uplifted by deep convection within a  $\theta$  layer. In order to characterize the uplift, trajectories originating below 500 hPa, and uplifted with a vertical speed larger than 50 hPa/h and crossing irreversibly 250 hPa level, were selected
- The convective age,  $t_c$ , is the time elapsed between convective uplift and observation.  $t_c$  is defined for each parcel of cluster (1,2) as the earliest time

when air masses uplifted by deep convection (using the same criteria as  $f_c$ ) irreversibly crossed the 250 hPa level.

$f_c$  can be compared to similar diagnostics used to evaluate convective transport from other modeling studies such as Mullendore et al. (2005)) and analysis in-situ observations (Bertram et al., 2007).

Since modeled and observed ice particle presence can also provide useful information, two additional diagnostics were defined to estimate model ice clouds and the extent to which such clouds might have been influenced by deep convection.

- The ice fraction,  $f^{ice}$ , is the fraction of points from cluster (2) with values of  $RHI^{ice} > 100\%$  at the final point along the flight
- The convective fraction of ice,  $f_c^{ice}$ , is the fraction of air masses uplifted by deep convection (calculated from cluster (2) using the same criteria as  $f_c$ ) with values of  $RHI^{ice} > 100\%$  at the final point along the flight

## 5.2 Convective outflow from BOLAM trajectories

Figure 5.2 shows  $t_c$  estimated from backtrajectory cluster (1) initialized on 7 August 12UTC for two  $\theta$  layers (369 K and 353 K). The geographical points where backtrajectories irreversibly cross the 250 hPa level are reported in the lower panel of Figure 5.2 where  $t_c$  values are indicated by the colors.

The number of trajectories uplifted by convection increases with decreasing altitude and the region sampled by the aircraft is marginally influenced by convection in the higher  $\theta$  layer. The uplift occurred 48 to 50 hours before the flight. Air masses from the lower troposphere crosses the 250 hPa level 20 to 50 hours prior to the measurement; this is visible in figure 5.2 (lower panel), where it is shown that air masses irreversibly crossed 250 hPa near to deep convective systems above southern Niger and northern Nigeria.

It is important to note that BOLAM does not show air masses with low  $t_c$  uplifted in the western part of the domain in correspondance to the MCS closest to the flight (MCS (1) in figure 4.8, top panel).

It is difficult to assess if this can be attributed to the fact that outflow of MCS system (1) is not advected into the flight region or to the fact that BOLAM fails to reproduce the intensity and extent of this MCS system as mentioned in section 5.1.1. BOLAM also shows the presence of saturated air ( $RH_{ice} > 100\%$ ) in the lower layer (yellow shaded area) corresponding to main outflow altitudes.

Figure 5.3 shows the same set of diagnostics for 8 August. Although a similar picture to the previous event can be inferred, the number of trajectories uplifted by deep convection is larger during this event. Moreover, the fraction of air masses characterized by lower  $t_c$  (16-24 hours) is larger in the lower  $\theta$  layer. Saturated air (yellow shade) is large and is present also in the upper layer but is located close to the outflow in the lower layer only.

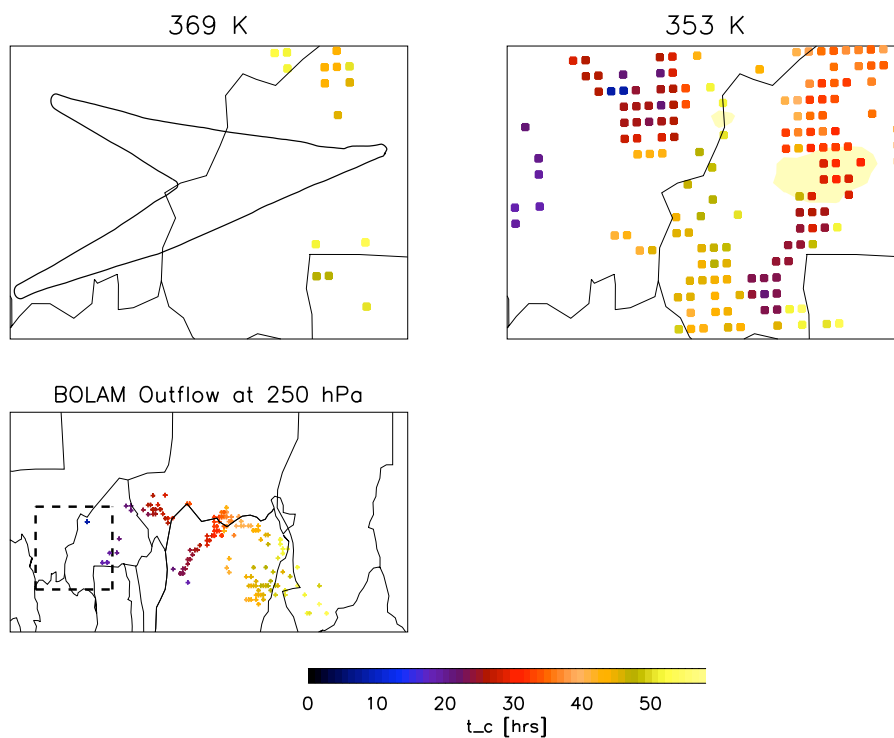


Figure 5.2: Upper panels: maps of  $t_c$  estimated from the BOLAM trajectories (see text for definition) for two theta layers (368-369 K above the main convective levels and at 353-355 K) for 7 August 2006. Yellow shaded area indicates where BOLAM  $RH_{ice}$  exceeds 100 %. The flight path is also reported in the top left panel. Lower panels: the position where air parcels cross irreversibly the 250 hPa surface. Dashed box indicate the horizontal domain shown above where trajectories in cluster 1 (see text) originates. Colors indicate  $t_c$ .



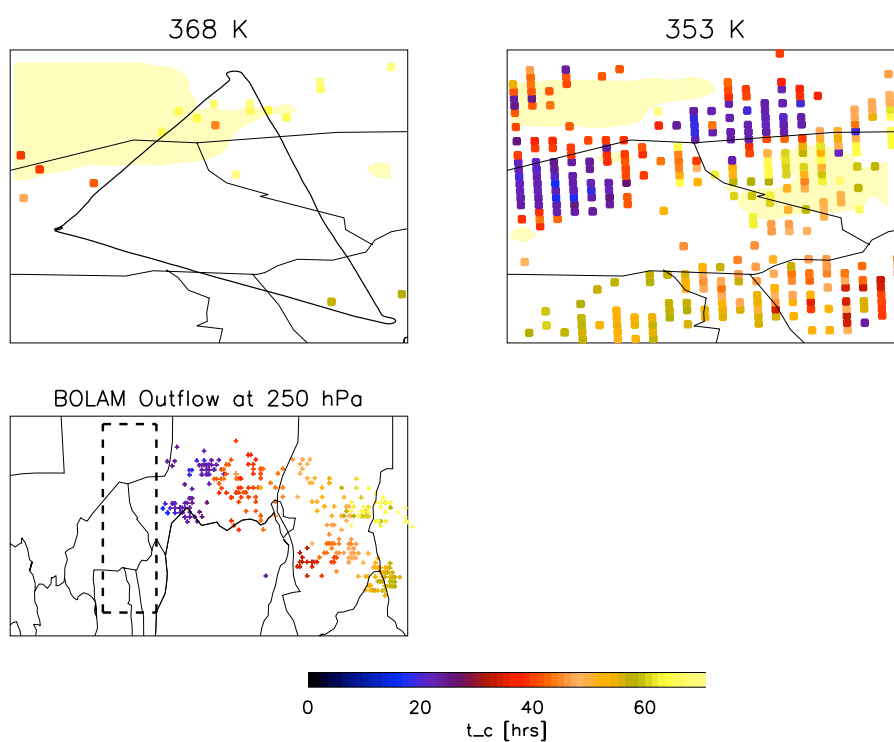


Figure 5.3: As figure 5.2 but for the 8 August 2006 flight

The results for 11 August (figure 5.4) show much larger convective impact in both 354 and 367 K layers mostly related to uplift occurring in the large MCS labeled by (1) in figure 4.8 that is correctly reproduced by BOLAM (figure 5.1, lower panel).  $t_c$  ranges between 12 and 24 hours at 354 K and has significantly higher values at 367 K, with a non-negligible number of trajectories with  $t_c$  ranging between 30 and 80 hours. Both layers are characterized by large areas of saturated air.

The aerosol backscatter data from the Cloud-Aerosol Lidar and Infrared Pathfinder Satellite Observation (CALIPSO) that sampled the region where outflow occurred at longitude ranging between 3E and 5E on 11 August at 1h30 UTC (dashed line in figure 5.4, lower panel) are shown in figure 5.5. It shows a deck of solid particles up to 17 km (380 K) between 7N and 18N and vast deep convection area reaching up to 16 km (370 K) around 15N. BOLAM trajectories give a coherent picture with regard to the convective ascent at the same time as the CALIPSO overpass and the presence of ice clouds in the outflow region between 15 km and the tropopause (located at 17 km) in the model results.

Overall, the analysis of cluster (1) shows that modeled convection has an important impact on the 353-355 K layer. At 363-366 K, convective transport influence is visible to a small extent on 7 and 8 August while the impact is much larger on 11 August. Moreover, the convective age (as given by  $t_c$  values) is variable showing that air masses influenced by very recent convection ( $t_c < 24$  hours) coexist (especially at higher altitudes) with air masses influenced by older convection ( $t_c > 48$  hours) which formed to the east over central Sahelian region above northern Nigeria and southern Chad.

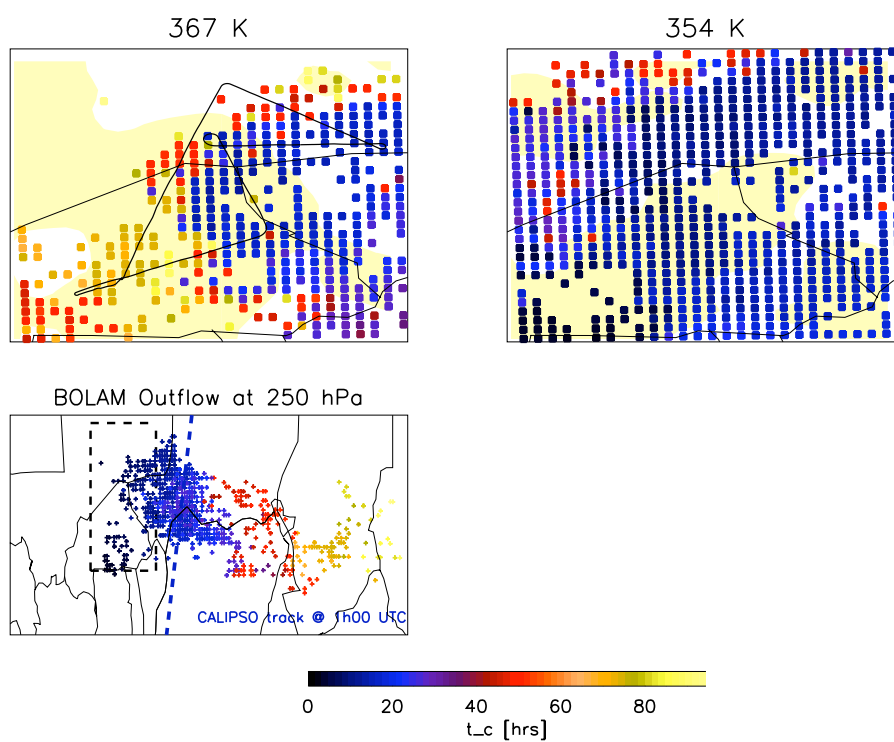


Figure 5.4: As figure 5.2 but for the 11 August 2006 flight. Dashed line indicates CALIPSO overpass and blue color follows the  $t_c$  scale (15 hours before the measurement)

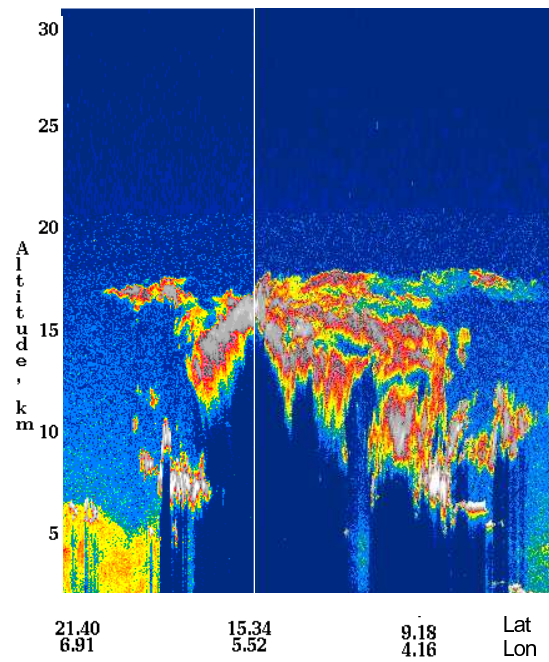


Figure 5.5: CALIPSO aerosol backscatter observed on August 11 1h30 UTC. Aerosol observations (not shown) shows that aerosol are in solid phase.

### 5.3 Comparison with observations

We focus now on the vertical structure of convective outflow in the upper troposphere. In order to perform a comparison of the modeled and the observed vertical profiles, a set of diagnostics analogous to those described in section 5.1.2 are applied to measurements: (1)  $f_{BSR}$  is the fraction of observations with  $BSR > 1.2$  and describes the vertical distribution of ice clouds to be compared with  $f_{ice}$ ; (2)  $f_{CO_2}$  is the fraction of observations with  $CO_2$  concentrations lower than the average value minus its standard deviation and describes the possible impact of deep convection on  $CO_2$  profiles.  $f_{BSR}$  and  $f_{CO_2}$  were averaged over the same 12  $\theta$ -levels used for the model-based diagnostics discussed in the previous section. Vertical profiles of diagnostics are plotted in figure 5.6: model derived ones are colored in blue and observation-derived in red.

The vertical profile of  $f_{BSR}$  for 7 August flight (figure 5.6, upper panel, red dotted line) shows the presence of two distinct layers (below 360 K and at 367 K) as shown in figure 4.9. The model-derived vertical profiles of  $f_{ice}$  (left panel, solid blue line) and  $f_{ice}^c$  (left panel, dashed blue line) indicate that BOLAM predicts the presence of ice clouds in the lower layer that are formed inside air masses uplifted by deep convection. The BOLAM convective fraction,  $f_c$  (solid blue line on the right panel), decreases with height and is in acceptable agreement with  $f_{BSR}$  below 355 K (reported also in the right panels). Conversely, in the uppermost layer, where enhanced depolarization was observed, BOLAM does not reproduce ice clouds and reports a small (less than 3%) and old (up to 60 hours) convective uplift. As discussed earlier, this could be due to the fact that BOLAM fails to fully reproduce the dynamics of the closest MCS to the flight for this event.

On 8 August (middle panel) the vertical structure of  $f_{BSR}$  is similar to the previous day but, in this case, BOLAM shows a better agreement throughout the entire vertical profile; enhanced  $f_{ice}$  is simulated in correspondance to ice particle observations in the upper layer.  $f_{ice}^c$  is equal to  $f_{ice}$  below 355 K indicating that

modelled ice clouds were formed in the convective outflow whilst above 355 K, the BOLAM model simulated ice particles in upper tropospheric air masses. Above 360 K  $t_c$  is characterized by values (48 hours) larger than in the main outflow. In the same layer low  $\text{CO}_2$  (shown in figure 4.10) was also observed and  $f_{\text{CO}_2}$  (red dashed line on the right panel) reaches 5%.

On 11 August (lower panel) the model shows two main ice cloud layers (below 360 K and at 370K) in agreement with the observations which show distinct thin layers of ice particles. The trajectories overestimate  $f_{ice}$  with respect to  $f_{BSR}$ . 75% of model ice clouds are of recent convective origin in the lower layer (estimated as the ratio between  $f_{ice}^c$  and  $f_{ice}$  throughout the vertical range) whilst the fraction is around 30% in the upper layer.  $f_c$  shows a large convective fraction (up to 90 %) which decreases with altitude. Air masses with higher  $t_c$  (72 to 90 hours) are visible together with air masses originating from recent outflow ( $t_c$  less than 20 hours) between 360 and 375 K. Within the same layer,  $f_{\text{CO}_2}$  is large (up to 90 %) and corresponds to regions where low  $\text{CO}_2$  was observed (see figure 4.10) .

The trajectory analysis shows that local convection hydrates the upper troposphere over West Africa and in one case (11 August) there is a significant impact up to 375 K. This recent convection is superimposed on older convection which took place up to 4 days before the observations. Even if a detailed analysis of cirrus formation mechanism is outside the scope of this chapter, it is worth to noting that modelled and observed layers of ice particles are in good agreement, despite the fact that for the 11 August, the model overestimates the amount of ice clouds.

The analysis shows that ice particles are formed directly in the main outflow below 360 K and their presence is correlated to the uplift seen by model. Above the main outflow, trajectories indicates that ice clouds often form in the TTL at the top of mesoscale convective systems . These results are in qualitative agreement with a recent analysis of CALIPSO and CLOUDSAT observations which concluded

that TTL cirrus are likely observed close to deep convective clouds (Sassen et al., 2009).

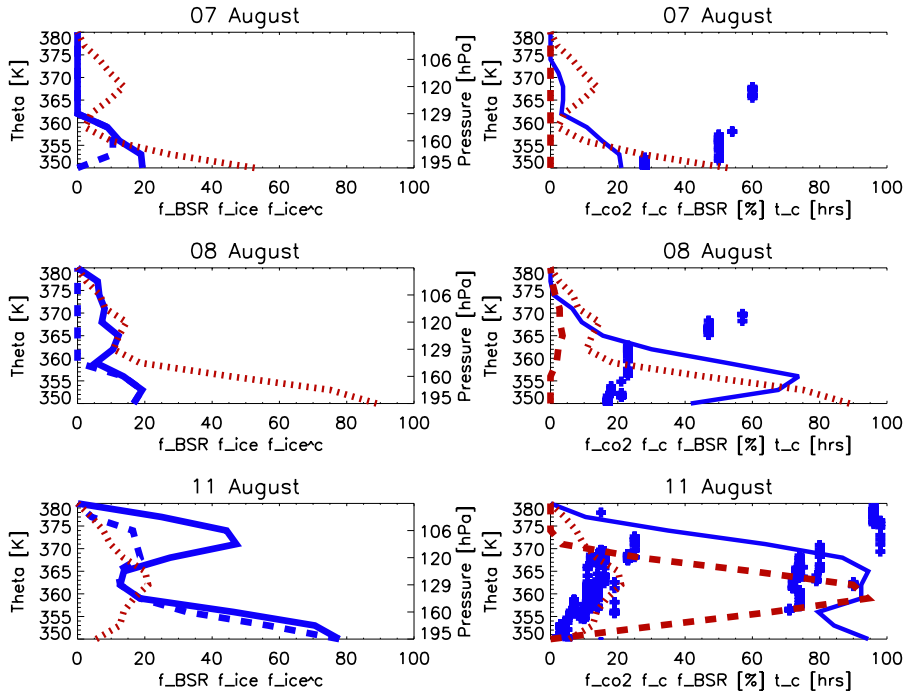


Figure 5.6: Vertical profiles of the diagnostics described in the text. Model-derived ones are plotted in blue, observation-derived in red. Left column: BOLAM ice fraction  $f_{ice}$  (solid blue line) and convective ice fraction  $f_{ice}^c$  (dashed blue line); observed aerosol fraction  $f_{BSR}$  (dotted red line), Right column: BOLAM convective time  $t_c$  (blue symbols), convective fraction  $f_c$  (blue line); observed fraction of outliers in  $CO_2$   $f_{CO_2}$  plotted as dashed red line;  $f_{BSR}$  is also plotted to be compared with  $f_c$ . Top panels are for August 7 middle for August 8 and bottom for August 11.

In summary, the improvements achieved with the nudging scheme shown in chapter 3, are used in this chapter to simulate tracer transport by deep convection.

Beside the melioration of precipitation, an improvement of organised convection position and evolution as well as the coherent modification of the divergent wind at convection outflow level, is necessary for a correct description of the effect of deep convection over trace gases transport. Thus we ran a simulation with BOLAM, improved by the nudging scheme, over the period 4-14 August 2006 to help the analysis of the measurements taken by the high altitude research aircraft M55 in the frame of the AMMA-SCOUT campaign.

The comparison between CTBT from Meteosat and from the BOLAM model showed that nudged mesoscale simulation correctly reproduce the general pattern and the propagation of convection observed during the first 15 days of August 2006 and therefore can be used to estimate the convective outflow and to compare with M55 measurements.

BOLAM shows good agreement with convective perturbation derived from observations of aerosol and chemical tracers for the main convective outflow region below 355 K and indicates that West Africa convection influences up to 50 % of airmasses resulting in substantial hydration and formation of ice particles up to this level. This result is in accord with the study of Bechara et al. (2009) which analysed convective flights performed by the two research aircraft ATR-42 and Falcon-20 during the AMMA campaign in August 2006. They report for the fraction of low tropospheric air in fresh convective outflow a mean value of  $40 \pm 15$  %. BOLAM also correctly reproduces the outflow of a recent MSC on 11 August and simulates a large convective influence (up to 70 %) between 355-370 K in agreement with the convective fraction estimated from observations of CO<sub>2</sub> and of freshly nucleated small particles.

Trajectories calculated from the mesoscale model simulation were used to estimate the convective age in order to identify when and where uplift occurred. The time since convective uplift ranges between 18 and 24 hours in the main convective layer but is more variable (between 20 and 96 hours) above 355 K showing that



deep convection in the central Sahel has a non negligible role in the uppermost troposphere, at least with respect to the formation of ice layers. The event of recent deep convection is characterized by the coexistence of air masses uplifted by recent and older convection; the last one being responsible of the presence of thin ice clouds. This is confirmed, at least on qualitative basis, by in-situ observations of CO<sub>2</sub>, water vapour and aerosol that show the presence in the upper troposphere of perturbed trace gas concentrations, hydrated air, and particles that are not always measured in the same air masses.



## Chapter 6

# Transport of biomass burning emissions

Biomass burning produces large quantities of pollutants which can be transported many thousands of kilometres downwind. This includes trace gases such as CO<sub>2</sub>, and precursors of O<sub>3</sub> as well as aerosols which can also have an important impact on radiative forcing. Inter-hemispheric transport of biomass burning plumes has been reported by many authors (e.g. Mari et al. (2008) and Sauvage et al. (2005)). They reported both (1) direct transport from emission region in the southern hemisphere to the gulf of Guinea by means of a southern hemispheric easterly jet blowing around 5S and 700hPa or, during the break phase of this jet, (2) north-westerly transport over the continent into the ITCZ followed by convective uplift and subsequent westward transport in the high troposphere due to the TEJ.

In this chapter we examine, using a BOLAM simulation including a biomass burning passive tracer, the origin of two pollution plumes observed in the Mid Troposphere (MT) and Upper Troposphere (UT) during August 2006 over the southern coast of West Africa during the AMMA project.

## 6.1 Observational evidence

Here, we focus on the analysis of plumes observed in the MT and also in the UT on 13 August 2006 when 4 aircraft flew to the Gulf of Guinea (UK BAe-146 (B-146), French Falcon-20 (FF20), DLR Falcon-20 (DF-20) and the M55-Geophysica (M55)). Figure 6.1 shows horizontal and vertical sketch of the flight of the DF-20, the B146 and M55 (see chapter 4) research flight together with measurements of CO and CO<sub>2</sub>. Enhancements of CO and CO<sub>2</sub> are visible between 2.5 and 4.5 km.

Figure 6.2 shows measurements taken by DF-20 (left panel) and Bae-146 (right panel). Layers with high concentrations of CO, CO<sub>2</sub>, PAN, NO<sub>x</sub>, O<sub>3</sub>, VOCs and aerosols were sampled between 2.5 and 4.5 km by the B-146, and 3 hours later by the DF-20 below 5.5 km (500hPa) over southern West Africa and the Gulf of Guinea. For example, the DF-20 measured up to 450 ppbv CO, 130 ppbv O<sub>3</sub> and more than 8 ppbv NO<sub>y</sub> (see figure 6.2). The NO:NO<sub>y</sub> was rather low (0.04) indicating that significant photochemical processing had taken place and therefore discounting local anthropogenic emissions as the origin.

The FF-20 (measurements not shown), which flew to the same region, also sampled air masses with elevated CO and O<sub>3</sub> at around 8km at 6N on the same day with an origin over the Gulf of Guinea according to Ancellet et al. (2009). The B-146 observed rather similar CO and O<sub>3</sub> concentrations especially in the upper part of their plume sampling suggesting that both aircraft sampled the same polluted air mass. The B-146 also sampled high levels of PAN (greater than 800 pptv) together with high acetonitrile, a strong indicator of BB emissions. The DF-20 plume also had high CO<sub>2</sub> concentrations up to 390 ppmv (mean value of 387 ppmv).

These observations strongly suggest the presence of a large BB plume over the Gulf of Guinea extending between about 3 and 6km: denoted the MT plume in the rest of the chapter. Interestingly, data collected on the 4 August 2006, when a similar flight was made over this region, also showed evidence for BB plumes

with elevated trace gas and aerosol concentrations, including CO<sub>2</sub> up to 379 ppmv Andrés-Hernández et al. (2009). This suggests that BB transport to West Africa in August is episodic.

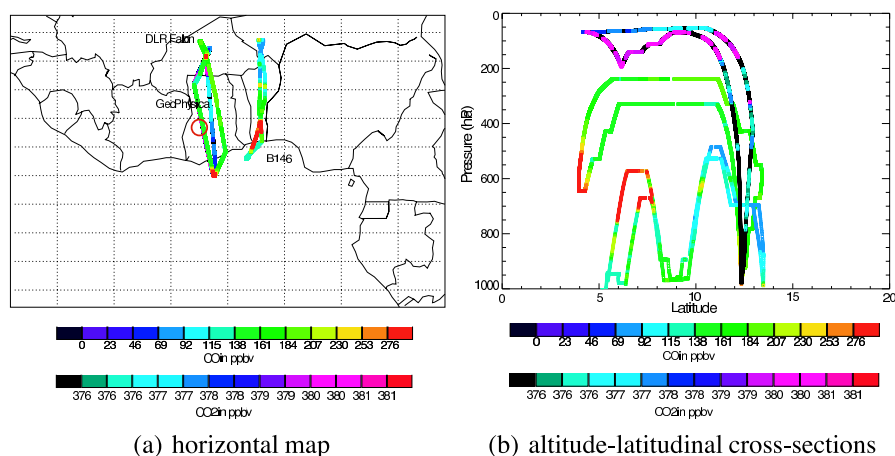


Figure 6.1: Flight path for 13 August 2006 flight. Colour scales represent the CO concentrations from the DF-20 and the B-146 and CO<sub>2</sub> concentrations for the M55 aircraft. See text for details.

The M55 aircraft flew on this day and figure 6.3 reports measurements of NO, NO<sub>y</sub>, O<sub>3</sub> and CO<sub>2</sub> sampled by the high altitude research aircraft. A plume was observed during a dive over the Gulf of Guinea down to 200 hPa (12 km): denoted the UT plume in the rest of the chapter. Observations showed elevated concentrations of trace gases and aerosols. Measurements of CO<sub>2</sub> in the dive (around 380 ppmv) were higher than measured at similar altitudes during the rest of the campaign. Higher CO<sub>2</sub> concentrations in the TTL are usually attributed to uplift of mid-latitude air masses several months earlier when surface concentrations are higher. However, CO<sub>2</sub> concentrations are also elevated in BB air masses (as in the MT plume observed by the DF-20 on the same day). O<sub>3</sub> concentrations were around 60 ppbv which is in the upper range of measurements collected at these altitudes during the rest of the M55 campaign (see figure 4.5).

The M55 plume also showed slightly elevated concentrations (up to 10000

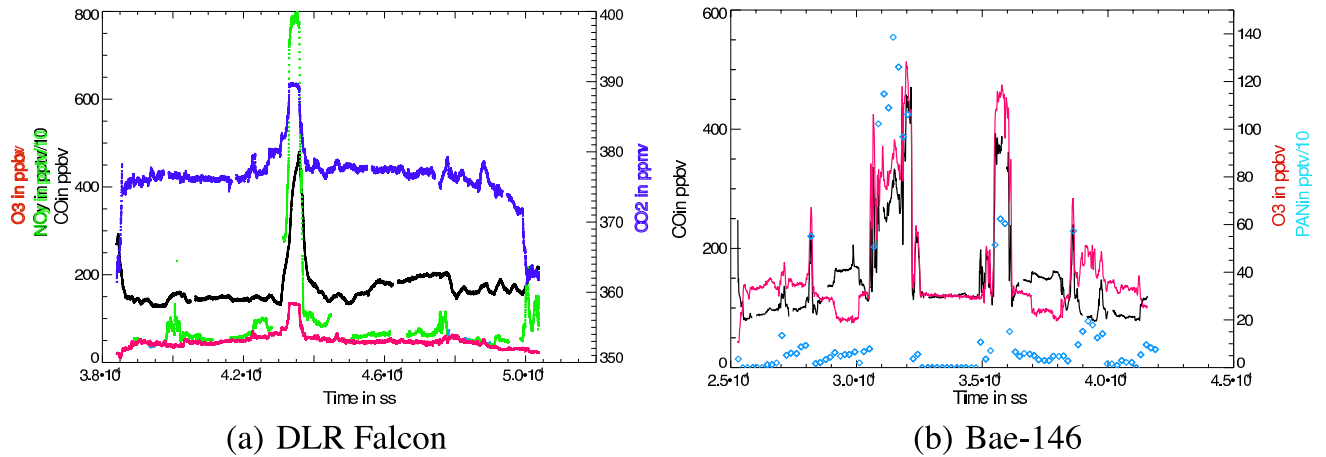


Figure 6.2: Measurements taken on 13 August 2006 by the DLR Falcon aircraft (left hand) and the Bae-146 (right hand).

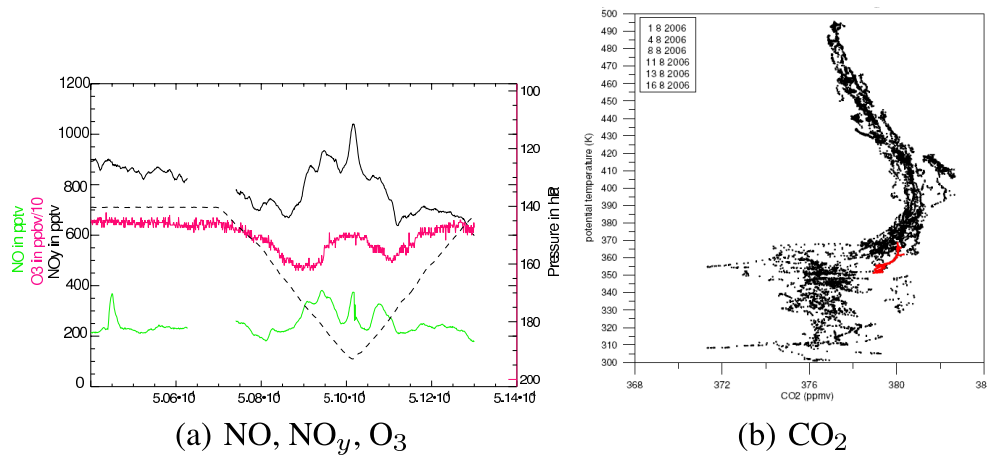


Figure 6.3: Right hand figure: Measurements of  $NO$ ,  $NO_y$  and  $O_3$  taken on 13 August 2006 by the GeoPhysica. Left hand figure: Measurements of  $CO_2$  taken during the whole campaign,  $CO_2$  measured during the dive on the 13 August is highlighted in red.

molecules per milligram of air) of fine-mode aerosol. This is in the upper range of measurements collected at these altitudes during the rest of the campaign (Borrmann et al., 2009). The fact that particle concentrations for sizes less than 6nm and less than 14nm are very similar indicates that no new nucleation had recently taken place. Analysis of other flights (4 and 11 August, 2006) when measurements of the non-volatile fraction are also available show that a significant fraction (up to 60%) of particles in the lower TTL were non-volatile and contained soot or non-volatile organic aerosols suggesting injection from a surface source such as BB emissions could be influencing upper tropospheric aerosol composition over West Africa (Borrmann et al., 2009). Finally, whilst CO was not measured on this day by the M55, the DF-20 and the FF-20 (Ancellet et al., 2009) also sampled plumes with elevated CO at around 11km over the southern coast of West Africa (see figure 6.2). Analysis of MOZAIC data collected between 1 to 16 August 2006 in the upper troposphere also shows the existence of several plumes between the Equator and 5N with CO concentrations above 150 ppbv and, in one case as high as 230 ppbv in the upper troposphere (240 hPa) (J. P. Cammas., pers. comm.) Examination of air mass origins in the TTL (350-380K, 250 to 50 hPa) for this campaign using ensembles of back trajectories from both the M55 flight paths and the TTL region over West Africa showed that 10 to 15% of the measured air masses up to 150 hPa probably originate from central Africa during the period 13 to 16 August.

In summary, it appears that the MT plume(s) has the characteristics of a BB origin with high concentrations of trace gases (including BB tracers) and aerosols. Considering the UT plume, high CO<sub>2</sub> concentrations and aerosols indicate a BB origin and a low NO : NO<sub>y</sub> ratio (around 0.3) indicates that air mass may also have been influenced by LiNO<sub>x</sub> emissions associated with deep convection.

So it is necessary to identify the transport processes influencing the plumes positions in order to asses if BB emissions, located in the African southern

hemisphere, could have been transported in the measurements area and which is the age of such air masses. To do so, in the next section we present a simulation performed with a new version of the BOLAM model that include the transport of a CO like passive tracer.

## 6.2 Model description and simulation set up.

The objective is to quantify, using the BOLAM model, the relative fractions of BB pollutants transported in the UT compared to the MT and to investigate how long it took the pollutants to arrive over southern West Africa where the measurements were taken. We also use the model results to estimate dilution rates for the UT plume in the chemical trajectory model calculations.

The BOLAM model (section 3.2) simulations discussed here were run over the domain shown in figure 6.4 with a horizontal resolution of  $0.26^\circ \times 0.26^\circ$  ( $24 \times 24$  km) and 38 hybrid sigma vertical levels from the ground to 10hPa. The model was initialized using  $0.5^\circ \times 0.5^\circ$  European Centre for Medium Range Weather Forecast (ECMWF) meteorological analyses at 00UT on 15 July 2006 and run for 32 days until 00UT on 16 August 2006. ECMWF analyses were also used to update the lateral boundary conditions every 6 hours. Time-varying CO-like BB tracer emissions were introduced into the model for the duration of the run. Daily fire emissions were interpolated from 5-day running-mean averaged emissions taken from the AMMA African BB inventory compiled by Lioussé (personal communication), specifically for 2006. Separate tracers were injected daily for 24h up to an altitude of 1 km and then transported for the rest of the simulation, in order to follow the fate of BB plumes emitted on each day of the run. Figure 6.5 shows the BB CO emissions averaged between 15 July and 15 August 2006 together with the ECMWF wind field at 750 hPa averaged over the same period. Two transport pathways for the BB plumes in lower troposphere to the north-east



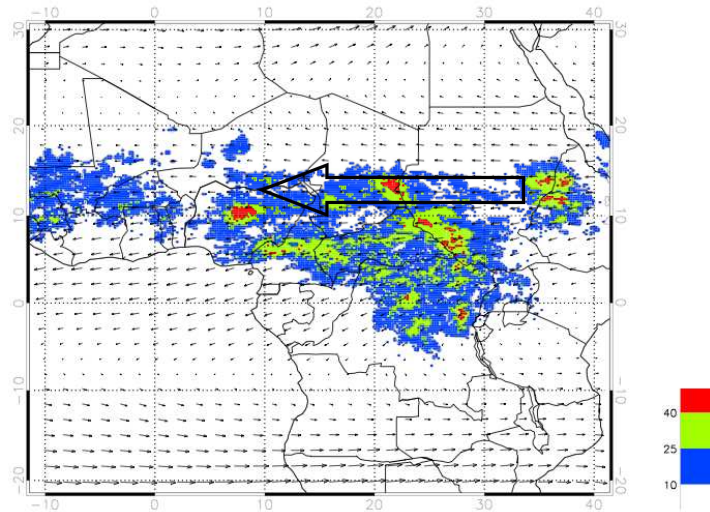


Figure 6.4: Observed percentage of cloud cover for cloud top brightness temperature less than 230K. Percentage is relative to the period 15 July - 15 August. Thin arrows are ECMWF wind field at 250 hPa averaged over the same period.

over the continent and to the north-west toward the Gulf of Guinea are highlighted by thick arrows.

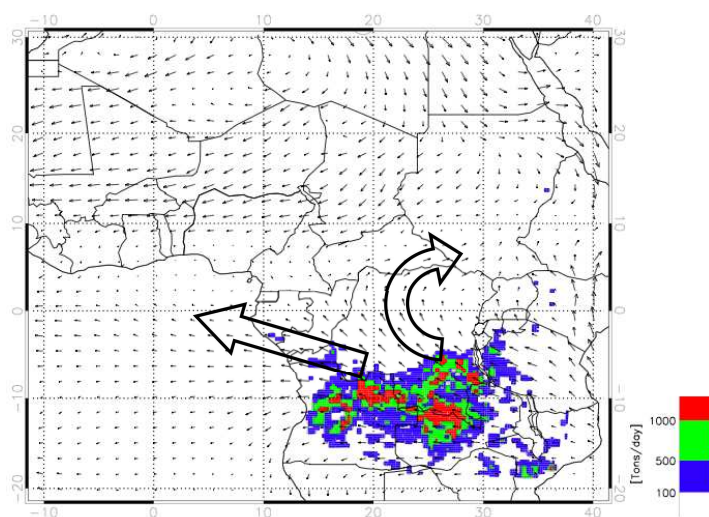


Figure 6.5: CO flux averaged between 15 July and 15 August. Thin arrows are ECMWF wind field averaged between 15 July and 15 August at 750 hPa.

## 6.3 Biomass burning transport

In this section the model capacity to reproduce convective activity was first evaluated. Then the model time distribution of BB tracers was studied (from 15 July to 15 August), showing the episodic nature of transport in equatorial regions both in the UT and the MT. Different pathways for UT and MT plumes were simulated and the ratio of tracers transported in the UT to those transported in the MT was evaluated and compared with measurements. Finally the plumes age over West Africa was evaluated using modelled tracers.

The performance of the BOLAM model in reproducing convective activity was evaluated, analogously to the previous chapter, using cloud top brightness temperatures derived from the 10.8 micrometer channel of the SEVIRI radiometer, on-board of MSG satellite. These values were compared with cloud top brightness temperatures evaluated from BOLAM model and averaged over the whole simulation (15 July - 15 August 2006). Figures 6.4 and 6.6 shows the regions where convective activity at 18UTC, individuated by CTBT lower than 230 K, occurs more than 10%, 20% and 40% of the times over the analysed period.

A comparison between a satellite and cloud derived percentage of cloud cover shows that the model reproduces reasonably well the structure and intensity of convective activity. The position of the intertropical convergence zone in West Africa is displaced northward in the model by about 5 degrees between 10W and 10E while its northern extent between 10E and 40E is well simulated. However, BOLAM simulates less convective activity in Democratic Republic of Congo, Cameroon (around 13E-5N) and Nigeria (7W-5N) and overestimates occurrence of convection in Central African Republic, Sudan and Chad (longitude 15-25 latitude 5-15).

Figure 6.7 shows the time evolution of tracer profiles averaged over three different areas highlighted in figure 6.4. In these and subsequent figures we only display CO tracers which are 20 days old or younger based on estimates of the

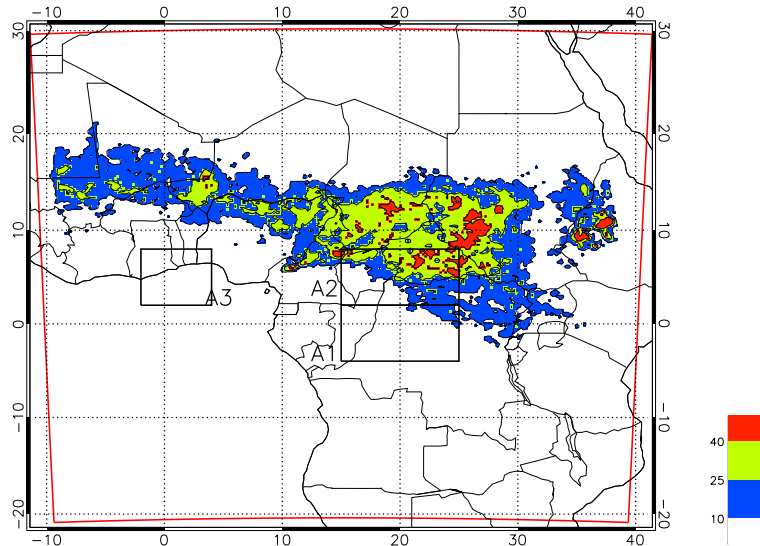


Figure 6.6: Percentage of cloud cover for model-derived cloud top brightness temperature less than 230K. Cloud Percentage is relative to the period 15 July - 5 August. Squares indicate the averaging area used in Figure 6.7.

chemical of CO lifetime in the lower tropical troposphere Mauzerall et al. (1998). Area A1 is located just to the north of the emission region and area A2 is located further north, where convective uplift of polluted air masses from lower troposphere could be active. Note that results are not shown below 900hPa over these regions due to the presence of mountains. Area A3 is located in the region where the aircraft observed the polluted plumes on 13 August.

Significant tracer arrives in A1 and A2 in the mid-troposphere starting on 17 July in the region A1, and later from 22 July in A2. There is significant variability in the modelled tracer transport which depends on the daily position of fires and the intensity of the low level winds. Three episodes of high BB tracer concentrations are clearly visible in A1 in the lower troposphere. The first one between 3-11 August 2006 corresponds reasonably well with the break phase of the southern African Easterly Jet (AEJ-S) described by Mari et al. (2008) when pollutants build up over

the continent, even if the model has higher concentrations and simulated tracers for longer over this region than simulated tracer by Mari et al. (2008). Injection into the UT is also episodic and depends on the position of convective activity relative to the availability of pollutants (tracer) at lower altitudes.

There is a clear increase in MT and UT tracer after the 5 August, especially in A2 where the convection is active. At mid-levels (around 650 hPa) over West Africa enhancements in A3 tracer concentration are seen between 27-29 July, 2-5 August and after 14 August. In the UT tracer arrives, albeit with low values, around 1 August with a more intense peak after the 14 August. This later enhancement corresponds well with the plume location measured by the M55 even if the modelled plume arrives around 1 day later. The plume is quite dispersed in the vertical (200 hPa - 400 hPa), this may be supported by observations since the DF-20 may have also sampled a BB plume around 11km (250 hPa) (see figure 6.2).

Examination of tracer concentrations at different altitudes shows that the MT and UT BB tracer follow different pathways. During the break phase (e.g. 3-11 August in the model) what becomes UT tracer is uplifted by wet convection in the area around the equator spanning in longitudes between 15 and 25E, and in the area around 5N 22E. The MT tracer is transported into the mid-troposphere south of the equator between 10 and 23S, where wet convection is absent according to the model or less intense according to the satellite cloud measurements (see figure 6.6 and figure 6.4). Then, it can be transported vertically by dry convection and the baroclinic circulation cell described by Sauvage et al. (2005).

The ratio of tracer in the MT versus UT ( $\text{Tracer}_{\text{UT}} / \text{Tracer}_{\text{MT}}$ ) can be estimated using observed CO<sub>2</sub> enhancements above background in both plumes and compared with results from the BOLAM model. Enhancements of about 11 ppmv and 4 ppmv are measured for the MT and UT plumes, respectively (see figure 6.2 and figure 6.3). The ratio between the deviations of measured concentration from mean value in the UT and MT is around 0.36. Taking into account the 24

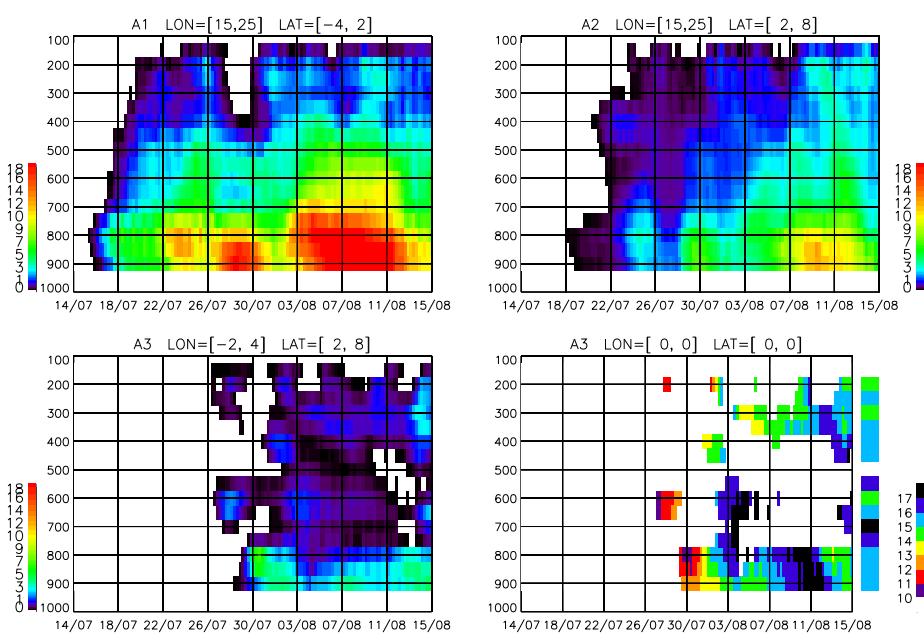


Figure 6.7: Hovmoller plot of tracer concentration profiles (top and bottom left panels). Limits of the three averaging areas are reported on the top of each panels (see also figure 6.4). Tracer travel time for averaging area A3 is presented in bottom right panel (colour scale indicates days from emission).

hour delay in higher modelled concentrations reaching the measurement location, we use model results on 14 and 15 August to estimate the same ratio of UT (200 hPa) to MT (650 hPa) tracer. The area selected to evaluate the ratio was chosen to contain almost all the plumes and spans from 10S to 15N and 10W to 10E. The UT:MT ratio varies between 0.3 and 0.6 between 14-15 August, with an average of 0.42 over this period which is similar to that derived from the CO<sub>2</sub> measurements.

Values inferred from Mari et al. (2008) suggest a lower fraction transported into the upper troposphere (0.05-0.2) based on study using a Lagrangian trajectory model driven with ECMWF winds over the region encompassing 30W-10E. The UT:MT ratio was also calculated for a longer period from 1-15 August including also wake phases of the AEJ-S. To take into account the variability of the vertical position and thickness of the plumes, two pressure layers were used: [800 hPa - 500 hPa] and [500 hPa - 150 hPa]. 500 hPa was chosen since the model shows a discontinuity in tracer concentration at this altitude which can be interpreted as the transition between the UT and MT transport pathways. The ratio over this period varies between 0.25 and 1, giving 0.6 on average. Therefore, according to the model, a significant fraction (higher than previously reported) of BB emissions can be transported into the UT but this fraction remains lower than those transported in the MT.

These differences in tracer concentrations are due to in-mixing of non polluted air masses during the deep convective uplift and due to dispersion by wind fields. In fact, entrainment and detrainment of ambient air within the vertical column is kept into account in the model convective parameterization leading to tracer mixing with cleaner air masses. Dispersion also occurs in the outflow region due to divergent winds that forms at the top of uplift column.

Since we emitted one tracer per day the results can also be used to estimate the time since emission as a function of altitude. This time since emission is obtained with a weighted mean of the tracers emitted on each days, weighted with their

concentrations. Results over A3 are shown in figure 6.7 averaged over the whole simulation period. The time for tracer to arrive over West Africa with maximum modelled concentrations in the UT (14 August) at 200hPa is 14 to 15 days whereas the MT plume takes between 16 to 17 days.

An estimate of the time needed by pollutants to travel between areas A1/A2 and area A3 was also estimated by dividing the longitudinal distance between the centres of areas A1 and A2 (20E) and the centre of area A3 (1E) by the zonal wind speed averaged between 11-15 August and averaged over the region encompassing areas A1, A2 and A3 (4S and 8N; 2W and 25E). We derive a transit time of 4-5 days for the MT plume and 1-2 days for the UT plume. This is faster than the 8 days reported by Sauvage et al. (2005). However, that study was based on a climatological (1997-2003) analysis of MOZAIC profile data, and could be due to differences in wind speeds between different years and our results suggest that this transport can be much faster in certain cases.

In this chapter we analysed the inter-hemispheric transport of biomass burning plumes coming from southern hemispheric wild fires occurring during the boreal summer.

Pollutant plumes with enhanced concentrations of trace gases and aerosols were observed over the southern coast of West Africa during August 2006. Plumes were detected both in the mid and upper troposphere by 4 research aircraft. We performed a simulation with a new version of the BOLAM mesoscale model including a biomass burning tracer confirming that the origin of the plumes are wild fires located in the southern hemisphere.

The plumes observed in the mid troposphere had significantly higher pollutant concentrations than the plume observed in the upper troposphere. The mesoscale model reproduces these differences and shows two different pathways for the plumes



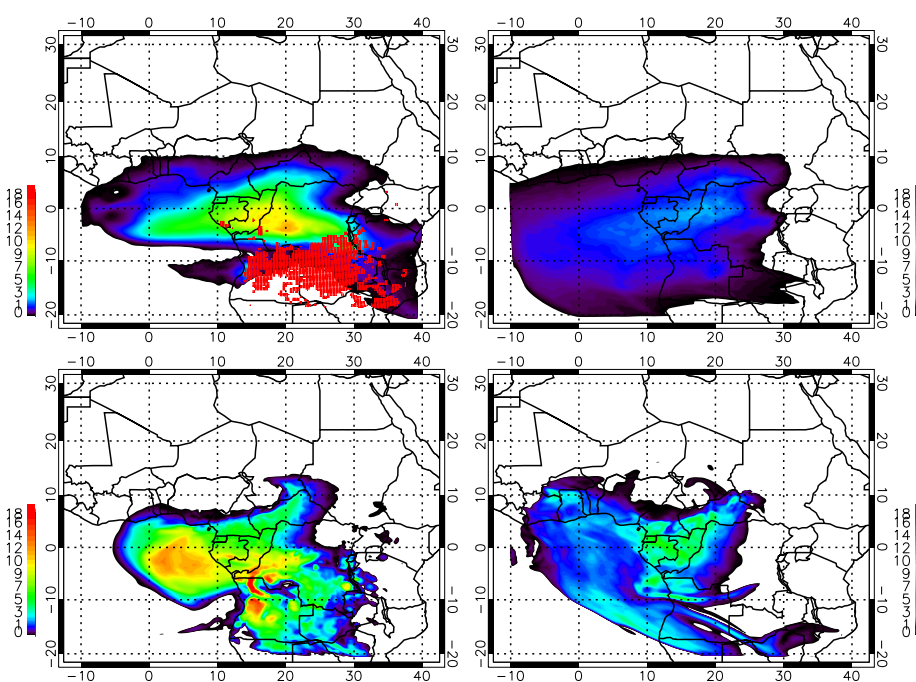


Figure 6.8: Tracer concentrations on 9 August 18UTC at 650 hPa and 200 hPa (respectively upper left and right panel), 15 August 18UTC at 650 hPa and 200 hPa (respectively bottom left and right panel)

at the different altitudes: transport to the north-east of the fire region, moist convective uplift and transport to West Africa driven by the tropical easterly jet for the upper tropospheric plume; north-west transport from the emission region to the Gulf of Guinea for the middle tropospheric plume.

The UT:MT ratio of tracer concentrations at 600hPa and 250hPa was estimated to around 0.42 for the period 14-15 August in the region of the measurements which agrees well with the ratio derived from observed CO<sub>2</sub> enhancements in the plumes. Lower pollutants concentrations in the UT are mainly due to more dilution with cleaner air masses during upward transport. A mean UT:MT fraction of 0.6 was evaluated over the period 1-15 August showing that even if injection of pollutants into the UT over West Africa is less frequent and plumes more diluted, it is significant, at least in the studied period (August 2006).

Time since emission results showed that BB pollutants were confined over central Africa for between 9-10 days (MT plume) and 12-13 days (UT plume) before being transported to the measurement region 4 days (MT plume) and 2 days (UT plume) later. According to the model both plumes are about 14 days old when measured over West Africa.

# Chapter 7

## Seasonal scale re-analysis

This study has been put at the end of the thesis because it is somehow distinct and represent a follow-up of the work carried out in the framework of the PhD. In the rest of the manuscript the simulations were adapted to study processes with time scales ranging from the single MCS event (1-2 days) up to the inter-hemispheric transport of biomass burning plumes (around 15 days). In the following paragraph two seasonal simulations, with and without assimilation, are presented to assess the capability of the BOLAM model in reproducing the intra-seasonal variability and total amount of precipitation in Africa during the whole 2006 wet season.

The assimilation scheme is used and its ability in improving the precipitation is evaluated in terms of total amount, spatial distribution and seasonal evolution over sub-Saharan and Sahelian areas. Simulations cover a period of 79 days, starting on the 15 June and ending on 31 August 2006. For the simulation named Nudg-4h the nudging scheme has been used throughout the simulated period; a value of 4 hours for the  $\tau$  parameter has been used to apply a smooth nudging to the model (see paragraph 3.4 for further details). The other simulation named Free-run has been run without assimilation. Boundary and initial conditions for both seasonal simulations are ECMWF AMMA reanalyses Agusti-Panareda et al. (2009), they differ from operative analyses because radiosoundings and dropsondes data

collected during the AMMA field campaign have been assimilated into the ECMWF model.

Seasonal simulations have been divided in 3 monthly simulations: June (15-30 June), July (31 June-31 July) and August (31 July-31 August). The BOLAM model has been reinitialised each month and the first day of July and August simulation are used to spin up the model and are not utilised for the comparison with precipitation. Horizontal grid spacing is  $0.22^\circ \times 0.22^\circ$  (corresponding to  $24 \text{ km} \times 24 \text{ km}$ ). 38 vertical levels (spanning from the ground to 1 hPa) are used and vertical resolution varies from around 50 m close to ground and around 800 m at the tropopause. Model domain has been extended further East to include the whole African part of the ITCZ, it is shown by the black box in figure 7.1.

Firstly we compare mean precipitation from each monthly simulation with the two rainfall product TRMM 3B42 and GPCP 1DD. In figure 7.2 averaged rainfall rates (mm/day) for the period 15-30 June are shown. TRMM and GPCP rainfall patterns and amount are similar over the Western part of the rainfall band but disagree eastern than 10E. GPCP shows higher rainfall rates in the area around 10W 10N; furthermore, the rain band reproduced by GPCP is north displaced with respect to the TRMM one. Those disagreements leads to a difference of 0.7 mm in the mean rainfall rate (see table 7.2) over the area LON=[20W-40E] and LAT=[0-18N], blue box in figure 7.1. A study of Nicholson et al. (2003) showed that GPCP product has small seasonal bias (0.1 mm/day) in West Africa while TRMM merged product doesn't.

Adeyewa and Nakamura (2003) compared TRMM 3B42 product and GPCP 1DD over major climatic regions in Africa against precipitation analyses based on rain gauges on a 3-year period (1998-2000). They found that both products overestimates precipitation over the semiarid region (defined as LON=[11W-30E] and LAT=[12N-15N]) and savanna region (LON=[11W-30E] and LAT=[8N-12N]). Compared with rain gauges estimates, GPCP 1DD daily precipitation is 0.6

mm/day higher over semiarid region and 1 mm/day higher over savanna region on June-July-August period. While TRMM 3B42 product overestimates are 0.3 mm/day and 0.2 mm/day over savanna and semiarid region respectively.

The averaging area used in the present work includes those used by Adeyewa and Nakamura (2003) and the difference in rainfall rate reported here are in good accord with results obtained by Adeyewa and Nakamura (2003) for what concerns TRMM versus GPCP comparison. Dinku et al. (2006) compared these rainfall products over complex terrain in Ethiopian highlands for the period 1998-2004. They also found that TRMM 3B42 precipitation better agrees with the rain gauges network measurements than GPCP 1DD. So, we will consider TRMM precipitation estimates as the reference value and use the GPCP 1DD product to have an estimation of the variability of the blended satellite precipitation products.

Concerning the BOLAM model, Nudg-4h simulation is in agreement with GPCP precipitation patterns; it overestimates TRMM precipitation eastern than 10E with too high rain-rates north of 10N. Nudg-4h rainfall rates are overestimated with respect to both observational data-sets considered, leading to an overestimate of the mean rainfall rate of 1.8 mm/day and 1.1 mm/day with respect to TRMM and GPCP respectively. Free-run simulation largely overestimates (up to 5 times) precipitation, in particular north of 10N. Mean rainfall rates are overestimated by a factor of two with respect to TRMM. It is worth noting that nudging procedure greatly improves precipitation patterns and reduce the rainfall overestimate north of 10N.

Figure 7.3 shows July rainfall rates averaged over the blue box shown in figure 7.1. In July TRMM and GPCP precipitation patterns are more similar than in June even if, in the area surrounding 10W 10N, GPCP still overestimates the rain-rate. The latitudinal position of the rainfall band is the same for the two satellite precipitation estimates. Concerning GPCP monthly mean rainfall rate, it is 0.7 mm/day higher than TRMM one. Also in July the Free-run simulation largely

overestimates precipitation, in particular in the latitudinal band spanning from 10N to 18N, with an average rainfall rate of 6.3 mm/day (2.2 mm/day higher than TRMM). Nudg-4 simulation shows a better agreement with satellite precipitation estimates. Rainfall patterns match with TRMM ones apart from an overestimation on the Ethiopian highlands (38E 10N) and downwind from Guinea highlands (10W 10N). Assimilation of CTBT reduces the mean rainfall rate overestimation from 2.2 mm/day (Free-run) to 0.9 mm/day (Nudg-4h).

In August (figure 7.4) the comparison between the two satellite rainfall products shows an overestimate of GPCP East of 20E and around 10W 10N, leading to a mean rainfall difference of 1.1 mm/day. Free-run simulation presents the same differences with respect to satellite precipitation products as in July and overestimates TRMM mean rainfall by 2.2 mm/day. Nudged simulation presents similar overestimates over Ethiopian highlands while underestimates rainfall rates over the region around 10E 10N. The Nudg-4h mean rainfall rate is much closer to the one evaluated using precipitation satellite estimates than Free-run one, lying between GPCP and TRMM mean rainfall rates.

Table 7.1: Mean June July and August monthly precipitation (mm/day) for TRMM, GPCP and the two BOLAM simulations averaged over LON [20W;40E] LAT [0;18N], corresponding to the blue box in 7.1 .

	June	July	August
TRMM	2.9	4.1	4.2
GPCP	3.6	4.7	5.3
<i>Nudg-4</i>	4.7	5.0	4.9
<i>Free-run</i>	5.4	6.3	6.4

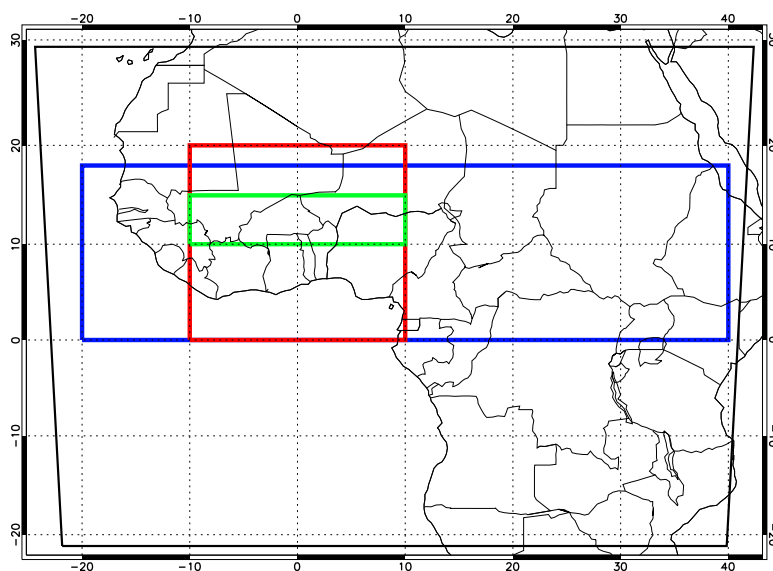


Figure 7.1: Simulation domain and averaging boxes used in the text. Sub-Saharan region (LON[10W,10E]; LAT[0,20N]) in red. ITCZ region (LON[20W,40E]; LAT[0,18N]) in blue. Sahel region (LON[10W,10E]; LAT[10N,15N]) in green.

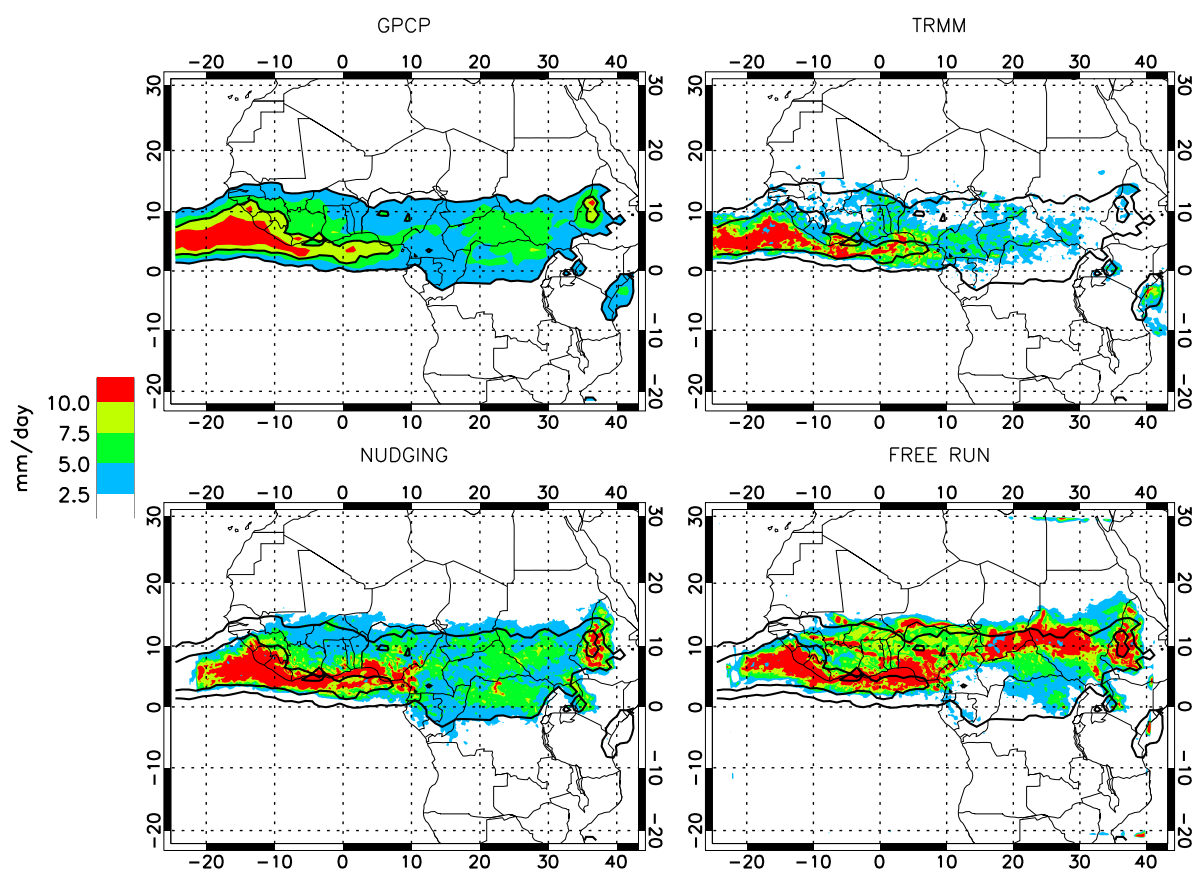


Figure 7.2: Mean June 2006 rain-rate (mm/day) for GPCP [top left], TRMM [top right], Nudg-4 simulation [bottom left] and Free-run simulation [bottom right].



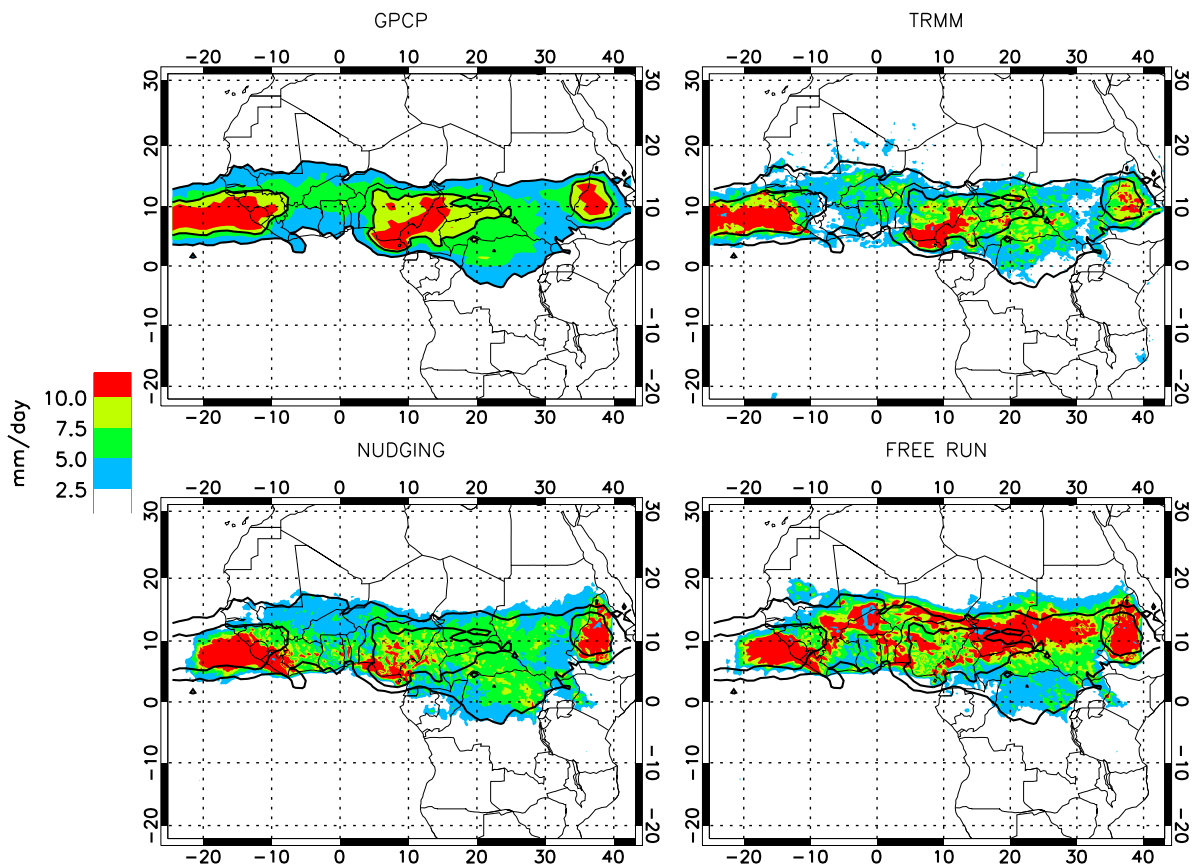


Figure 7.3: Mean July 2006 rain-rate (mm/day) for GPCP [top left], TRMM [top right], Nudg-4 simulation [bottom left] and Free-run simulation [bottom right].

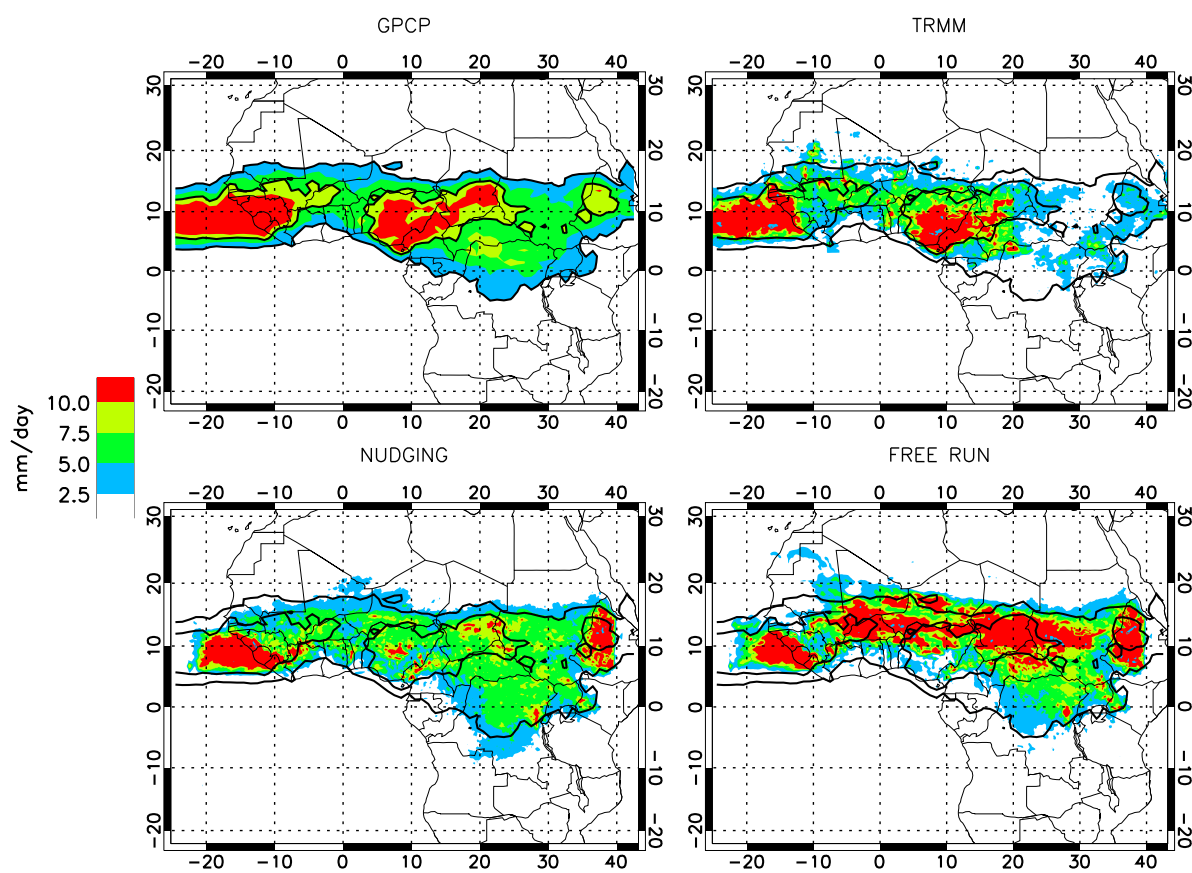


Figure 7.4: Mean August 2006 rain-rate (mm/day) for GPCP [top left], TRMM [top right], Nudg-4 simulation [bottom left] and Free-run simulation [bottom right].

Figure 7.5 shows the Hovmoller (time vs. latitude) plot of precipitation averaged over the longitudinal band 10W-10E (red box in figure 7.1) for TRMM, GPCP and BOLAM simulations. This kind of plot is useful to evaluate the model capability in reproducing the African summer monsoon onset, defined as the abrupt latitudinal shift of the inter tropical convergence zone (ITCZ) from a quasi-stationary location at 5N in May-June to a second quasi-stationary location at 10N in July-August. Sultan and Janicot (2003) found that the transition phase between the two stationary positions of ITCZ is accompanied by low convective activity over West Africa. Janicot et al. (2008) locate this transition period between 25 June and 10 July for summer 2006. This transition period is enclosed within the two red vertical lines in figure 7.5.

It can be seen from the two upper panels in figure 7.5 that in the transition period both satellite estimates report low precipitation north of 5N. This feature is better caught by Nudg-4 simulation than Free-run that exhibits much higher precipitation values north of 5N in that period. In the Sahelian region GPCP and TRMM exhibits very similar time evolution of the rain band even if total precipitation over the period under exam is still very different: 376 mm for TRMM and 464 mm for GPCP, as reported in table 7.2.

Nudg-4h simulation correctly reproduces the latitudinal position of the rain band in the Sahelian region, also rain maxima positions and timing is in accord with TRMM and GPCP. A general tendency in generating too much low intensity precipitation is notable, furthermore Nudg-4 simulation is not able to catch the rain minima visible in both GPCP and TRMM. This because nudging procedure is not activated if model or MSG cloud temperature is below 230 K, threshold chosen to select only deep convection. Thus, when model rain is not due to deep convection, the nudging procedure can't help in improving model precipitation.

Free-run simulation tends to generate a too northward displaced rain band, in particular during August, when almost all precipitation is between 10N and 20N.

Regarding the total precipitation, see table 7.2 Nudg-4 shows a much better accord with TRMM while Free-run presents strong overestimation in the Sahelian region, with a total precipitation around twice the TRMM one.

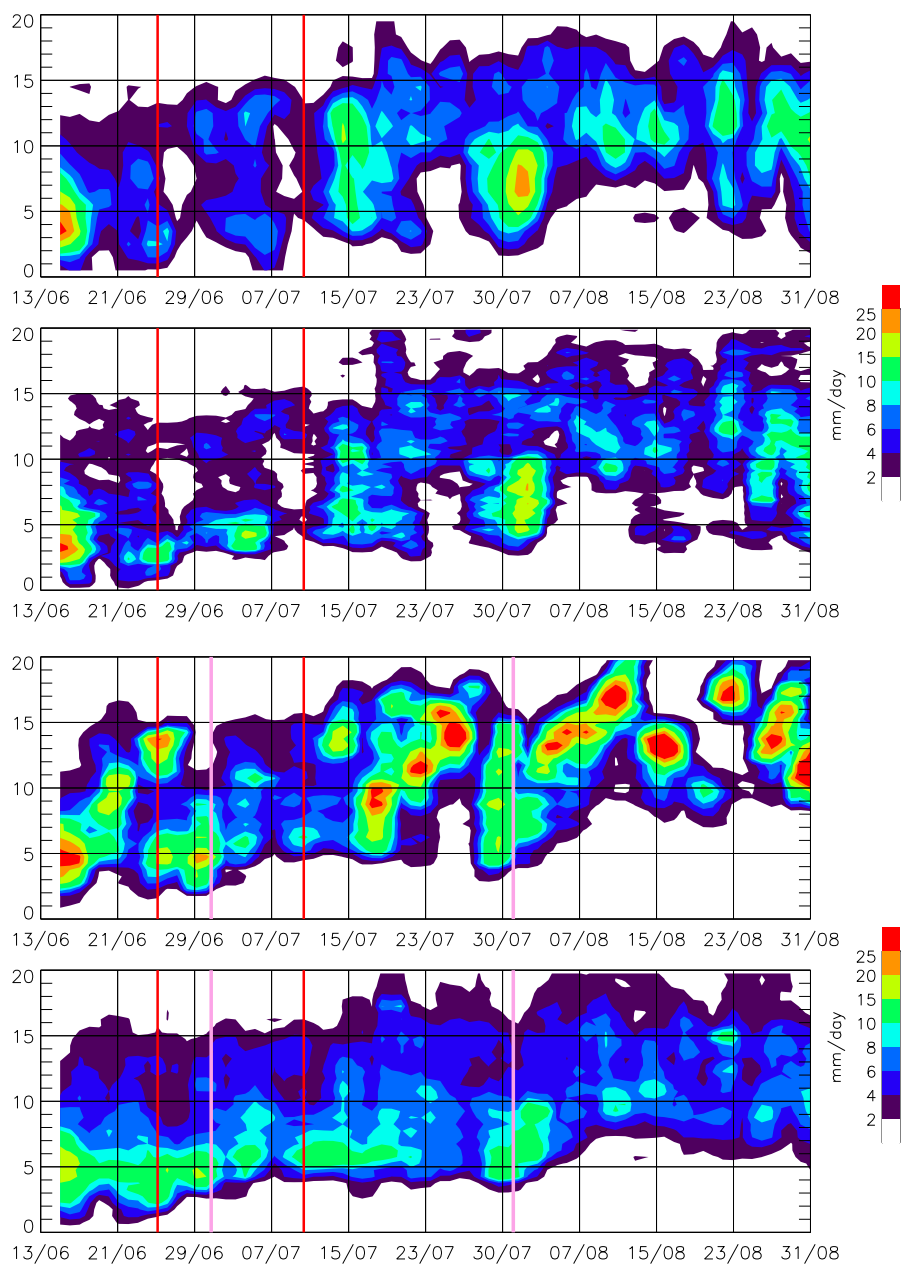


Figure 7.5: Hovmöller plot of precipitation averaged over longitude bands ranging from 10E to 10W. From top to bottom: GPCP, TRMM, Free-run and Nudg-4. Red lines enclose the West African monsoon onset period. Pink lines indicate 1st of July and 1st of August.

Here we make a comparison between rain gauges measurements, satellite products and model simulations. The comparison is restricted over two small areas where numerous rain gauges measurements were conducted within the AMMA-CATCH experiment. Among other goals, the AMMA-CATCH experiment focus on measuring and understanding land surface properties and processes in West Africa and the potential that surface hydrology may directly or indirectly affect monsoon dynamics and rainfall in the region, see for further details Lebel et al. (2009a). In the present work, rain gauge measurements were interpolated with an inverse distance method over two boxes B1 (LON[1.5,3.5]; LAT[12.5,14.5]) and B2 (LON[1.2,3.2]; LAT[8.8,10.8]), highlighted by blue and red boxes in fig 7.6. Table 7.2 shows accumulated precipitation (mm) for the June-July-August period. In area B1 TRMM shows a perfect agreement with gauge measurements while GPCP slightly underestimates measurements. Nudg-4h performs clearly better than Free-run. Free-run accumulated total precipitation over B1 is almost twice the gauges value. In area B2 TRMM has again the best agreement, Free-run overestimates gauge measurements. Nudg-4h slightly underestimates the reference value but gives a better agreement than GPCP.

This comparison is far from being a comprehensive validation of GPCP and TRMM precipitation satellite estimates because it is performed over a too small area. It could be intended as a first test of precipitation downscaling over restricted geographical areas. In a possible extension of this study we would make a rain-gauge versus model comparison for gauges located in various longitude within the Sahelian area and using a multi-year mesoscale simulation. This would be useful to asses the capability of the model in reproducing the marked difference between interannual variability of precipitation between western and eastern Sahel (Ali and Lebel, 2009).

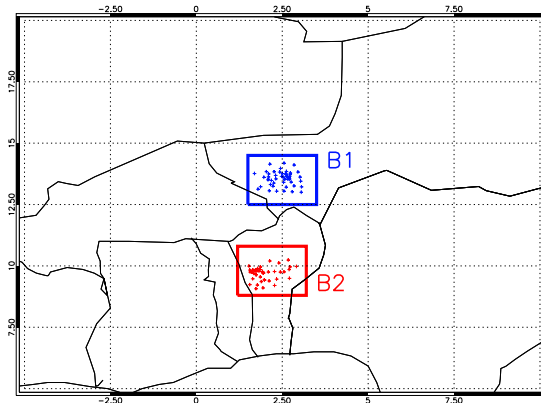


Figure 7.6: Rain gauges position and averaging box B1 and B2. Only rain gauges with all the daily precipitation values are used in the text and plotted here.

Table 7.2: Mean precipitation (mm) for TRMM, GPCP and the two BOLAM simulations averaged over two areas: West Africa LON [10W;10E] LAT [0;20N] and Sahel LON [10W;10E] LAT [10N;15N].

	West Africa	Sahel	AREA1	AREA2
TRMM	281	376	398	452
GPCP	313	464	363	418
<i>Nudg-4</i>	322	399	358	435
<i>Free-run</i>	417	709	735	564
Rain gauges			396	491

Here we presented the validation of the nudging scheme, introduced in chapter 3, for a seasonal mesoscale simulation covering the whole West African area. Therein the nudging scheme is used throughout the period to obtain a reanalysis for the June-July-August 2006 period. The nudged and non-nudged simulations are compared against satellite precipitation estimates to assess the capability of nudging scheme in improving seasonal rainfall. The assimilation of cloud top brightness temperature greatly improves the spatial patterns and the amount of

rainfall generated by the BOLAM model over a seasonal time-scale. This high temporal (1 hour) and spatial (24 km) reanalysis would allow a detailed study of the water fluxes between the atmosphere and the soil-vegetation or it could be taken as an input for soil models studying the soil runoff and the discharge of river basins.



# Conclusions

The dynamic of MCS during boreal summer African monsoon and their predictability is a key issue for both precipitation forecast and atmospheric composition. In this study we addressed this twofold issue using both mesoscale modelling studies and a wide typology of measurements obtained during the AMMA field campaign. The present research have been conducted in the frame of the AMMA project and shares with it some of its main objectives as the improvement of the forecast of the WAM over various time and spatial scales and the assessment of the impact of regional circulation and local convection on climate.

The use of modelling studies coupled with measurements, came from the need of models to be validated and improved in the region trough the use of measurements and, on the other hand, the need to separate and identify various processes in measurement due to atmospheric transport.

We started showing that regional meteorological models present severe weaknesses over west Africa. Over the time scale of the single organised convective event, mesoscale models are often not able to reproduce the exact location of MCSs' initiation, their speed of propagation and the amount of precipitation. Unrealistic initial and boundary conditions have a role in driving mesoscale models to incorrect representation of convection.

We proposed a method to improve the performances of mesoscale models in reproducing organised convective events through the implementation of a nudging scheme that forces water vapour in the lower troposphere using satellite

observations. We tested this assimilation scheme in a case of intense precipitation due to the development of two intense MCSs occurring over West Africa during the 2006 monsoon season. We estimated that the assimilation procedure (in forecast set-up) has a positive impact in terms of the FSS score for 13 hours after the end of the assimilation period and that the representation, position and speed of propagation of the MCSs is driven closer to observations. Furthermore the comparison of daily accumulated model and measured precipitation shows a positive impact in reducing the overestimation of total precipitation and in improving the spatial patterns.

In order to upscale the results obtained on a single event, we performed a seasonal mesoscale simulation covering west Africa during the whole monsoon season (presented in chapter 7). Therein the nudging scheme is used throughout the period to obtain a reanalysis for the June-July-August 2006 period. The assimilation of cloud top brightness temperature greatly improves the spatial patterns and the amount of rainfall generated by the BOLAM model over a seasonal time-scale.

The role of transport of chemicals and aerosols at local, regional and global scale is then analysed. The improvements achieved with the nudging scheme are used to characterise transport due to deep convection. Beside the amelioration of precipitation, an improvement of organised convection position and evolution as well as the coherent modification of the divergent wind above convective systems, is necessary for a correct description of the effect of deep convection over trace gases distribution.

Analysis of trajectories calculated with BOLAM model were used to calculate both the fraction of lower tropospheric air present at the main convective outflow level and the convective age of uplifted air masses. The fraction evaluated using BOLAM in the region of the main convective outflow varies between 20% and 90% for the 3 flights, with a mean value of 50%. This is in good agreement

with convective perturbation derived from observations of aerosol and chemical tracers. The MCS outflow for the 11 August flight is particularly well reproduced by BOLAM that gives a percentage of lower tropospheric air present in the 355-370 K layer up to 90%, in accord with observations of CO<sub>2</sub> and freshly nucleated small particles.

The impact on the atmospheric composition between the main outflow level and the tropopause is more difficult to assess due to different sources and the role of large-scale westerly transport processes. Nevertheless it is possible to identify a clear signature of local convection in observations; model aided analysis confirms the presence of direct injection up to the tropical tropopause by intense convective systems and indicates that composition is dependent on the residence time in the TTL after convective uplift.

Together with deep convective impact on the upper tropospheric composition, we studied the role of inter-hemispheric transport of biomass burning emissions. We used BOLAM mesoscale model simulation to investigate whether the measurements collected during the AMMA field campaign were influenced or not by biomass burning emissions occurring in the southern hemisphere.

Pollutant plumes with enhanced concentrations of trace gases and aerosols were observed over the southern coast of West Africa during August 2006. Plumes were detected both in the mid and upper troposphere by research aircraft. We ran the BOLAM mesoscale model including a biomass burning tracer to confirm that the origin of the plumes are wild fires located in the southern hemisphere. Model results showed BB pollutants confined over central Africa for between 9-13 days before being transported to the measurement region. According to the model both plumes are about 14 days old when measured over West Africa.

The plumes observed in the mid troposphere had significantly higher pollutant concentrations than the plume observed in the upper troposphere. The mesoscale model reproduces these differences and shows two different pathways for the plumes

at the different altitudes: transport to the north-east of the fire region, moist convective uplift and transport to West Africa driven by the tropical easterly jet for the upper tropospheric plume; north-west transport from the emission region to the Gulf of Guinea for the middle tropospheric plume. Lower pollutants concentrations simulated in the UT (in agreement with observations) are mainly due to more dilution with cleaner air masses during upward transport.

The work presented here proposes a methodology to improve the models' scores and qualitatively identify several atmospheric key transport processes. The analysis of the simulation with forecast set-up for the nudging scheme has shown that it is possible to improve the forecasting capabilities on a time window of about 12 hours after the end of the assimilation. Thus it can be used in an operational weather forecast frame to improve at least short-range forecast of precipitation events. It has been also shown that continuous nudging can simulate a correct distribution and propagation of MCSs, also improving precipitation.

A general follow-up of this work would be to provide an upscaling over longer time-scales (as done for precipitation in chapter 7) to assess the climatic relevance of the reanalysis carried out assimilating satellite data. In particular this could be useful for the detailed analysis of the water cycle and transport related to convection in the Sahelian region, which requires a correct positioning of MCSs and an accurate quantification of precipitation. This high temporal (1 hour) and spatial (24 km) reanalysis would allow a detailed study of the water fluxes between the atmosphere and the soil-vegetation or it could be taken as an input for soil models studying the soil runoff and the discharge of river basins.

Furthermore we presented a detailed analysis of the impact of local convection and biomass burning emissions transport over the African atmospheric composition. The completion of this work would be the characterisation of the

African contribution to global atmospheric composition and its radiative impact; this could be achieved both estimating outward fluxes from regional scale model seasonal simulations or using global chemistry transport models.



# Appendix A

## List of acronyms

AMMA	African Monsoon Multidisciplinary Analyses
AEJ	African Easterly Jet
AEW	African Easterly Wave
BOLAM	BOlogna Limited Area Model
BSR	aerosols Back-Scatter Ratio
CAPE	Convective Available Potential Energy
CTBT	Clout Top Brightness Temperature

---

D	aerosols Depolarization
ECMWF	European Centre for Medium-range Weather Forecast
EOP	Enhanced Observing Period
EPSAT	Evaluation des Pluies par SATellite (satellite evaluation of precipitation)
GOES	Geostationary Operational Environmental Satellite
GPCP	Global Precipitation Climatology Project
GPI	GOES Precipitation Index
ITCZ	Inter Tropical Convergence Zone
IR	Infra Red
LOP	Long term Observing Period
MCS	Mesoscale Convective System
MSG	Meteosat Second Generation
MOZAIC	Measurement of OZone on Airbus In-service aircraft
PM	Passive Microwave
RHI	Relative Humidity over Ice
RTTOV	Radiative Transfer for TOV
SOP	Special Observing Period
SSM/I	Special Sensor Microwave Imager
SST	Sea Surface Temperature
TEJ	Tropical Easterly Jet
TRMM	Tropical Rainfall Measuring Mission
TTL	Tropical Tropopause Layer
VOC	Volatile Organic Compound
WA	West Africa
WAM	West African Monsoon



# Appendix B

## List of simulations

Simulation name	Period beginning end	Domain LON LAT	Resolution	Nudging	Notes
<b>Chapter 2</b>					
BOLAM	00UTC 28/8/2005 00UTC 30/8/2005	[-8,24] [0,23]	12km	no	
<b>Chapter 3</b>					
Nudg-48H-2	00UTC 9/8/2006 00UTC 12/8/2006	[-8,24] [0,23]	12km	yes	48 hours nudging
Nudg-24H-2	00UTC 9/8/2006 00UTC 12/8/2006	[-8,24] [0,23]	12km	yes	24 hours nudging
Free-run	00UTC 9/8/2006 00UTC 12/8/2006	[-8,24] [0,23]	12km	no	
Simulations performed for sensitivity test are reported in table 3.1					
<b>Chapter 5</b>					
BOLAM	00UTC 4/8/2006 00UTC 14/8/2006	[-10,40] [-20,30]	24km	yes	continuous nudging
<b>Chapter 6</b>					
BOLAM	00UTC 15/7/2006 00UTC 15/8/2006	[-10,40] [-20,30]	24km	no	
<b>Chapter 7</b>					
Nudging	00UTC 15/6/2006 00UTC 1/9/2006	[-22,40] [-20,30]	24km	yes	continuous nudging
Free run	00UTC 15/6/2006 00UTC 1/9/2006	[-22,40] [-20,30]	24km	no	
Simulations in this chapter have been reinitialized on 30/06/2006 and 30/07/2006					

# Bibliography

- Adeyewa, Z. D. and K. Nakamura, 2003: Validation of trmm radar rainfall data over major climatic regions in africa. *Journal of Applied Meteorology*, **42**.
- Agusti-Panareda, A., A. Beljaars, I. Genkova, C. Cardinali, and C. Thorncroft, 2009: Impact of assimilating amma soundings on ecmwf analyses and forecasts, Tech. rep., ECMWF Technical Memorandum.
- Ali, A. and T. Lebel, 2009: The Sahelian standardized rainfall index revisited. *International Journal of Climatology*, **29**, 1705–1714.
- Ancellet, G., J. Leclair de Bellevue, C. Mari, P. Nedelec, A. Kukui, A. Borbon, and P. Perros, 2009: Effects of regional-scale and convective transports on tropospheric ozone chemistry revealed by aircraft observations during the wet season of the AMMA campaign. *Atmospheric Chemistry & Physics*, **9**, 383–411.
- Andreae, M., A. Chapuis, B. Cros, J. Fontan, G. Helas, C. Justice, Y. Kaufman, A. Minga, and D. Nganga, 1992: Ozone and Aitken nuclei over equatorial Africa: Airborne observations during DECAFE 88. *Journal of Geophysical Research-Atmospheres*, **97**.
- Andrés-Hernández, M. D., D. Kartal, L. Reichert, J. P. Burrows, J. Meyer Arnek, M. Lichtenstern, P. Stock, and H. Schlager, 2009: Peroxy radical observations over west africa during amma 2006: photochemical activity in the outflow of convective systems. *Atmospheric Chemistry and Physics*, **9**, 3681–3695.

- Arribas, A., C. Gallardo, M. Gaertner, and M. Castro, 2003: Sensitivity of the Iberian Peninsula climate to a land degradation. *Climate Dynamics*, **20**, 477–489.
- Barret, B., P. Ricaud, C. Mari, J.-L. Attié, N. Bousserez, B. Josse, E. Le Flochmoën, N. J. Livesey, S. Massart, V.-H. Peuch, A. Piacentini, B. Sauvage, V. Thouret, and J.-P. Cammas, 2008: Transport pathways of CO<sub>2</sub> in the African upper troposphere during the monsoon season: a study based upon the assimilation of spaceborne observations. *Atmospheric Chemistry and Physics*, **8**, 3231–3246.
- Bechara, J., A. Borbon, C. Jambert, A. Colomb, and P. E. Perros, 2009: Evidence of the impact of deep convection on reactive volatile organic compounds in the upper tropical troposphere during the amma experiment in West Africa. *Atmospheric Chemistry and Physics Discussions*, **9**, 20309–20346.
- Bechtold, P., M. Kohler, T. Jung, F. Doblas-Reyes, M. Leutbecher, M. Rodwell, F. Vitart, and G. Balsamo, 2008: Advances in simulating atmospheric variability with the ECMWF model: From synoptic to decadal time-scales. *Quarterly Journal of the Royal Meteorological Society*, **134**, 1337–1352.
- Bergès, J. C., I. Jobard, F. Chopin, and R. Roca, 2010: Epsat-sg: a satellite method for precipitation estimation; its concepts and implementation for the amma experiment. *Annales Geophysicae*, **28**, 289–308.
- Berry, G. J. and C. Thorncroft, 2005: Case study of an intense African easterly wave. *Monthly Weather Review*, **133**.
- Bertram, T., A. Perring, P. Wooldridge, J. Crouse, A. Kwan, P. Wennberg, E. Scheuer, J. Dibb, M. Avery, G. Sachse, et al., 2007: Direct measurements of the convective recycling of the upper troposphere. *Science*, **315**, 816.

- Borrmann, S., D. Kunkel, R. Weigel, A. Minikin, T. Deshler, J. C. Wilson, J. Curtius, G. N. Shur, G. V. Belyaev, K. S. Law, and F. Cairo, 2009: Aerosols in the tropical and subtropical ut/lis: in-situ measurements of submicron particle abundance and volatility. *Atmospheric Chemistry and Physics Discussions*, **9**, 24587–24628.
- Boulain, N., B. Cappelaere, D. Ramier, H. Issoufou, O. Halilou, J. Seghieri, F. Guillemin, M. O  
"1, J. Gignoux, and F. Timouk, 2009: Towards an understanding of coupled physical and biological processes in the cultivated Sahel–2. Vegetation and carbon dynamics. *Journal of Hydrology*, **375**, 190–203.
- Cairo, F., G. Di Donfrancesco, A. Adriani, L. Pulvirenti, and F. Fierli, 1999: Comparison of various linear depolarization parameters measured by lidar. *Appl. Opt*, **38**, 4425–4432.
- Cairo, F., J. P. Pommereau, K. S. Law, H. Schlager, A. Garnier, F. Fierli, M. Ern, M. Streibel, S. Arabas, S. Borrmann, J. J. Berthelier, C. Blom, T. Christensen, F. D'Amato, G. Di Donfrancesco, T. Deshler, A. Diedhiou, G. Durrý, O. Engelsen, F. Goutail, N. R. P. Harris, E. R. T. Kerstel, S. Khaykin, P. Konopka, A. Kylling, N. Larsen, T. Lebel, X. Liu, A. R. MacKenzie, J. Nielsen, A. Oulanowski, D. J. Parker, J. Pelon, J. Polcher, J. A. Pyle, F. Ravagnani, E. D. Rivière, A. D. Robinson, T. Röckmann, C. Schiller, F. Simões, L. Stefanutti, F. Stroh, L. Some, P. Siegmund, N. Sitnikov, J. P. Vernier, C. M. Volk, C. Voigt, M. von Hobe, S. Viciani, and V. Yushkov, 2009: An overview of the scout-amma stratospheric aircraft, balloons and sondes campaign in west africa, august 2006: rationale, roadmap and highlights. *Atmospheric Chemistry and Physics Discussions*, **9**, 19713–19781.
- Capes, G., J. G. Murphy, C. E. Reeves, J. B. McQuaid, J. F. Hamilton, J. R. Hopkins, J. Crosier, P. I. Williams, and H. Coe, 2009: Secondary organic aerosol

- from biogenic vocs over west africa during amma. *Atmospheric Chemistry and Physics*, **9**, 3841–3850.
- Chopin, F., J. Bergès, M. Desbois, I. Jobard, and T. Lebel, 2004: Multi-scale precipitation retrieval and validation in African monsoon systems, *2nd International TRMM Science Conference*.
- Cook, K., 1999: Generation of the African easterly jet and its role in determining West African precipitation. *Journal of Climate*, **12**, 1165–1184.
- Corti, T., B. Luo, M. de Reus, D. Brunner, F. Cairo, M. Mahoney, G. Martucci, R. Matthey, V. Mitev, F. dos Santos, et al., 2008: Unprecedented evidence for deep convection hydrating the tropical stratosphere. *Geophysical Research Letters*, **35**, L10810.
- Crutzen, P. and M. Andreae, 1990: Biomass burning in the tropics: Impact on atmospheric chemistry and biogeochemical cycles. *Science*, **250**, 1669.
- Curtius, J., 2006: Nucleation of atmospheric aerosol particles. *Comptes rendus-Physique*, **7**, 1027–1045.
- Delmas, R., J. Lacaux, J. Menaut, L. Abbadie, X. Roux, G. Helas, and J. Lobert, 1995: Nitrogen compound emission from biomass burning in tropical african savanna fos/decafe 1991 experiment (lamto, ivory coast). *Journal of Atmospheric Chemistry*, **22**, 175–193.
- Delon, C., C. E. Reeves, D. J. Stewart, D. Serca, R. Dupont, C. Mari, J.-P. Chaboureau, and P. Tulet, 2008: Biogenic nitrogen oxide emissions from soils: impact on  $\text{no}_x$  and ozone over west africa during amma (african monsoon multidisciplinary experiment): modelling study. *Atmospheric Chemistry and Physics*, **8**, 2351–2363.

- Dinku, T., P. Ceccato, E. Grover-Kopec, S. Connor, and C. Ropelewski, 2006: Validation and inter-comparison of satellite rainfall products over east african complex topography. *International Journal of Remote Sensing*, **28**, 1503–1526.
- Diongue, A., J. Lafore, J. Redelsperger, and R. Roca, 2002: Numerical study of a sahelian synoptic weather system: Initiation and mature stages of convection and its interactions with the large-scale dynamics. *Quarterly Journal of the Royal Meteorological Society*, **128**.
- Doms, G. and U. Schattler, 2002: A description of the nonhydrostatic regional model LM. *Part I: Dynamics and numerics*. *Deutscher Wetterdienst (German Weather Service)*. [Available online at <http://cosmo-model.cscs.ch/public/documentation.htm#p1>].
- Druyan, L., M. Fulakeza, P. Lonergan, and M. Saloum, 2001: A regional model study of synoptic features over West Africa. *Monthly Weather Review*, **129**, 1564–1577.
- Ebert, E., J. Janowiak, and C. Kidd, 2007: Comparison of near-real-time precipitation estimates from satellite observations and numerical models. *Bulletin of the American Meteorological Society*, **88**, 47–64.
- EUMETSAT, 2008: Effective radiance and brightness temperature relation for meteosat 8 and 9, Tech. Rep. EUM/OPS-MSG/TEN/08/0024, EUMETSAT.
- Fierli, F., G. Di Donfrancesco, F. Cairo, V. Marécal, M. Zampieri, E. Orlandi, and G. Durré, 2008: Variability of cirrus clouds in a convective outflow during the Hibiscus campaign. *Atmos. Chem. Phys*, **8**, 4547–4558.
- Fontan, J., A. Druilhet, B. Benech, R. Lyra, and B. Cros, 1992: The decafe experiments: Overview and meteorology. *Journal of Geophysical Research-Atmospheres*, **97**.

- Fu, R., A. Del Genio, and W. Rossow, 1990: Behavior of deep convective clouds in the tropical Pacific deduced from ISCCP radiances. *Journal of Climate*, **3**, 1129–1152.
- Fueglistaler, S., M. Bonazzola, P. Haynes, and T. Peter, 2005: Stratospheric water vapor predicted from the Lagrangian temperature history of air entering the stratosphere in the tropics. *J. Geophys. Res.*, **110**.
- Fueglistaler, S., A. Dessler, T. Dunkerton, I. Folkins, Q. Fu, and P. Mote, 2009: Tropical tropopause layer. *Rev. Geophys.*, **47**.
- Gheusi, F. and J. Stein, 2002: Lagrangian description of airflows using Eulerian passive tracers. *Quarterly Journal of the Royal Meteorological Society*, **128**, 337–360.
- Giannini, A., R. Saravanan, and P. Chang, 2003: Oceanic forcing of Sahel rainfall on interannual to interdecadal time scales. *Science*, **302**, 1027.
- Gu, G. and R. Adler, 2004: Seasonal evolution and variability associated with the West African monsoon system. *Journal of Climate*, **17**, 3364–3377.
- Guichard, N., N. Asencio, C. Peugeot, O. Bock, J. Redelsperger, X. Cui, M. Garvert, B. Lamptey, E. Orlandi, J. Sander, F. Fierli, M. Gaertner, S. Jones, J. Lafore, A. Morse, M. Nuret, A. Boone, G. Balsamo, P. de Rosnay, B. Decharme, N. R. P. Harris, and J. Berges, 2010: An intercomparison of simulated rainfall and evapotranspiration associated with a mesoscale convective system over west africa. *Weather and Forecasting*, **in press**.
- Homan, C. D., C. M. Volk, A. C. Kuhn, A. Werner, J. Baehr, S. Viciani, A. Ulanovski, and F. Ravegnani, 2009: Tracer measurements in the tropical tropopause layer during the amma/scout-o3 aircraft campaign. *Atmospheric Chemistry and Physics Discussions*, **9**, 25049–25084.



- Hopkins, J. R., M. J. Evans, J. D. Lee, A. C. Lewis, J. H. Marsham, J. B. McQuaid, D. J. Parker, D. J. Stewart, C. E. Reeves, and R. M. Purvis, 2009: Direct estimates of emissions from the megacity of Lagos. *Atmospheric Chemistry and Physics*, **9**, 8471–8477.
- Huffman, G., R. Adler, D. Bolvin, G. Gu, E. Nelkin, K. Bowman, Y. Hong, E. Stocker, and D. Wolff, 2007: The TRMM Multisatellite Precipitation Analysis (TMPA): Quasi-global, multiyear, combined-sensor precipitation estimates at fine scales. *Journal of Hydrometeorology*, **8**, 38–55.
- Huffman, G., R. Adler, M. Morrissey, D. Bolvin, S. Curtis, R. Joyce, B. McGavock, and J. Susskind, 2001: Global precipitation at one-degree daily resolution from multisatellite observations. *Journal of Hydrometeorology*, **2**, 36–50.
- Janicot, S., C. Thorncroft, A. Ali, N. Asencio, G. Berry, O. Bock, B. Bourles, G. Caniaux, F. Chauvin, A. Deme, et al., 2008: Large-scale overview of the summer monsoon over West Africa during the AMMA field experiment in 2006, *Annales Geophysicae*, vol. 26.
- Jenkins, G. S., M. Camara, and S. A. Ndiaye, 2008: Observational evidence of enhanced middle/upper tropospheric ozone via convective processes over the equatorial tropical Atlantic during the summer of 2006. *Geophys. Res. Lett.*, **35**.
- Jonquieres, I., A. Marengo, A. Maalej, and F. Rohrer, 1998: Study of ozone formation and transatlantic transport from biomass burning emissions over West Africa during the airborne tropospheric ozone campaigns Tropoz I and Tropoz II. *Journal of Geophysical Research-Atmospheres*, **103**.
- Khaykin, S., J. Pommereau, L. Korshunov, V. Yushkov, J. Nielsen, N. Larsen, T. Christensen, A. Garnier, A. Lukyanov, and E. Williams, 2009: Hydration of the lower stratosphere by ice crystal geysers over land convective systems. *Atmos. Chem. Phys.*, **9**, 2275–2287.

- Lafore, J., J. Stein, N. Asencio, P. Bougeault, V. Ducrocq, J. Duron, C. Fischer, P. Hérel, P. Mascart, V. Masson, et al., 1997: The Meso-NH atmospheric simulation system. Part I: Adiabatic formulation and control simulations, *Annales Geophysicae*, vol. 16, Springer.
- Laing, A., R. Carbone, V. Levizzani, and J. Tuttle, 2008: The propagation and diurnal cycles of deep convection in northern tropical Africa. *Quarterly Journal of the Royal Meteorological Society*, **134**, 93–110.
- Laing, A. and J. Fritsch, 2000: The large-scale environments of the global populations of mesoscale convective complexes. *Monthly Weather Review*, **128**, 2756–2776.
- Lebel, T. and A. Ali, 2009: Recent trends in the Central and Western Sahel rainfall regime (1990–2007). *Journal of Hydrology*, **375**, 52–64.
- Lebel, T., B. Cappelaere, S. Galle, N. Hanan, L. Kergoat, S. Levis, B. Vieux, L. Descroix, M. Gosset, E. Mougin, et al., 2009a: AMMA-CATCH studies in the Sahelian region of West-Africa: an overview. *Journal of Hydrology*, **375**, 3–13.
- Lebel, T., D. Parker, C. Flamant, B. Bourles, B. Marticorena, E. Mougin, C. Peugeot, A. Diedhiou, J. Haywood, J. Ngamini, et al., 2009b: The amma field campaigns: Multiscale and multidisciplinary observations in the west african region. *QJR Meteorol. Soc.*, **135**.
- Ma, L., J. Chan, N. Davidson, and J. Turk, 2007: Initialization with diabatic heating from satellite-derived rainfall. *Atmospheric Research*, **85**, 148–158.
- Malguzzi, P., G. Grossi, A. Buzzi, R. Ranzi, and R. Buizza, 2006: Climate and Dynamics-D24106-The 1966” century” flood in Italy: A meteorological and hydrological revisitation (DOI 10.1029/2006JD007111). *Journal of Geophysical Research-Part D-Atmospheres*, **111**.

- Marenco, A., V. Thouret, P. Nédélec, H. Smit, M. Helten, D. Kley, F. Karcher, P. Simon, K. Law, J. Pyle, et al., 1998: Measurement of ozone and water vapor by Airbus in-service aircraft: The MOZAIC airborne program, An overview. *Journal of Geophysical Research-Atmospheres*, **103**.
- Mari, C. H., G. Cailley, L. Corre, M. Saunois, J. L. Attié, V. Thouret, and A. Stohl, 2008: Tracing biomass burning plumes from the southern hemisphere during the amma 2006 wet season experiment. *Atmospheric Chemistry and Physics*, **8**, 3951–3961.
- Marti, J. and K. Mauersberger, 1993: A survey and new measurements of ice vapour pressure at temperatures between 170 K and 250 K. *Geophys. Res. Lett*, **20**, 363–366.
- Mauzerall, D., J. Logan, D. Jacob, B. Anderson, D. Blake, J. Bradshaw, B. Heikes, G. Sachse, H. Singh, and B. Talbot, 1998: Photochemistry in biomass burning plumes and implications for tropospheric ozone over the tropical South Atlantic. *Journal of Geophysical Research*, **103**, 8401–8424.
- Mekonnen, A., C. Thorncroft, and A. Aiyyer, 2006: Analysis of convection and its association with African easterly waves. *Journal of Climate*, **19**, 5405–5421.
- Mullendore, G. L., D. R. Durran, and J. R. Holton, 2005: Cross-tropopause tracer transport in midlatitude convection. *J. Geophys. Res.*, **110**.
- Nicholson, S., B. Some, J. McCollum, E. Nelkin, D. Klotter, Y. Berte, B. Diallo, I. Gaye, G. Kpabeba, O. Ndiaye, et al., 2003: Validation of TRMM and other rainfall estimates with a high-density gauge dataset for West Africa. Part I: validation of GPCC rainfall product and pre-TRMM satellite and blended products. *Journal of Applied Meteorology*, **42**, 1337–1354.
- Orlandi, E., F. Fierli, S. Davolio, A. Buzzi, and O. Drofa, 2010: A nudging scheme to assimilate satellite brightness temperature in a meteorological model: Impact

- on African mesoscale convective systems representation. *QJR Meteorol. Soc.*, **in press**.
- Park, S., R. Jiménez, B. Daube, L. Pfister, T. Conway, E. Gottlieb, V. Chow, D. Curran, D. Matross, A. Bright, et al., 2007: The CO<sub>2</sub> tracer clock for the Tropical Tropopause Layer. *Atmos. Chem. Phys.*, **7**, 3989–4000.
- Pfister, L., H. B. Selkirk, E. J. Jensen, M. R. Schoeberl, O. B. Toon, E. V. Browell, W. B. Grant, B. Gary, M. J. Mahoney, T. V. Bui, and E. Hintsas, 2001: Aircraft observations of thin cirrus clouds near the tropical tropopause. *J. Geophys. Res.*, **106**, 9765–9786.
- Pope, V., M. Gallani, P. Rowntree, and R. Stratton, 2000: The impact of new physical parametrizations in the Hadley Centre climate model: HadAM3. *Climate Dynamics*, **16**, 123–146.
- Real, E., E. Orlandi, K. S. Law, F. Fierli, D. Josset, F. Cairo, H. Schlager, S. Borrmann, D. Kunkel, M. Volk, J. B. McQuaid, D. J. Stewart, J. Lee, A. Lewis, J. R. Hopkins, F. Ravegnani, A. Ulanovski, and C. Lioussé, 2009: Cross-hemispheric transport of central african biomass burning pollutants: implications for downwind ozone production. *Atmospheric Chemistry and Physics Discussions*, **9**, 17385–17427.
- Redelsperger, J., A. Diongue, A. Diedhiou, J. Ceron, M. Diop, J. Gueremy, and J. Lafore, 2002: Multi-scale description of a Sahelian synoptic weather system representative of the West African monsoon. *Quarterly Journal of the Royal Meteorological Society*, **128**, 1229–1258.
- Redelsperger, J., C. Thorncroft, A. Diedhiou, T. Lebel, D. Parker, and J. Polcher, 2006: African Monsoon Multidisciplinary Analysis: An international research project and field campaign. *Bulletin of the American Meteorological Society*, **87**, 1739–1746.

- Roca, R., J. Lafore, C. Piriou, and J. Redelsperger, 2005: Extratropical dry-air intrusions into the West African monsoon midtroposphere: An important factor for the convective activity over the Sahel. *Journal of the Atmospheric Sciences*, **62**, 390–407.
- Rotunno, R., J. Klemp, and M. Weisman, 1988: A theory for strong, long-lived squall lines. *Journal of the Atmospheric Sciences*, **45**, 463–485.
- Rudolf, B. and U. Schneider, 2004: Calculation of gridded precipitation data for the global land-surface using in-situ gauge observations. *Proceedings of the 2nd Workshop of the International Precipitation Working Group IPWG, Monterey*, 231–247.
- Sassen, K., Z. Wang, and D. Liu, 2009: Cirrus clouds and deep convection in the tropics: Insights from calipso and cloudsat. *J. Geophys. Res.*, **114**, D00H06.
- Sauvage, B., F. Gheusi, V. Thouret, J. Cammas, J. Duron, J. Escobar, C. Mari, P. Mascart, and V. Pont, 2007: Medium-range mid-tropospheric transport of ozone and precursors over Africa: two numerical case studies in dry and wet seasons. *Atmos. Chem. Phys.*, **7**, 5357–5370.
- Sauvage, B., V. Thouret, J. Cammas, F. Gheusi, G. Athier, and P. Nédélec, 2005: Tropospheric ozone over Equatorial Africa: regional aspects from the MOZAIC data. *Atmos. Chem. Phys.*, **5**, 311–335.
- Schmetz, J., S. Tjemkes, M. Gube, and L. Van de Berg, 1997: Monitoring deep convection and convective overshooting with METEOSAT. *Advances in Space Research*, **19**, 433–441.
- Skamarock, W., J. Klemp, J. Dudhia, D. Gill, D. Barker, W. Wang, and J. Powers, 2005: A description of the Advanced Research WRF Version 2. *NCAR technical note*, **468**, 88.

- Stohl, A., G. Wotawa, P. Seibert, and H. Kromp-Kolb, 1995: Interpolation errors in wind fields as a function of spatial and temporal resolution and their impact on different types of kinematic trajectories. *Journal of Applied Meteorology*, **34**, 2149–2165.
- Sultan, B. and S. Janicot, 2003: The West African monsoon dynamics. Part II: The “Preonset” and “Onset” of the summer monsoon. *Journal of Climate*, **16**, 3407–3427.
- Swap, R., H. Annegarn, J. Suttles, J. Haywood, M. Helmlinger, C. Hely, P. Hobbs, B. Holben, J. Ji, M. King, et al., 2002: The Southern African Regional Science Initiative (SAFARI 2000): overview of the dry season field campaign. *South African Journal of Science*, **98**, 125.
- Thompson, A., K. Pickering, D. McNamara, M. Schoeberl, R. Hudson, J. Kim, E. Browell, V. Kirchhoff, and D. Nganga, 1996: Where did tropospheric ozone over southern Africa and the tropical Atlantic come from in October 1992? Insights from TOMS, GTE TRACE A, and SAFARI 1992. *Journal of Geophysical Research-Atmospheres*, **101**.
- Thouret, V., M. Saunois, A. Minga, A. Mariscal, B. Sauvage, A. Solete, D. Agbangla, P. Nédélec, C. Mari, C. E. Reeves, and H. Schlager, 2009: An overview of two years of ozone radio soundings over cotonou as part of amma. *Atmospheric Chemistry and Physics*, **9**, 6157–6174.
- Williams, J. E., M. P. Scheele, P. F. J. van Velthoven, J.-P. Cammas, V. Thouret, C. Galy-Lacaux, and A. Volz-Thomas, 2009: The influence of biogenic emissions from africa on tropical tropospheric ozone during 2006: a global modeling study. *Atmospheric Chemistry and Physics*, **9**, 5729–5749.



# Registrazione modulo Dichiarazione di conformità

## MODULO INVIATO CORRETTAMENTE

**Consegnare la copia stampata e debitamente firmata all'Ufficio Dottorato e Alta Formazione in via Scienze 41b Ferrara**

Io sottoscritto Dott. (Cognome e Nome)

Orlandi Emiliano

nato a

Milano

Provincia

Milano

il giorno

17/04/1979

Your E-Mail Address

e.orlandi@isac.cnr.it

avendo frequentato il corso di Dottorato di Ricerca in:

Fisica

Ciclo di Dottorato

XXII

Titolo della tesi in Italiano

Studio della convezione durante il monsone africano: osservazioni e modellazione della precipitazione e del ruolo della circolazione regionale sulla composizione atmosferica.

Titolo della tesi in Inglese

CONVECTION DURING THE AFRICAN MONSOON: OBSERVATIONS AND MODELLING OF PRECIPITATION AND THE ROLE OF REGIONAL CIRCULATION ON ATMOSPHERIC COMPOSITION.

Titolo della tesi in altra Lingua Straniera

Tutore - Prof:

Prodi Franco

Settore Scientifico Disciplinare (SSD)

FIS/06

Parole chiave (max 10)

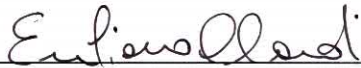
Convezione, precipitazione, monsone africano, modelli meteorologici, trasporto di gas in traccia, fuochi di biomassa. Convection, precipitation, African monsoon, meteorological models, trace gases transport, biomass burning

Consapevole - Dichiaro

CONSAPEVOLE --- 1) del fatto che in caso di dichiarazioni mendaci, oltre alle

sanzioni previste dal codice penale e dalle Leggi speciali per l'ipotesi di falsità in atti ed uso di atti falsi, decade fin dall'inizio e senza necessità di alcuna formalità dai benefici conseguenti al provvedimento emanato sulla base di tali dichiarazioni; -- 2) dell'obbligo per l'Università di provvedere al deposito di legge delle tesi di dottorato al fine di assicurarne la conservazione e la consultabilità da parte di terzi; -- 3) della procedura adottata dall'Università di Ferrara ove si richiede che la tesi sia consegnata dal dottorando in 4 copie di cui una in formato cartaceo e tre in formato .pdf, non modificabile su idonei supporti (CD-ROM, DVD) secondo le istruzioni pubblicate sul sito : <http://www.unife.it/dottorati/dottorati.htm> alla voce ESAME FINALE – disposizioni e modulistica; -- 4) del fatto che l'Università sulla base dei dati forniti, archiverà e renderà consultabile in rete il testo completo della tesi di dottorato di cui alla presente dichiarazione attraverso l'Archivio istituzionale ad accesso aperto "EPRINTS.unife.it" oltre che attraverso i Cataloghi delle Biblioteche Nazionali Centrali di Roma e Firenze. --- DICHIARO SOTTO LA MIA RESPONSABILITA' --- 1) che la copia della tesi depositata presso l'Università di Ferrara in formato cartaceo, è del tutto identica a quelle presentate in formato elettronico (CD-ROM, DVD), a quelle da inviare ai Commissari di esame finale e alla copia che produrrò in seduta d'esame finale. Di conseguenza va esclusa qualsiasi responsabilità dell'Ateneo stesso per quanto riguarda eventuali errori, imprecisioni o omissioni nei contenuti della tesi; -- 2) di prendere atto che la tesi in formato cartaceo è l'unica alla quale farà riferimento l'Università per rilasciare, a mia richiesta, la dichiarazione di conformità di eventuali copie; -- 3) che il contenuto e l'organizzazione della tesi è opera originale da me realizzata e non compromette in alcun modo i diritti di terzi, ivi compresi quelli relativi alla sicurezza dei dati personali; che pertanto l'Università è in ogni caso esente da responsabilità di qualsivoglia natura civile, amministrativa o penale e sarà da me tenuta indenne da qualsiasi richiesta o rivendicazione da parte di terzi; -- 4) che la tesi di dottorato non è il risultato di attività rientranti nella normativa sulla proprietà industriale, non è stata prodotta nell'ambito di progetti finanziati da soggetti pubblici o privati con vincoli alla divulgazione dei risultati, non è oggetto di eventuali registrazioni di tipo brevettale o di tutela. --- PER ACCETTAZIONE DI QUANTO SOPRA RIPORTATO

Firma Dottorando  
Ferrara, li 24/02/2010

Firma del Dottorando 

Firma Tutore  
Visto: Il Tutore Prodi Franco  
Si approva

Firma del Tutore 

---

FORMAZIONE POSTLAUREA

Ufficio Dottorato di Ricerca - Ufficio Alta Formazione ed Esami di Stato - IUSS

---